NEAR EAST UNIVERSITY

INSTITUTE OF GRADUATE STUDIES

DEPARTMENT OF PHYSICS ENGINEERING

UPGRADE OF CMS ENDCAP CALORIMETERS

AND

SILICON SENSOR CHARACTERIZATION

M.Sc. THESIS

Gizem Gül DİNÇER

Nicosia

May, 2024

NEAR EAST UNIVERSITY

INSTITUTE OF GRADUATE STUDIES

DEPARTMENT OF PHYSICS ENGINEERING

UPGRADE OF CMS ENDCAP CALORIMETERS

AND

SILICON SENSOR CHARACTERIZATION

M.Sc. THESIS

Gizem Gül DİNÇER

Supervisor

Prof. Dr. Kerem CANKOÇAK

Nicosia

May, 2024

Approval

We certify that we have read the thesis submitted by Gizem Gül DİNÇER titled **"Upgrade of CMS Endcap Calorimeters and Silicon Sensor Characterization"** and that in our combined opinion it is fully adequate, in scope and in quality, as a thesis for the degree of Master of Applied Sciences.

Examining Committee	Name-Surname	Signature
Head of the Committee:	Assoc. Prof. Dr. Zalihe TÜRKER	
Committee Member:	Prof. Dr. Dilber Uzun ÖZŞAHİN	
Supervisor:	Prof. Dr. Kerem CANKOÇAK	
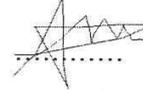
Approved by the Head of the Department

28/05/2024

Assoc. Prof. Dr. Zalihe TÜRKER
Head of the Department

Approved by the Institute of Graduate Studies

28/05/2024

Prof. Dr. Kemal Hüsnü Can Başer
Head of the Institute of Graduate Studies

Declaration

I hereby declare that all information, documents, analysis and results in this thesis have been collected and presented according to the academic rules and ethical guidelines of Institute of Graduate Studies, Near East University. I also declare that as required by these rules and conduct, I have fully cited and referenced information and data that are not original to this study.

Gizem Gül DİNÇER

28/05/2024

Acknowledgments

First of all, I would like to express my sincere thanks to my supervisor Prof. Dr. Kerem Cankoçak for his valuable feedback and suggestions on my thesis. His insights and guidance were instrumental in shaping my research and writing this thesis. Also, I would like to thank Eva Sicking, head of the Silicon Sensor group in the HGCAL project at CERN, for her support and guidance throughout my MSc program. Her expertise and patience were invaluable to me and played a crucial role in the success of this thesis. Additionally, I would like to thank Dave Barney, Group Leader for CMS Detector Activities (current and future) and Technical Coordinator for HGCAL at CERN, for allowing me to take part in this project and for guiding me throughout my MSc program. I am grateful to all of them. Without their support at all stages of the thesis project, the completion of this work would not have been possible. I would also like to thank Head of Physics Engineering Dept. Assoc. Prof. Dr. Zalihe Türker and Prof. Dr. Dilber Uzun Özşahin, for always helping and supporting me. Finally, I would like to sincerely thank Prof. Dr. Tamer Şanlıdağ, the Rector of the Near East University, for his support during my post graduate studies. Without his support for the CERN project, I would not have started this research.

Gizem Gül DİNÇER

Abstract

UPGRADE OF CMS ENDCAP CALORIMETERS AND SILICON
SENSOR CHARACTERIZATION
DİNÇER, Gizem Gül
M.Sc. Department of Physics Engineering
May, 2024, 109 pages

Since 2008, the CMS detector at the LHC has suffered radiation damage in many sub-detectors due to particle radiation from proton-proton collisions. Due to this radiation damage and the 10-fold increase in luminosity at the HL-LHC, extensive upgrades and refurbishments are planned for the CMS experiment in the coming years. This thesis covers the radiation damage in the CMS calorimetry system and the upgrade to high-granularity calorimetry (HGCAL), which will replace the existing electromagnetic and hadronic calorimeters with end caps. In addition to the electrical characterization of the silicon sensors to be used in HGCAL, the quality control steps and analysis of the hexaboards where the sensors will be placed are also included in this thesis. Hexaboards are the main active part of the silicon hexagonal module consisting of silicon sensor, kapton foil and base plate. Technical specifications of hexaboards are given in the thesis. In addition to the detailed discussion of the techniques and setups used for the electrical characterization of silicon sensors, HGCAL's test strategy for silicon sensors is also included.

HGCAL has a "wedge" containing several hexagonal modules. Here, partial sensors are needed to provide sufficient coverage around the regions instrumented with silicon sensors. This thesis includes the analysis of both full and partial sensors with low-density. This refurbishment and upgrade project at CMS will improve the detector systems to provide the required physics performance under the challenging conditions of high luminosity at HGCAL, HL-LHC. The installation of the upgraded detector systems is planned to be completed at LS3, scheduled between 2026 and 2028.

Keywords: calorimetry, particle physics, proton accelerator, radiation damage

Özet

CMS ENDCAP KALORİMETRELERİNİN YÜKSELTMESİ VE SİLİKON SENSÖR KARAKTERİZASYONU

DİNÇER, Gizem Gül
M.Sc. Fizik Mühendisliği Bölümü
Mayıs, 2024, 109 sayfa

LHC hızlandırıcısındaki CMS detektöründe 2008'den beri süregelen proton-proton çarpışmalarından çıkan parçacık radyasyonu nedeniyle pek çok alt detektörde radyasyon hasarı gözlenmektedir. Gerek bu radyasyon hasarı yüzünden gerekse HL-LHC de luminozitenin 10 kat artması yüzünden önümüzdeki yıllarda CMS deneyinde çok kapsamlı yükseltme ve yenileme çalışmaları planlanmaktadır. Bu tez, CMS kalorimetre sistemindeki radyasyon hasarını ve mevcut uç kapaklı elektromanyetik ve hadronik kalorimetrelerin yerini alacak olan yüksek tanecikli kalorimetresini (HGCAL) kapsamaktadır. HGCAL'da kullanılacak olan silikon sensörlerin elektriksel karakterizasyonunun yanı sıra sensörlerin yerleştirileceği hexaboard'ların kalite kontrol adımlarına ve analizine de bu tezde yer verilmiştir. Hexaboard'lar, silikon sensör, kapton folyo ve taban plakasından oluşan silikon altıgen modülün ana aktif parçasıdır. Hexaboardların teknik özelliklerine tezde yer verilmiştir. Silikon sensörlerin elektriksel karakterizasyonu için kullanılan teknik ve kurulum çalışmalarının detaylı bir şekilde de ele alınmasının yanı sıra HGCAL'ın silikon sensörler için test stratejisine de yer verilmiştir.

HGCAL'da birçok altıgen modül içeren bir "kama" mevcuttur. Burada silikon sensörlerle enstrümante edilen bölgelerin çevrelerinde yeterli kapsama alanı sağlamak için kısmi sensörlere ihtiyaç vardır. Bu tez çalışması düşük yoğunluklu hem tam hem de kısmi sensörlerin analizini içermektedir. CMS'deki bu yenileme ve yükseltme projesi, HGCAL, HL-LHC deki yüksek parlaklığın zorlu koşulları altında gerekli fizik performansını sağlamak için detektör sistemlerini geliştirecektir. Yükseltilmiş detektör sistemlerinin kurulumunun 2026 ila 2028 yılları arasında planlanan LS3'te tamamlanması planlanmaktadır.

Anahtar Kelimeler: kalorimetre, parçacık fiziği, proton hızlandırıcısı, radyasyon hasarı

Table of Contents

CHAPTER I

CHAPTER II

CHAPTER III

CHAPTER IV

CHAPTER V

List of Tables

List of Figures

List of Abbreviations

ALICE	A Large Ion Collider Experiment
ARRAY	Switching matrix probe card system
ATLAS	A Toroidal LHC ApparatuS
CMS	Compact Muon Solenoid
CERN	Conseil Europeen pour la Recherche Nucleaire
CE	CMS Endcap Calorimeter
CV	Capacitance-Voltage
DAQ	Data Acquisition System
ECAL	Electromagnetic Calorimeter
EE	Electromagnetic Endcap
ES	Endcap Preshower
Epi	Epitaxial process
FZ	Float zone
HB	Hadron Barrel Calorimeter
HE	Hadron Endcap Calorimeter
HF	Hadron Forward Calorimeter
HO	Hadron Outer Calorimeter
HCAL	Hadronic Calorimeter
HD	High-Density
HGCAL	High Granularity Calorimeter
HGCROC	High-Granularity Calorimeter Readout
HL-LHC	High Luminosity Large Hadron Collider
HPK	Hamamatsu Photonics K.K.
IV	Leakage Current
LD	Low-Density
LHC	Large Hadron Collider
LHCb	Large Hadron Collider beauty
MGW	Multiple Geometry Wafers
MUXOUT	Output Multiplexer
MUX512	512-Channel Multiplexer
PCB	Printed Circuit Board
PMT	Photomultiplier Tube

PQC   Process Quality Control

QIE   Charge Integrator and Encoder

RadDam   Online Radiation Damage Monitoring

SiPM   Silicon Photomultiplier

SMU   Source Measure Unit

SQC   Sensor Quality Control

TDC   Time-to-Digital Converter

TS   Time Slot

VQC   Vendor Quality Control

CHAPTER I

Introduction

Throughout history, mankind has endeavored to understand nature around the questions "what is matter made of?" and "what holds them together?". Numerous experiments and theoretical studies that have provided suggestions, predictions and interpretations have shown that matter is composed of very few and very small building blocks (Workman et al., 2022). In other words, air, water, fire and earth are composed of atoms ten billionths of a meter in size; atoms are composed of nuclei ten thousand times smaller than themselves and electrons one billion times smaller; and the nucleus is composed of neutrons and protons ten times smaller than themselves. The protons and neutrons in the atomic nucleus are composed of quarks, which are fundamental particles. The behavior of such small entities is different from that of the objects we observe in daily life: the more precisely their position can be measured, the less precisely their velocity can be known (Heisenberg uncertainty principle); they exhibit both wave and particle properties; they do not follow a certain trajectory during motion; they experience unobservable intermediate states when moving from one given state to another. This set of principles is called quantum mechanics. Today, we know very well the basic structure of the universe we live in and the matter that constitutes it (Peskin & Daniel, 2019). The best theory ever developed and experimentally proven is the so-called Standard Model (SM). The Standard Model, which combines two of the four known fundamental forces in the universe, the Electromagnetic and Weak forces, in the same theory, has been one of the greatest achievements of physical science in the 20th century. The theory, proposed by Glashow, Salam and Weinberg in the 1960s, was developed and tested over the next 30 years, and with successive discoveries, it has become the only accurate model describing elementary particles that can be tested experimentally (Bilenky & Hošek, 1982).

Statement of the Problem: Problems of Standard Model

Although the Standard Model, supported by many experiments, provides a very good explanation of what is happening in the universe we live in, there are still some unanswered questions. A particle necessary for the Standard Model (which we call the Higgs particle) was discovered at CERN (Higgs, 1964). According to the Standard Model, the fundamental particles that are the building blocks of matter are the six leptons, six quarks and the intermediary particles that carry out the fundamental interactions between them. According to this model, the Higgs particle, which is necessary to explain where the masses of particles come from, was detected in 2012 in two of the four major experiments, CMS and ATLAS, and its mass was measured to be 125 GeV (Jenni & Virdee, 2020). However, the Higgs particle alone is not enough (Altarelli, 2013). The quantum corrections to the Higgs particle far exceed the mass of the Higgs particle, which is a big problem. The SM is currently too fine-tuned. We need a simpler, more holistic theory. One of the main aims of the LHC experiments is to test the models which are Beyond Standard Model (such as Supersymmetry or any other BSM models). The source of Dark Matter, the diffraction of matter/antimatter symmetry, etc. require physics models beyond the SM (Denegri et al., 2021).

Purpose of the Study: CERN and CMS Detector Upgrade

CERN, which stands for the European Council for Nuclear Research, was established in Geneva, Switzerland, and is the world's largest particle physics laboratory. Founded in 1954 by 12 European countries, CERN currently has 23 members. Its budget is over several billion Swiss francs. CERN, which is a striking example of the importance given by developed countries to basic sciences, is the first post-war council in which all European countries participated together (Krige, 1996).

The purpose of CERN's establishment is to carry out joint research that member countries cannot carry out with their own budgetary means. Today, approximately 10,000 researchers (half of the world's particle physicists) representing 500 institutes from 80 countries are conducting research at CERN (CERN Official Website, 2023). CERN is a

center where very important scientific discoveries, which have also been awarded Nobel Prizes, have been made. With the Large Hadron Collider (LHC), which was launched in 2008, CERN is known as the "Experiment of the Century" in the world public opinion.

CERN provides scientists at the cutting edge of fundamental science with the most advanced experimental facilities that technology permits, and pushes technology to increase these facilities. Advanced technologies developed at CERN are transferred free of charge to the countries participating in the experiments. The World Wide Web (www) system, which is used by mankind today to access information and communicate, was discovered and developed at CERN. Here is a brief history of CERN and its major achievements:

- 1954: Foundation of the European Organization for Nuclear Research (CERN).
- 1957: First accelerator, the Synchrocyclotron, of CERN starts up.
- 1959: Proton Synchrotron (PS), starts up. The PS is still the heart of CERN's accelerator complex even today.
- 1968: Georges Charpak invented the multi-wire proportional chamber and received the Nobel Prize for this invention in 1992.
- 1971: The Intersecting Storage Rings (ISR) are up and running. The world's first hadron collider, ISR marked the transition from research with beams striking fixed targets to experiments studying colliding beams.
- 1973: The Gargamelle experiment and the discovery of neutral currents provided evidence for the electroweak theory.
- 1976: The Super Proton Synchrotron (SPS) with a circumference of 7 kilometers was put into service. The SPS, which provided light for a wide range of experiments, was later used as the world's first proton-antiproton collider.
- 1983: The CERN experiments UA1 and UA2 detected the existence of W and Z particles, the carriers of the weak interaction, and measured their masses.
- 1989: The Large Electron Positron Collider (LEP), built about 100 meters below the Earth's surface and 27 kilometers in circumference, has begun operation. In the same year, Tim Berners-Lee presented his plan for the World Wide Web under a proposal title such as 'Knowledge Management'. The first web server was up and running by the end of 1990,

and three years later CERN made the software available royalty-free. Thus, was born the WWW, which today we call the Internet.

- 1995: The first antihydrogen atoms were created in the PS210 experiment using a beam from the Low Hydrogen Power Plant.
- 2008: The LHC circulates its first beam on September 10.
- 2012: On July 4 at CERN, the ATLAS and CMS collaborations presented evidence in LHC data for a particle consistent with the Higgs boson, the particle linked to the mechanism proposed in the 1960s to give mass to W, Z and other particles.
- 2013: Further analysis confirms that the new particle is a Higgs boson, leading to the Nobel Prize in Physics for François Englert and Peter Higgs for proposing the mechanism that gives mass to elementary particles.
- 2024: The third operating period of the LHC at a center-of-mass energy of 13.6 TeV is underway.

Basically, the work carried out at CERN can be summarized as the study of the basic fundamental structure of matter and the investigation of the forces that hold matter together. But the technologies discovered in the process of investigating the building blocks of matter are used in everyday life in almost every field from medicine to the Internet.

So far, the LHC (Large Hadron Collider) at the European Particle Physics Laboratory at CERN, with its 27-kilometer superconducting ring, enables proton-proton collisions at a center-of-mass energy of 13.6 TeV. The LHC experiments aim to observe models beyond the Standard Model. By colliding proton beams at speeds close to the speed of light in the LHC accelerator, it is aimed to create the environment of the first moments of the Big Bang.

Since 30 March 2010, proton collisions have been going on at center-of-mass energies of 7 TeV, 8 TeV, 13 TeV and 13.6 TeV, respectively. There is no other accelerator on Earth capable of colliding protons at these energies. The main purpose of these experiments can be summarized as finding answers to questions that the Standard Model, which is the last point reached in Particle Physics, cannot answer. The Standard Model explains how the building blocks of matter behave and how they interact with each

other, but it does not give us information about their causes. The LHC experiments aim to find out the reasons for these behaviors. They have been designed for this purpose and have been collecting data since 2009. The LHC at CERN contains four large experiments (detectors) (CERN Official Website, 2023):

1.   A Large Ion Collider Experiment (ALICE)

2.   Large Hadron Collider beauty Experiment (LHC-b)

3.   A Toroidal LHC Apparatus (ATLAS)

4.   Compact Muon Solenoid (CMS)

At the LHC accelerator in a tunnel 100 meters underground, protons are accelerated by an electric field. Figure 1.1 shows the LHC ring (Evans & Bryant, 2008).

Figure 1.1: The CERN site near the city of Geneva. The circular ring underground is shown (yellow line) and the locations of the four experiments being conducted are indicated. The circumference of the LHC is 27 kilometers long.

1232 superconducting magnets are used to hold the proton beams, each of which will accelerate to 13.6 TeV, in orbit. At the LHC, proton beams travelling in opposite directions are first accelerated to an initial energy of 160 MeV in the linear accelerator LINAC4 and then to 2 GeV in the booster accelerator (Figure 1.2). They are then accelerated to an energy of 26 GeV in the Proton Synchrotron (PS) accelerator and then to 450 GeV in the Super Proton Synchrotron (SPS), which has a circumference of 7 km. From there, they reach the LHC tunnel and collide with each other when they reach energies of 13 or 13.6 TeV. The protons in the LHC ring orbit in beams travelling in opposite directions. Figure 1.2 shows the accelerator complex at CERN.
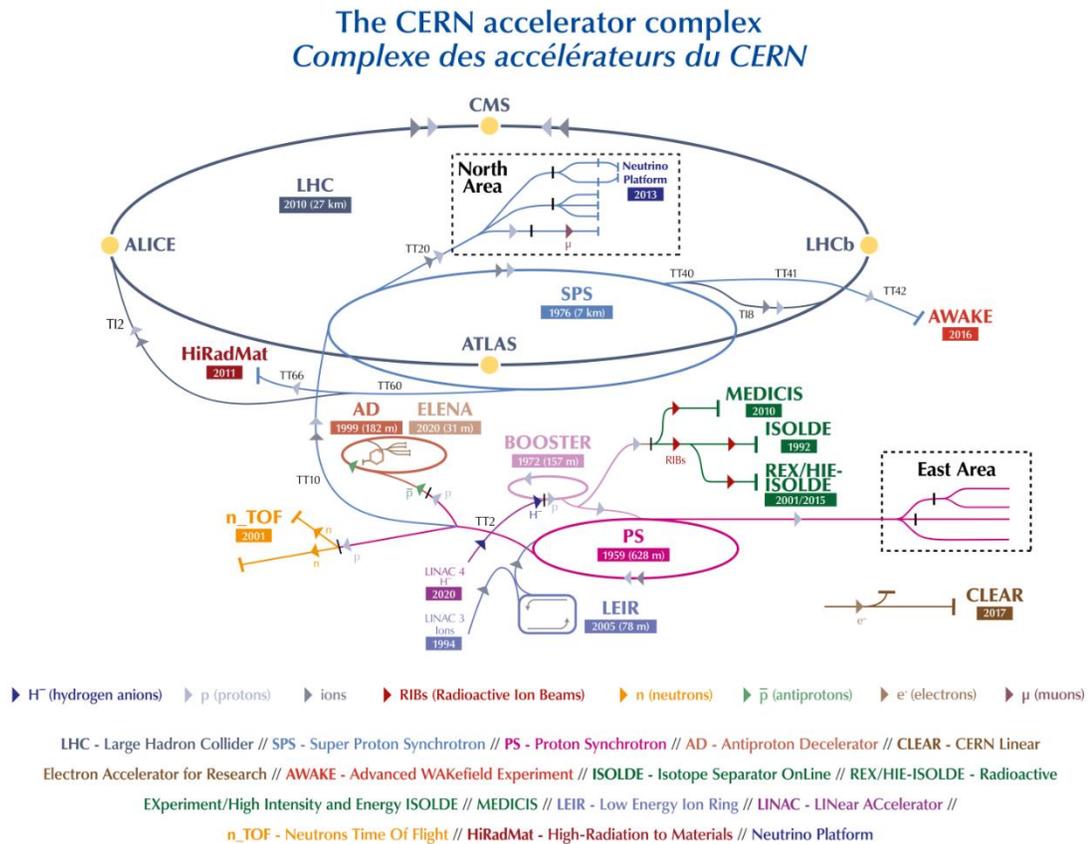
Figure 1.2: The accelerator complex at CERN.

As in modern particle detectors, the sub-detectors in the CMS detector are designed as vertex detectors, trace-detectors, electromagnetic and hadronic detectors, a

3.8 T solenoid magnet and muon detectors, starting respectively from the collision point of protons. The purpose of this design is to detect charged and uncharged particles, leptons and hadrons in separate sub-detectors, to measure the momentum of charged particles thanks to the 3.8 T magnetic field created by the solenoid, to determine the energies of the particles in calorimeters, and finally, thanks to the outermost muon detectors, to detect muons from the energies they release as they pass without being detected in other sub-detectors. A diagram of the Compact Muon Solenoid (CMS) detector is shown in Figure 1.3 (CMS Official Website, 2024).
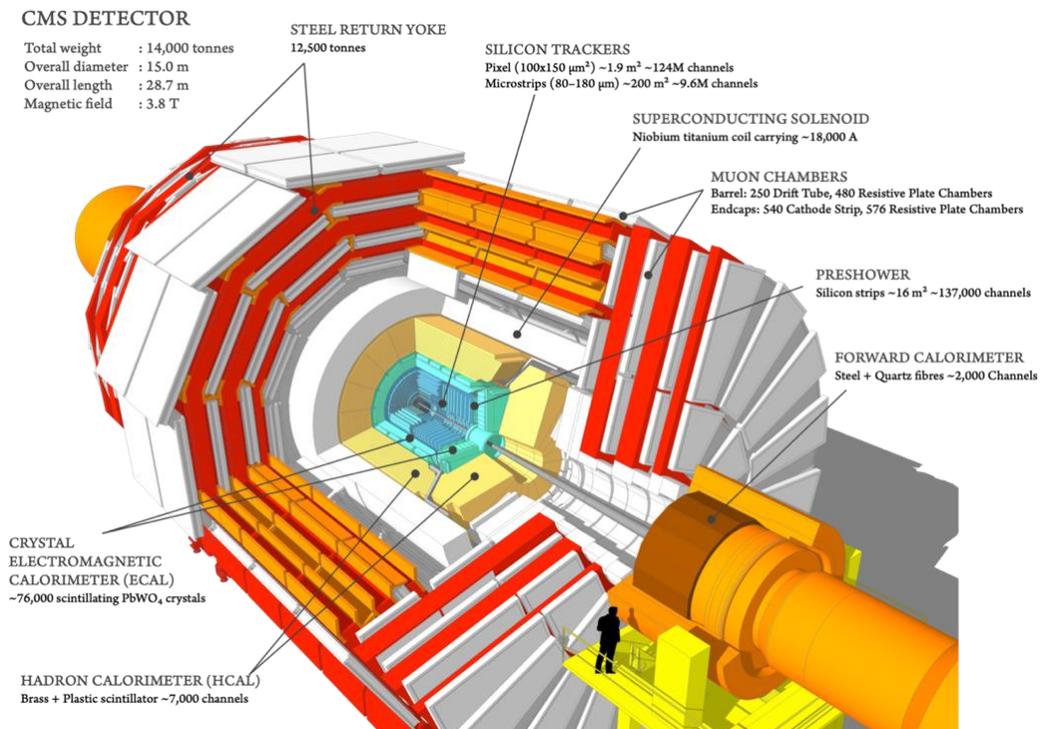
Figure 1.3: Structure of the CMS detector.

The tracker silicon pixel detectors of the CMS consist of a barrel and a forward cover disk. They are followed by silicon microstrip detectors with the same main body and cover disk configuration. The silicon tracer system is surrounded by a microstrip gas chamber (MSGC). The tracer systems are built into the calorimetry systems. The main

body of the Electromagnetic Calorimeter (ECAL) detector of CMS consists of 100,000 PbWO4 crystals, each 23 cm (25.6 Xo, 1.1 A) long and with a cross section of 2x2 cm. Outside the crystal calorimeter is a supporting hadron calorimeter (HCAL). The total length of the CMS detector is 30.0 m and the cap is 7.5 m. The solenoid has an inner diameter of 2.95 m and a length of 13 m.

Significance of the Study: HL-LHC and Calorimeter Upgrade

There are many unanswered questions in today's physics. One of the other goals of the LHC experiments is to seek answers to questions that the SM cannot answer and to test models of physics beyond the SM. Since the LHC opened in 2008, a special CMS upgrade program has been planned. This is because CERN has decided to upgrade the LHC accelerator and increase its luminosity to 10^{35} cm^{-2} s^{-1} (HL-LHC Website, 2024). Increasing the luminosity will undoubtedly greatly enhance the potential for new physics research, as it will make a statistically significant contribution (Dainese et al., 2019).

The CMS upgrade is being carried out in two phases. The first phase is related to the Phase-1 upgrade, while the second phase is related to the Phase-2 upgrade (Pásztor et al., 2021). The CMS Phase-1 upgrade took place during the second phase of the long shutdown (LS2) between 2019 and 2021. The upgrade of the hadron calorimeter (HCAL) at CMS, which consists of a middle section (Hadronic Barrel-HB), an end section (Hadronic Endcap-HE), an outer section (Hadronic Outer-HO) and a forward section (Hadronic Forward-HF), is mainly based on upgrading the photon detectors and improving the data acquisition electronics. In the hadron calorimeter, the avalanche effect and the hadronization of particles as they pass through the absorber cause photons to be emitted in plastic luminescent or fibers, which are collected by photo-detectors (Cooke, 2022). The CMS Phase-1 studies were completed by upgrading the photosensors (hybrid photodiodes-HPDs) in the barrel hadron calorimeter (HB) with silicon photomultipliers (SiPMs) and replacing the innermost pixel barrel layer.

Now, the plan is to further widen the cylindrical section of the beam to provide space for the Phase-2 pixel detector with extended pseudo-rapidity coverage to be installed during the long shutdown (LS3). This will maximize the high luminosity amplification of

the LHC (HL-LHC) (De Barbaro et al., 2017). However, one of the major problems of the CMS experiment at the HL-LHC is that with higher overall particle velocities, there will be higher particle "pile-up" in each LHC proton-proton collision event. This means higher instantaneous and integrated radiation doses hitting the detector elements. To solve this problem, CMS has silicon sensors that can withstand the expected irradiation levels, a new high-speed trigger, and detectors with higher detail or precise timing capabilities to help resolve pile-up events. Most of the CMS detector upgrades for the HL-LHC will be installed and commissioned during the long shutdown (LS3), scheduled for 2026-28. The High-Luminosity Upgrade plan for the LHC at CERN is shown in Figure 1.4 (CERN, 2022).

Figure 1.4: The existing and upcoming renovation/upgrade plan for the High Luminosity Upgrade at the LHC (CERN, 2022).

A major upgrade of the CMS detector aims to fully exploit the physics potential of the HL-LHC's challenging conditions, such as increased luminosity and higher clumping (Schmidt, 2016). The CMS detector will be replaced with pixel and strip tracking detectors to increase the resolution and provide extended (up to pseudo-rapidity $|\eta|=4$) geometric acceptance. The front-end electronics of the Electromagnetic Calorimeter (ECAL) barrel will be upgraded to access single crystal information at level 1 (L1) triggering, to provide 160 MHz sampling that provides high precision timing capability for photons, and to meet bandwidth requirements and trigger delay. The muon system will undergo upgrades for 3 types of gas detectors; new muon detectors with improved RPC

and gas electron multiplier technologies will increase kinematic velocity coverage (up to pseudo-rapidity |η|=2.8) and improve triggering and reconstruction performance in the forward region. The endcap electromagnetic and hadronic calorimeters (ECAL and HCAL) are planned to be replaced by an improved combined sampling calorimeter that will provide higher precision timing information and higher segmented spatial information in both the longitudinal direction and the transverse plane. A new timing detector for minimum ionizing particles in both the barrel and endcap regions will be added and aims to better reconstruct the interaction corners, all of which will be critical for these processes. This upgrade will also help reduce performance degradation due to high clutter (Ochando, 2017).

These renovations/upgrades, necessary to adapt to the High-Luminosity LHC (HL-LHC), which is scheduled to start in 2026, will be capable of sorting out the approximately 150 pile-up events that occur in each collision at the HL-LHC accelerator, which will produce five to ten times more collisions than the LHC (Lobanov, 2020). Since the number of proton-proton collisions produced at the HL-LHC will be ten times larger than originally planned for the CMS experiment, some of the existing detectors will not perform well enough during the HL-LHC phase. Therefore, the high-granularity calorimeter (HGCAL) will replace the existing endcap electromagnetic and hadronic calorimeters (CE-E and CE-H, respectively) during LS3 between 2024 and 2026. Silicon active layers will be used for the electromagnetic and front hadron calorimeter parts of the CMS High Granularity Calorimeter (HGCAL) and scintillators for the back hadron calorimeter (Paulitsch, 2020). The future Endcap Calorimeter called CE will be the large-scale application of a new technology in a particle physics experiment. The detector layers inside the absorber structure will have a high-granularity electromagnetic region consisting of a 26-layer silicon sensor with pad segmentation and a hadronic region with of 21 layers using the same technology in its innermost layers, but with a greater radius. As this new calorimeter is designed as high granularity system, it will allow measurement as 3D topology of energy depositions of the particle showers, caused by incoming hadrons, electrons and photons and accurate time stamping of neutral particles at the region close to the beam line.

The new detector provides 100 layers (50 at each end) of unprecedented information about electrons, photons and hadrons. With the Phase-2 HGCAL project, CMS will upgrade the detector systems in order to fulfill physics performance under the demanding conditions of high luminosity conditions of HL-LHC. The installation of the new detector systems is currently scheduled for completion at LS3, which is planned for 2026 to mid-2028. The main requirement for the HL-LHC is to distinguish head-on proton collisions from the hundreds of softer collisions. Because those softer collisions will accumulate in each event recording creating pile-ups. Therefore, the new calorimeters need high resolution to separate the trajectories of particles produced in these different collisions and then correlate them to their correct origin (Khan, 2023).

This upgrade will greatly improve the performance of discovery potential of the HL-LHC physics program, such as Vector Boson Fusion processes and searches for new physics with missing energy. Thus, of all the sub-detectors in the Hadron Calorimeter (HCAL), the Forward Hadron Calorimeter (HF) and the Endcap Calorimeter (HE) will become even more important. The HF and HE detectors will need to adapt to this new system of tracker detectors.

A photo of the electromagnetic calorimeter (ECAL) closest to the interaction point of the CMS detector and the surrounding hadronic calorimeter (HCAL) is shown in Figure 1.5 (Barney, 2021). The radiation exposure of the Forward Calorimeter (HF) detector is very high compared to the other sub-detectors (Penzo et al., 2009). The radiation dose is strongly dependent on the luminosity provided by the LHC and leads to a time-dependent deterioration of the calorimeter response. It is therefore very important to quantify the amount of radiation. However, measuring large amounts of radiation in real time is a very difficult task. Besides the lack of space in the detector to accommodate radiation measuring instruments, simultaneous measurement of such high radiation with conventional instruments has not been done so far. For this purpose, a new project called "online radiation monitoring-RADDAM" was launched in 2002. The main idea of the project is to determine the amount of radiation to which the HF detector is exposed by using fibers inside the HF. The peculiarity of this completely new method is that the

radiation exposure is determined from the radiation damage within the fibers themselves, without the aid of any instrumentation.
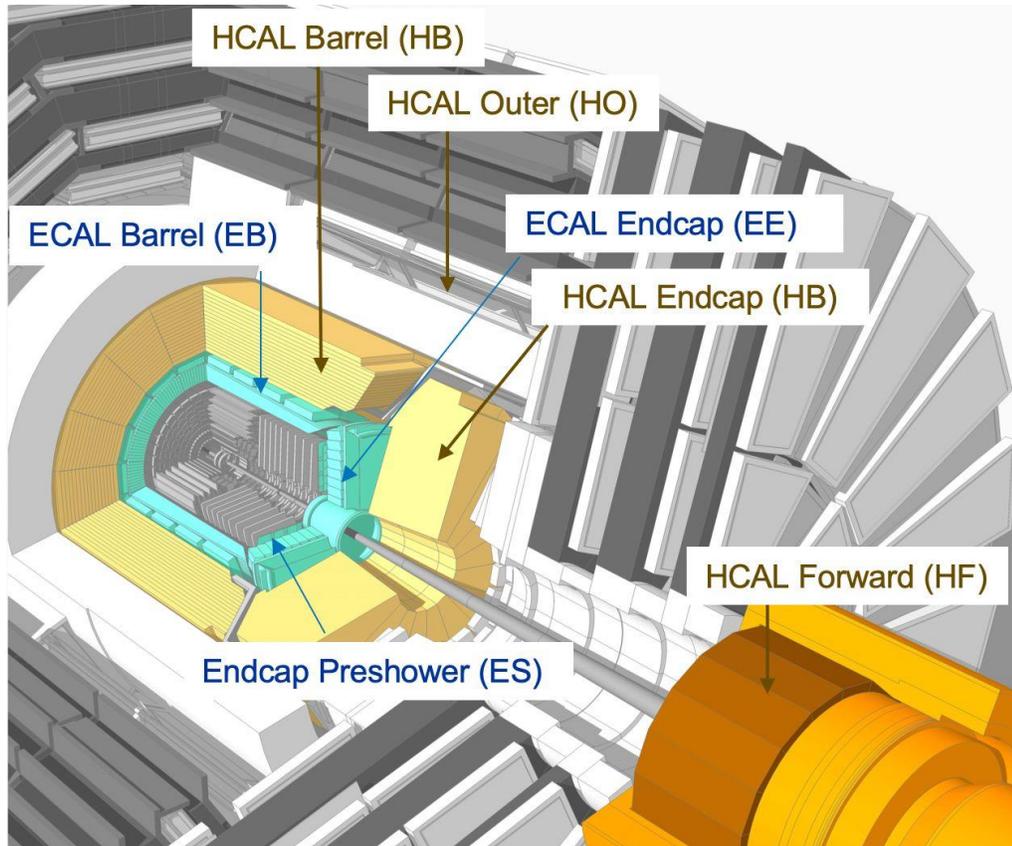
Figure 1.5: The Calorimeter system of CMS experiment: The closest one to the interaction point is electromagnetic calorimeter (ECAL) surrounded by hadronic calorimeter (HCAL). Forward Hadronic Calorimeter HF is at both end of endcaps (Barney, 2021)

Limitations

This thesis focuses on the refurbishment and upgrade of the calorimetry systems at the CMS detector. An important limitation of this research is that the luminosity of proton collisions at HL-LHC is very high, and therefore, both the calculation of the radiation damage to the detector and the elimination of pile-ups will be compromised.

This is because in the third operating period, which will serve as an acclimatisation period for the High Luminosity period after 2028 at CMS, much more pile-up events are expected than in previous operating periods. At the 13 TeV central collision energy, all collisions other than the one selected as the main collision, which occurs every 25 ns, are called accretions and cause significant damage to the detector. Depending on the number of accretions, the damage varies and quantification of this damage is of great importance before High Luminosity (HL-LHC).

On the other hand, there are also limitation for the upgrade of endcap calorimeter. There is a limit to the quality control of the silicon module component PCB (hexaboard), which must be taken into account during the quality control phase and ensures that there are no gaps between the modules. Due to the glued assembly and the fact that the boards or modules will operate at –30 degrees centigrade, the flatness of the hexaboard is critical. The flatness limit of the printed circuit boards is therefore 1.5 mm.

There are some limits on the IVCV measurements of the sensors to be used in HGCAL. The voltages of silicon sensors are measured up to 1000 V at HPK and up to 850 V at CMS institutes. In order to increase the electric field in silicon by increasing the bias voltage, measurements up to 1000V are provided. This minimises radiation damage and loss of charge collection efficiency.

However, since the leakage current (noise) increases with the bias voltage, the voltage is increased, but not too much. At the end of the HL-LHC, up to 800V is expected to be needed for 200 µm and 300 µm sensors and about 600V for 120 μm sensors. According to the specifications of the silicon sensors, the measurement condition must be a relative humidity of less than 60 per cent. The clean room laboratory at CERN is known to have high humidity from time to time. For this reason, at the beginning of the measurements, the probe station PM8 is washed with dry air to reduce the humidity and prevent discharges that may occur in the sensor. This method is used in case there is a correlation between discharges and relative humidity. To some extent, however, surface charges can be removed by applying an ion blower to the sensor before measurement, which can compensate for the lack of dry air in PM8. Measurements are therefore carried out at low relative humidity. This reduces both the current and the current variations over time.

CHAPTER II

Literature Review

In this section, the literature of this study is presented. There is a vast literature on radiation damage of particle detectors. In particular, the literature on radiation damage in scintillators and fibers is reviewed and the physics of silicon sensors is introduced.

Radiation Damage of the Particle Detectors

In experimental high-energy physics studies, the process of interaction of radiation with matter is well known (Knoll, 1999). The detection of particles is based on the detection of the interactions that occur when they encounter matter. These processes depend on the properties of both the particle and the detector material. What is measured is the calculation of the energy left by the particle in the detector, that is, in the active material (Grupen & Shwartz, 2008). The energies of charged particles are measured by measuring the absorption of particles by matter. This phenomenon manifests itself in different ways depending on the particle and its energy as well as the properties of the material that the particle interacts. Once the impact process is complete, the particle is characterized by looking at the energy loss and scattering angles. The main ways charged particles interact with matter, atomic ionization and excitation, Cherenkov radiation and Bremsstahlung (Frank & Tamm, 1937). The incoming heavy charged particles are generated through the Coulomb force with the nuclei and electrons of the material. Another mechanism for heavy charged particles is the excitation of electrons. If the incoming heavy charged particle has an energy is less than the ionization energy of the medium, the electrons in the active detector are excited to a higher energy level (Gorodetzky et al., 1995). After that, the excited atom or molecule emits a photon in the visible region and returns to its ground state or lower energy level. Such scintillation (Figure 2.1) or fiber materials are damaged by radiation exposure over time (Ahmed, 2007).
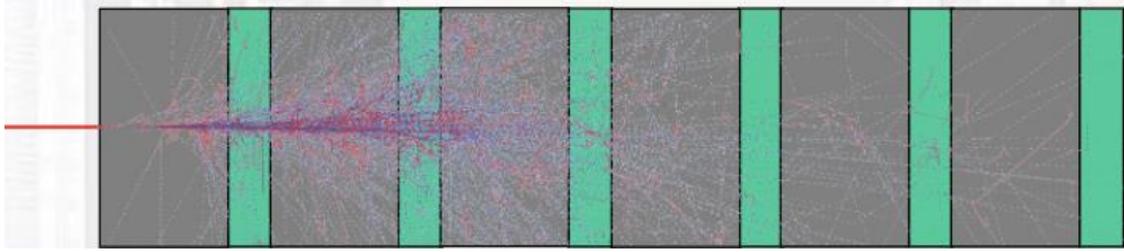
Figure 2.1: A sampling calorimeter consist of absorbers and scintillators as active element. The light collected from scintillators are carried to photo-detectors and produce an electrical signal.

The effects of radiation damage are usually caused by the color centers absorbing the scintillation light in the scintillators or fibers. This causes the reduction in the efficiency of the scintillators and fibers: This phenomenon is called radiation damage. (Wick et al., 1991).

The radiation damage in scintillators and fibers is complex and difficult to calculate in advance. It depends the material and the type of particle with which the material interacts, the total dose, dose rate etc. (Gusarov & Hoeffgen, 2013). Also, after exposure to radiation, it is expected a recovery process in scintillators and fibers, the time and amount of which again varies according to the parameters. This leads to uncertainty in the process of radiation damage assessments. For this reason accurate simulation of radiation damage is very difficult (Bross & Pla-Dalmau, 1992).

Dopants used in plastic scintillators must be stable, radiation tolerant and efficient. Without dopants, the attenuation length of the base plastic is low. In order to provide a longer attenuation length, a primary dopant that can strongly re-emit the absorbed energy at the wavelength at which the main plastic's light transmission amplitude is greatest is dissolved in the main plastic (Zorn et al., 1993). The effective parameters of radiation damage have been previously studied using many different scintillators and fiber materials (CMS Collaboration, 2018).

In these examples, it is generally observed that there is a threshold below which no damage is observed. Dose rate is an important parameter affecting radiation damage. Materials are exposed to a certain dose parameters such as exposure at different time intervals and the amount of oxygen in the air cause variations in the level of radiation damage in the material (Bicken et al., 1991). This topic is analyzed with studies on wavelength shifters (WLS) and plastic scintillators (Khachatryan et al., 2016). On the other hand, it was observed that the light loss for some scintillators was twice as high in samples irradiated in dry air than in those irradiated in an environment without oxygen (Bruning et al., 2004) . This can be considered as an indicator of the negative effect of oxygen during radiation exposure. The most important result obtained from these studies, as mentioned before, is that in the scintillator or fiber material it is very difficult to estimate the radiation damage, since it depends to many parameters such as the material content, the dose rate and atmospheric conditions etc (Hmayakyan et al., 2008). For this reason, the radiation-induced efficiency of scintillators used in detectors detecting the decline at regular intervals and compensating for this decline in the data received physics is very important in terms of the reliability of their analysis (Gorodetzky et al., 1995).

Silicon Detectors and Related Research

Using a silicon wafer is more advantageous compared to gas detectors because it generates a large signal at very short distances. The energy required to create an electron-hole pair is around 3.6 eV in silicon and around 2.85 eV in germanium, although this value is about 30 eV in gases (Hartmann, 2017). Silicon detectors are widely used in high energy physics experiments in the last decades. These experiments range from fixed target experiments to collider experiments (Aicheler et al., 2012). They are also used in many advanced spectrometry systems (e.g. in medical diagnostics) (Abashian et al., 2002). The rapid development of microelectronics in recent years has led to an increase in the quality of detector fabrication technology and an ease of fabrication of complex detectors. The reasons for the superiority of silicon detectors in both position and energy resolution can be summarized as follows (Hartmann, 2017):

1. Speed of around 10 ns.
2. Spatial resolution of around 10 μm.
3. Proportionality of the stored energy.
4. Good resolution of the stored energy (3.6 eV of energy is required to create a charge pair, compared to 30 eV for a gas detector).
5. Flexibility of design.

Semiconductors have conductive properties between metals and insulators. As an example, silicon (Si) is in group IV of the periodic table. A silicon atom has four electrons to make covalent bonds with neighboring atoms in the crystal.
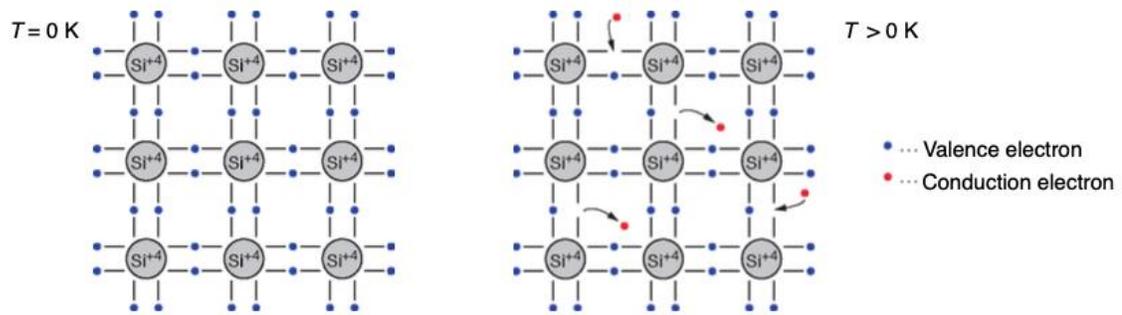
Figure 2.2: Atomic structure of silicon at 0 K and higher temperatures. When the temperature is higher than couple of degrees thermal vibrations breaks valence electrons and thus they become conduction electrons.

Here 4 electrons in the outer shell of each atom having closest neighbors are shared. And by that way they form covalent bonds. When the temperature is low electrons are bound but when the temperature is high the thermal vibrations break the bonds and this causes free electrons producing conductivity (Figure 2.2). On the other hand open bonds attract other electrons and this causes the "holes" change position which is called hole conduction.

Conductivity properties can be explained with the help of the energy band diagram shown in Figure 2.3. If the semiconductor is pure, the conduction band is completely free of electrons, but in this case the valence band is filled completely. The forbidden band

which is called energy band gap separates these two bands where there are no energy levels. In silicon sensors, if electrons are moved from the valence band to the conduction band by thermal means, there will be a current, due to the applied electric field. At room temperature the excitation energy must be more than 1.11 eV. This energy is called the band gap energy for silicon. For each electron which is moved to the conduction band, there is a missing electron in the valence band. This is called a hole. Both electrons and holes contribute to the current, again as shown in Figure 2.3. Conductivity can be greatly increased by the addition of elements such as As, Sb or P (Abbaneo, 2011). This is called doping. Those elements have 5 electrons in their outer shell. The fifth electron which is weakly bonded is available for conductivity. It rises to an occupied level, called the donor level, just below the conduction band as shown in Figure 2.4. These contributions are called donors because they can release an electron into the conduction band. Since the current in such materials is carried by electrons, they are known as n-type semiconductors (Abbaneo, 2004).
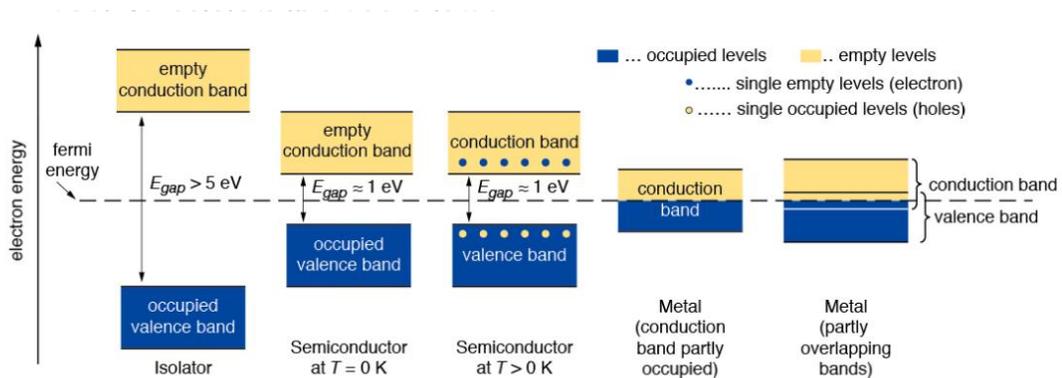
Figure 2.3: Energy bands of isolator, metals and semiconductors (Hartmann, 2017).

In a silicon sensor the conductivity can be increased by the addition of elements mostly group III of the periodic table, which have three electrons in their outer orbitals. Adding them, the three electrons covalently bond and a hole is formed. As shown in Figure 2.4, this leads to a not occupied region above the valence band (Hartmann, 2017). Conductivity happens when electrons are moved from the valence band to the acceptor level. Dopant atoms take electrons from the valence band. Such materials are known as p-

type semiconductors because the conductivity is the result of gap flow (Amendolia et al., 1980). In practical crystals there are regions of non-uniform structures due to the presence of dopants and missing or misplaced atoms in the lattice. Such regions are known as crystal defects (Bergauer et al., 2016).

Charged particles which traverse the detector cause electron-hole pairs. An electric field separates the electron-hole pairs and causing them drift to the electrodes. This is the signal of the detector. Signal to noise ratio is one of the most important parameter of a detector. The criteria for a good detector is a large signal and small noise. However for a large signal particles should produce many electron-hole pairs but this requires low ionization energy therefore small band gap. On the other hand, for a low noise the detector should not have more charge carriers which means should have large band gap. Therefore this creates an impasse for the detector design (Hartmann, 2017). For example, we can make a simple calculation for silicon with an average ionization energy

$$I_0 \approx 3.60 \text{ eV} \tag{2.1}$$

and for a minimum ionizing particle with an energy loss

$$dE/dx \approx 3.87 \text{ MeV/cm} \tag{2.2}$$

If we assume that our detector has a thickness of d = 0.300 mm and an area of

A = 100 mm^2 then the signal of a minimum ionizing particle in such a detector is:

$$\frac{dE/dx \cdot d}{I_0} = \frac{3.87 \cdot 10^6 \, eV/cm \cdot 0.03 \, cm}{3.62 \, eV} = 3.2 \cdot 10^4 \quad \text{e-hole pairs} \tag{2.3}$$

On the other hand, the charge carrier in the same volume at room temperature becomes:

$$n_i dA = 1.5 \cdot 10^{10} \, cm^{-3} \cdot 0.03 \, cm \cdot 1cm^2 = 4.5 \cdot 10^8 \text{ e-hole pairs} \tag{2.4}$$

Therefore, the electron-hole pairs thermally created are more than the ones produced by the signal by order of magnitudes (Casse et al., 2003). The solution is to reduce the number of charge carriers which can be done by a depletion zone in reverse

biased p-n junction. The p-n junction contains substrates which are *n* and *p* doped. In the doping process, some atoms are replaced by the atoms of the neighboring columns of the periodic table which have one valence electron more or less. Those replaced atoms create larger energy levels in the band gap and change the electron conduction. Doped n- or p-type semiconductors behave as conductors. The p-n junction is done joining p- and n-type semiconductors and it is responsible for the useful electrical properties of the semiconductor device. In a semiconductor device with a p-n junction, the majority carriers drift within the joint. This causes electrons to pass into the p-layer of the junction, filling holes, and holes to enter the n-layer and be annihilated by electrons. This creates an electric field across the joint (Figure 2.4). This field creates a contact potential V_0 between the two regions. The magnitude of the contact potential depends on temperature and dopant concentrations (Casse et al., 2008).

$$V_0 = \frac{kT}{q} \, ln \, \frac{N_A N_D}{n_i^2} \tag{2.5}$$

Here *kT* is the thermal energy, *q* is the charge of the electron. The donor and acceptor concentrations are N_A and N_D. The carrier concentration n_i is the concentration in the undoped semiconductor. This field also prevents the movement of charge carriers when equilibrium is established. Since electrons and holes are held in a covalent band structure within the joint, the joint has no moving charge carriers. This charge-independent region is called the displacement region, i.e. depletion zone. The electron-holes are pulled out of the depletion zone if we apply a voltage V between the cathode *p* and the anode *n*, then. Therefore the depletion zone becomes larger (Figure 2.5). In that way, the potential barrier becomes larger and diffusion is suppressed. The "leakage current" across the junction becomes very small. To give an example of a typical p-n junction, assume that the effective doping concentration *is* 10^{15} cm^{-3} in *p* region and 10^{12} cm^{-3} in *n* region, then without an external voltage, widths become

W_p = mm and W_n = 23,000 mm.

But if we apply a reverse bias voltage of 110 V, widths become

W_p =400 mm and W_n = 363,000 mm.
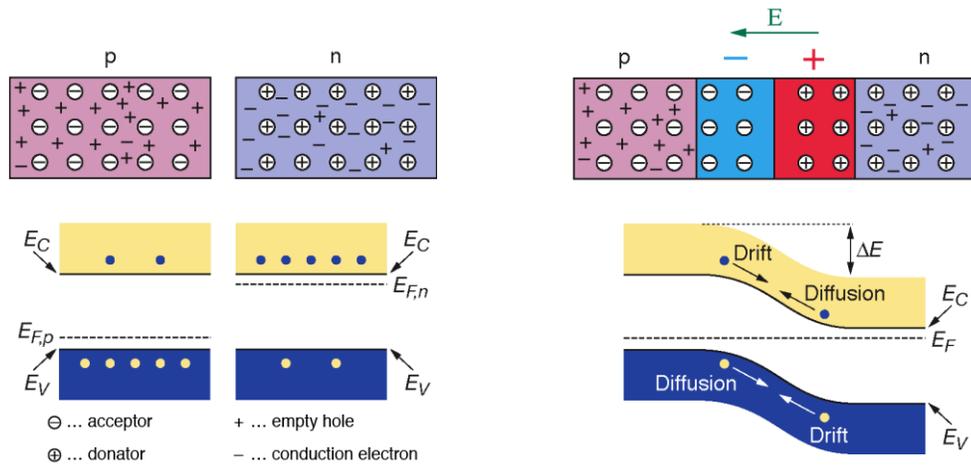
Figure 2.4: Energy gap and depletion zone created with p-n junction.
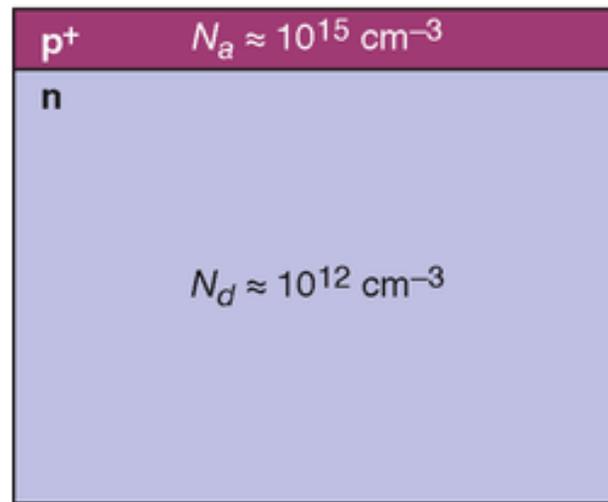
Figure 2.5: Width for a typical p+n junction.

In the bulk, the width of depletion zone is:

$$W \approx \sqrt{2\varepsilon_0 \varepsilon_r \mu \rho V} \tag{2.6}$$

where $\quad \rho = \dfrac{1}{e\mu N_{eff}}$

Here μ is the mobility of majority charge carriers, ρ is specific resistivity and N_{eff} is the effective doping concentration. This a typical way of a silicon detector configuration (Hartmann, 2017).

CHAPTER III

Methodology

In this section, the methodology for the solution of the problem is explained. Due to the radiation damage of the calorimeter systems a new calorimeter upgrade which is called high granularity calorimeter is proposed. There are methodological headings such as information on the methodology.

Radiation Damage of CMS Calorimeters

One of the most important problems of the CMS experiment for the HL-LHC is the higher particle "pile-up" in each LHC proton-proton collision event. This means higher instantaneous and integrated radiation doses hitting the detector elements. To solve this problem, CMS needs silicon sensors that can withstand the expected irradiation levels, a new high-speed trigger, and sub-detectors with higher detail or precise timing capabilities to help resolve pile-up events. Therefore, the electromagnetic calorimeter (ECAL) and hadronic calorimeter (HCAL) endcaps in the CMS detector will be replaced with High Granularity Calorimeter (HGCAL).

There are two types of calorimeters at CMS (Figure 3.1). These are the Electromagnetic and Hadronic Calorimeter (HCAL). Both are important components of particle detectors. The CMS electromagnetic calorimeter (ECAL) is designed to measure the energy of electromagnetic particles such as photons and electrons. These particles produce electromagnetic showers when they interact with matter. ECAL is made of transparent lead-tungstate crystals and is called a "homogeneous" calorimeter because it combines two functions in one material. Because transparent lead-tungstate crystals are so dense, they cause incoming particles to accumulate energy. In other words, when particles interact with matter, they produce electromagnetic showers through bremsstrahlung and pair production. They also scintillate with light detected by devices at the ends of the crystals, producing light proportional to the number of particles in the shower. But in the current electromagnetic calorimeter ECAL, lead-tungstate crystals lose

their transparency when heavily irradiated, reducing the amount of light that CMS can detect. How much radiation the crystals receive depends on where they are in the CMS. In the central, "barrel" part of CMS, the radiation is relatively low and the light loss is manageable, but for the HL-LHC, there will be a lot of radiation at the endcaps (Figure 3.3). Therefore, if the existing crystals are kept in the elevated collider, they will darken completely, reducing the amount of light that CMS can detect to almost zero. This is one of the reasons for replacing the ECAL endcaps for the HL-LHC. Another reason is that the HL-LHC will perform more collisions per second than the LHC because of the increased number of protons per beam. This means that every "image" CMS takes of collisions will be more complex. Therefore, much more granular detectors are needed.
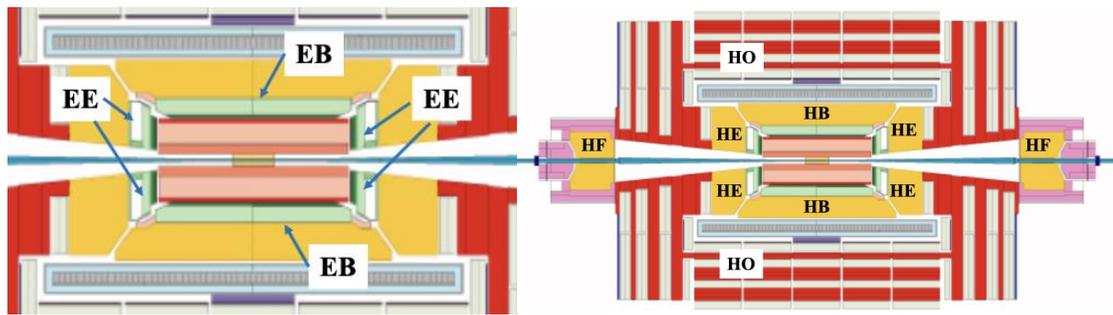
Figure 3.1: Cross sectional view of electromagnetic (ECAL) and hadronic calorimeter (HCAL) of CMS. At low eta region there are Barrel ECAL (EB) and Barrel HCAL (HB) and at high eta region, which is closer to beam line, there are endcap calorimeters of ECAL (EE) and HCAL (HE).

The crystals used in current ECAL endcaps have a cross-sectional area of about 3 cm by 3 cm and are insufficient to distinguish closely spaced particles in complex HL-LHC collisions (Figure 3.2). Because the crystals have only a single layer, "longitudinal" information on how showers develop cannot be obtained. For all these reasons, the ECAL endcap lead-tungstate crystals need to be modified to withstand the radiation at the HL-LHC.
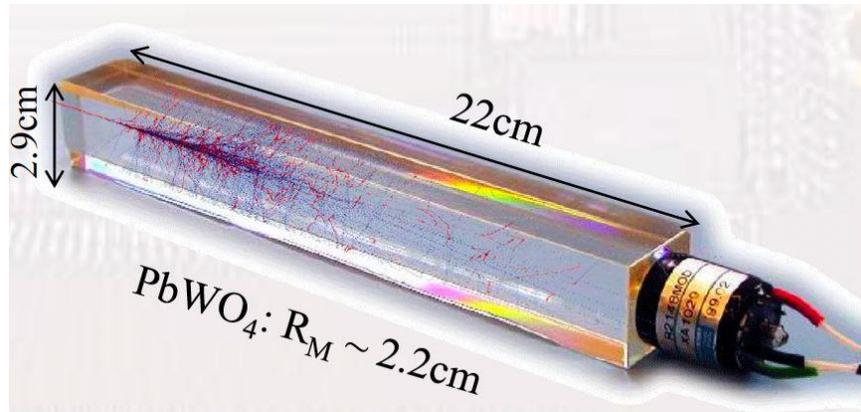
Figure 3.2: A lead-tungstate crystal of the electromagnetic calorimeter ECAL.
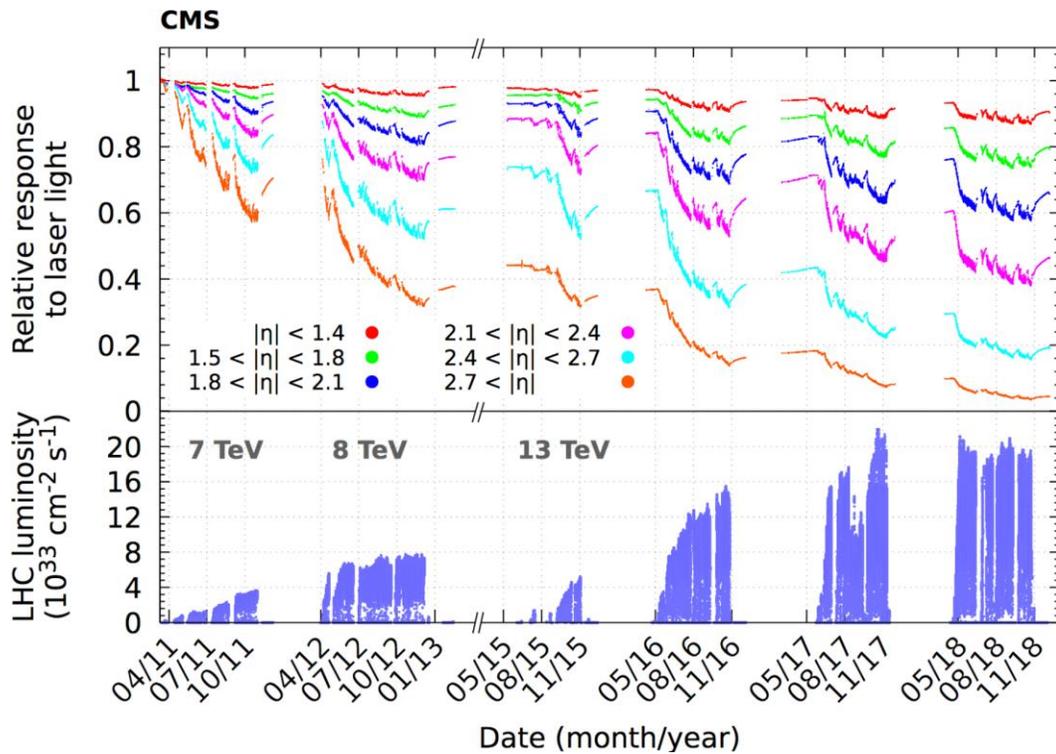
Figure 3.3: Radiation damage analysis done by laser light injected into the ECAL crystals, shows an attenuation up to 60% (Hayrapetyan et al., 2023).

Similarly to electromagnetic calorimeter, hadronic calorimeter (HCAL) of CMS as well is deteriorated after more than 10 years of LHC run. Proton-proton collisions in

the middle of the CMS creates lots of irradiation which bombard the sub-detectors. High eta region of CMS which is closer to beam line is affected more comparing to barrel region due to longitudinal proton collisions. Protons circulating in the LHC beam pipe are collided 40 million times every second, but few percent of those collisions are head-on. Most of the time protons are scraping each other and causing more particle flux close to beam pipe. Therefore, endcap detectors are getting more dose due to those collisions and they have more radiation damage (Figure 3.4) (Hayrapetyan et al., 2023).
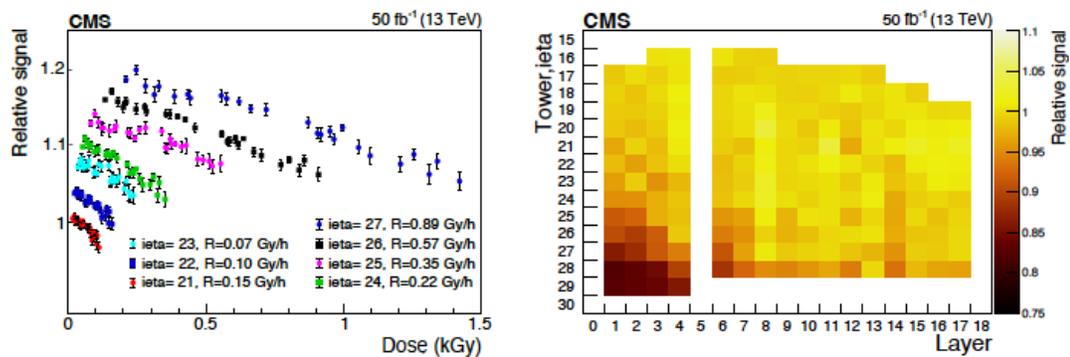
Figure 3.4: Relative signal of the hadronic endcap calorimeter (HE) is decreasing with the accumulated dose (Hayrapetyan et al., 2023).

HCAL is designed to measure the energy of hadrons such as protons, neutrons and mesons. Hadrons interact with matter primarily through the strong nuclear force, leading to the production of secondary particles (mostly pions) and particle showers. The energies of these particles are measured by the light emitted when they hit plastic scintillator tiles. At the HL-LHC, however, the HCAL endcap (HE) scintillators will darken due to radiation and stop producing light. HCAL's endcaps will therefore need to be replaced.

Finally, as it was expected, it is observed significant amount of radiation damage in the fibers of Forward Hadronic Calorimeter (HF) of CMS (Figure 3.5). In the analysis of radiation damage on HF fibers done at 2008, the darkening of fibers were shown

(Cankocak et al., 2008). Recent studies done about the radiation damage of HF found more than 35% radiation damage for high eta regions of HF calorimeter.
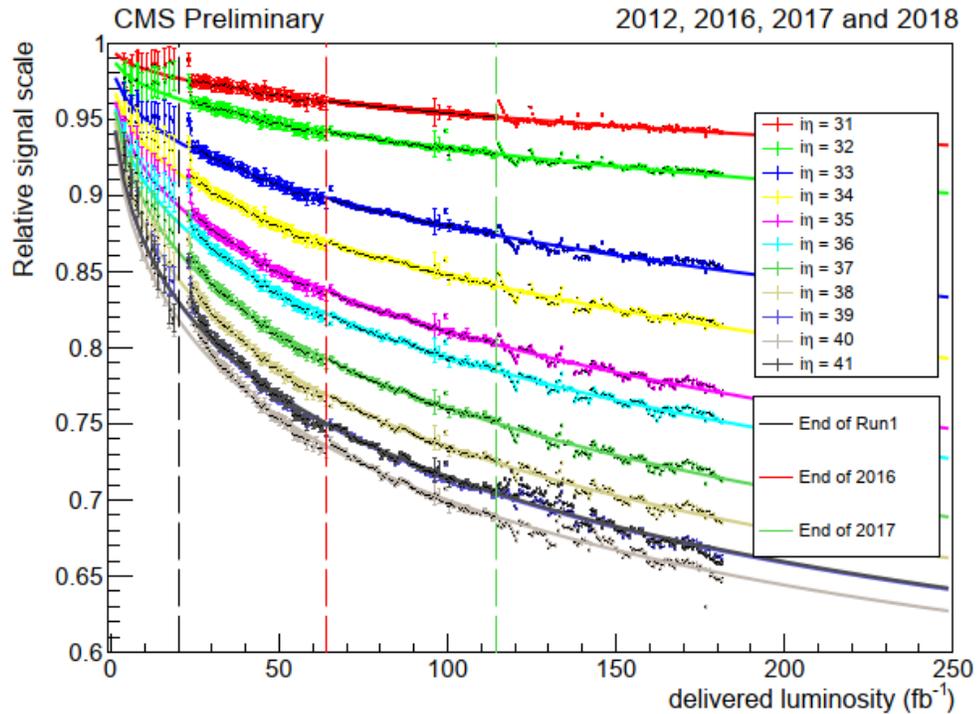
Figure 3.5: HF signal decrease in 2012, 2016, 2017 and 2018 as a function of delivered luminosity for different pseudo-rapidity (η) ranges.

Study case: HF Online RADDAM system

The hadronic calorimeter (HCAL) of the CMS detector is built to measure the positions and momentum of quarks, gluons and leptons, as well as the amount of missing energy. Measuring the missing energy is crucial for the detection and phenomenology of supersymmetric particles. The Forward Hadronic Calorimeter (HF) is close to the axis from which protons come and its front face is 11.1 m from the interaction point and it consists of steel absorber and quartz fibers as active material. Together with the area covered by the HF, a hermetically sealed detector is targeted. This will enable

measurements of the transverse energies (E_T) and missing energies of the jets and leptons resulting from proton-proton collisions. For the search for supersymmetric particles, loss energy and E_T measurements are of critical importance.

The radiation exposure of the HF detector is very high, and it is assumed that the part facing the proton-proton interaction point will accumulate a dose of approximately 100 Mrad per year. The online radiation monitoring (RADDAM) system is being used to measure such high levels of radiation in simultaneous measurements.
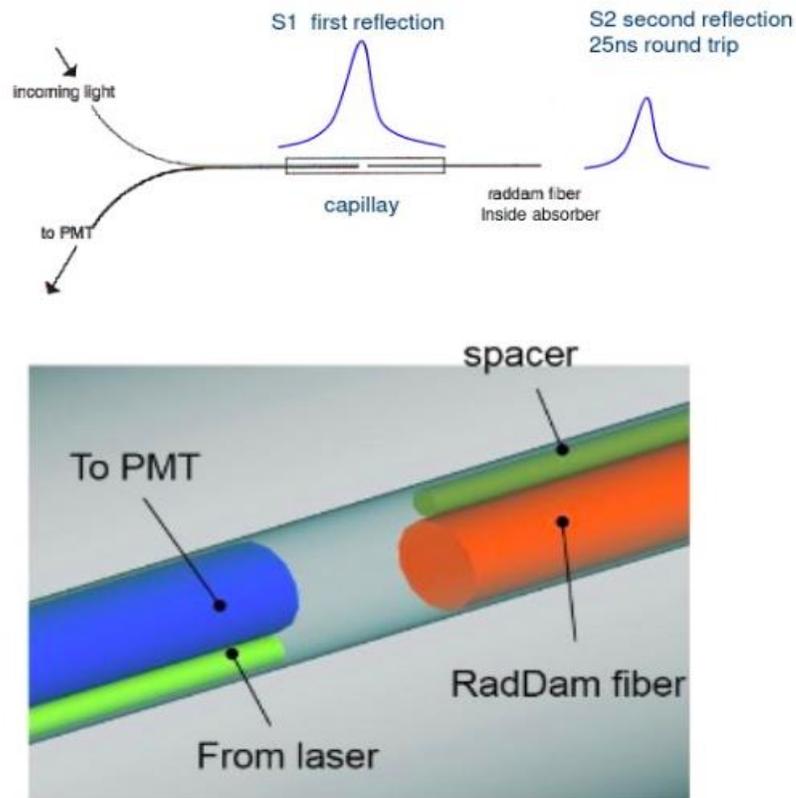
Figure 3.6: HF Online Radiation Monitoring (RADDAM) system consists of a Y-shaped fibers, which creates two signals from a light source, with a 25 ns time difference.

The fibers in the HF detector go to the photomultipliers. By disconnecting one fiber from the photomultiplier, placing a Y-shaped piece of fiber in between, and sending laser light to one end of this Y-shaped fiber, a signal is generated in the photomultiplier.

The other end of the Y fiber is connected to the fiber inside the HF. This 1.2 m long fiber crosses the HF detector and goes all the way to the other end of the detector. The difference between the first and second signal in HF RADDAM fibers is shown in Figure 3.6. In this region, which is most exposed to radiation, the light reflected from the end of the fiber returns back to the photomultiplier. This results in two signals separated by 25 ns in the photomultiplier. Based on the principle that as the amount of radiation increases over time, the light reflected from the free end of the fiber will decrease, while the light reflected from the end of the fiber connected to the photomultiplier will be relatively less affected since it will receive much less radiation, it is possible to determine the amount of radiation incident on the front face of the HF from the ratio of these two signals.

The Y-shaped fibers have been installed to both end of HF having 56 channels in total (Figure 3.7). The RADDAM system, which has been retrofitted to the HF, has been used in the CMS experiment since 2007. Since 2007, the RADDAM system has been integrated into the CMS data acquisition system and it has been possible to simultaneously determine how much radiation damage the fibers have received.
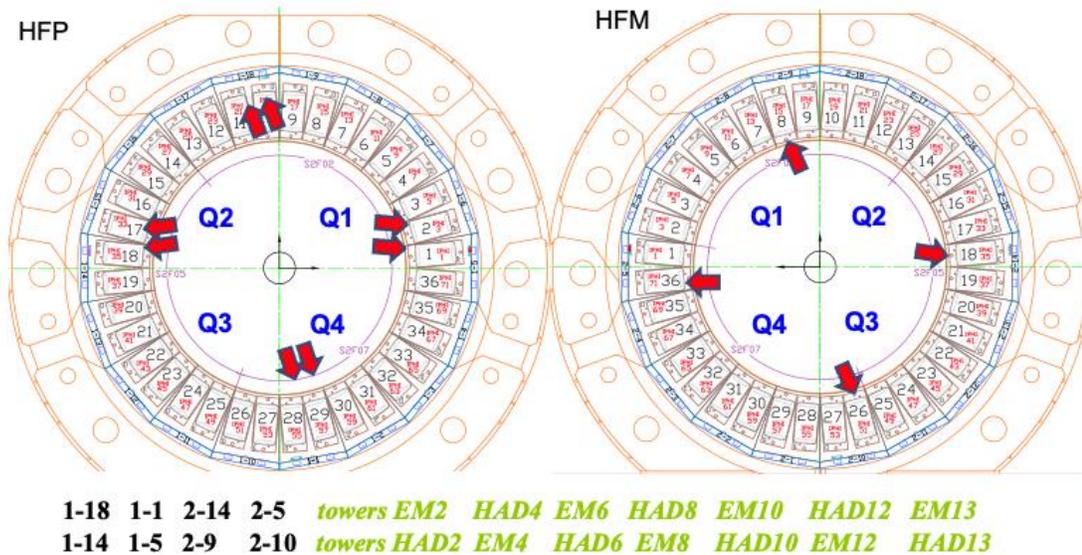
Figure 3.7: 56 channels of RADDAM fibers are installed to both end of HF.

In 2022, during the third run of the LHC accelerator (Run3), it was analyzed whether the RADDAM system worked successfully at high radiation and the effects of increased proton energies and luminosity on HF fibers. The first reflected light at the end of the RADDAM fiber is read by the Photomultiplier Tube (PMT) and labeled S_1 in the analysis. The remaining light from the front end travels to the far end and is reflected off the polished surface. This signal reaches the PMT 25 ns later (later than S_1) and is labeled S_2 in the analysis. Ideally, 50% of the incoming signal should pass through the fiber and 50% should be reflected at the front end, so the ratio of S_1 and S_2 could be greater than 1 (Figure 3.8).
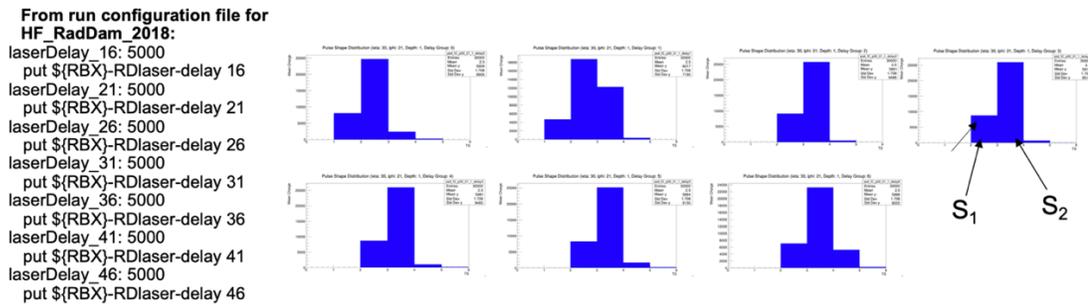
Figure 3.8: The ratio of S_2/S_1 is decreasing with the accumulated dose in HF fibers and thus indicates the radiation damage.

HF RADDAM measurements were performed with the HCAL laser system until 2018. However, the HCAL laser produces wide pulses. Therefore, since S_1 and S_2 are distributed over three time periods (wider than desired), it was difficult to analyze. During the Phase-1 upgrade of HF, a new laser system customized for HF RADDAM was introduced. The aim is to extract unwanted events using Time-to-Digital Converter (TDC) data from the Charge Integrator and Encoder (QIE), a front-end chip used in the readout electronics of the CMS HCAL. This provides a narrower and sharper signal. To see S_1 and S_2 in separate but consecutive time slots, especially in the second and third time slots. In short, with the new laser system you get 3500 events per run. The 7 different delay times are covered by 5000 events each. Attenuation is minimal and damage recovery is maximum between 400 nm and 520 nm. PMTs in HF calorimetry that detect Cherenkov

light are sensitive in the 400 and 500 nm light range, where damage recovery is maximum (Figure 3.9). For this reason, 450 nm light is used by RADDAM laser (Cankocak et al., 2008).
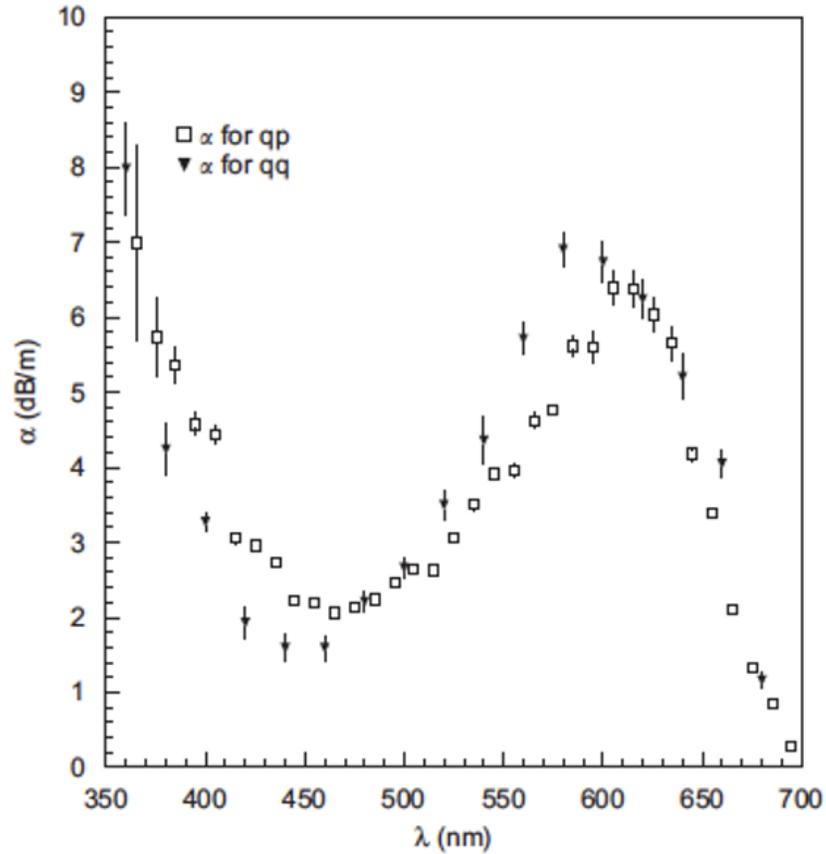
Figure 3.9: Attenuation measurement of HF fibers for different wavelengths (Cankocak et al., 2008).

The first step in the RADDAM analysis is to select the right delay time slices, so the function must be maximized.

$$\frac{Q_1 + Q_2}{Q_t} \tag{3.1}$$

Q_1 is the total charge in the second time slot (TS$_2$).

Q_2 is the total charge in the third time slot (TS$_3$).

Q_1 and Q_2 are summed and divided by the total charge in 'all time slices' in a single event (Q_t).

The laser runs taken with different phases helps us to find the best window to maximize this ratio (Figure 3.10).
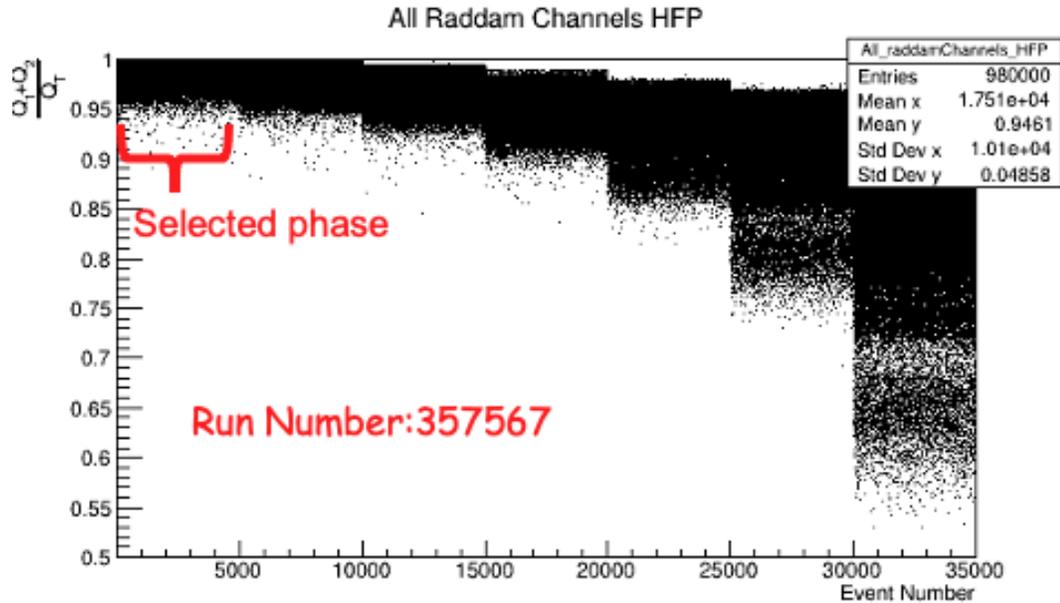
Figure 3.10: The ratio Q_1+Q_2/Q_T is used to determine the best laser phase.

After the irradiation has ended, a slight recovery occurs in a few minutes. The signal ratio is therefore depends on both the accumulated radiation dose and the time 't' after irradiation. The radiation hardness of quartz fibers is measured using 500 MeV electrons up to 50 Mrad and 24 GeV protons up to 1.25 Grad. For comparison, 1.25 Grad of radiation is equivalent to approximately 12 years of HF operation at the LHC. Below 0.6 Grad, the signal shows high degradation in the 550 nm to 680 nm range or below 380nm. During Run3 of LHC, until the end of August 2022 CMS recorded 8.44 fb^{-1} of Luminosity from proton-proton collisions and is it clearly observed the recovery of fibers during a short shut down period of LHC during the middle of August 2022 (Figure 3.11).

During the Run3 period almost 30 fb^{-1} integrated luminosity is recorded at CMS. I have analyzed HF Online Raddam channels from the data taken at local runs during this

period and observed between 2-15% signal reduction due to the radiation damage. As it is shown in the plot below (Figure 3.12) the signal reduction is much higher at high eta regions since this region is closer to the beam line. High eta RADDAM channel shows a signal reduction up to 15%. The next step should be to extrapolate these measurements to the higher luminosities and to compare the results with the data taken 2023 and 2024.
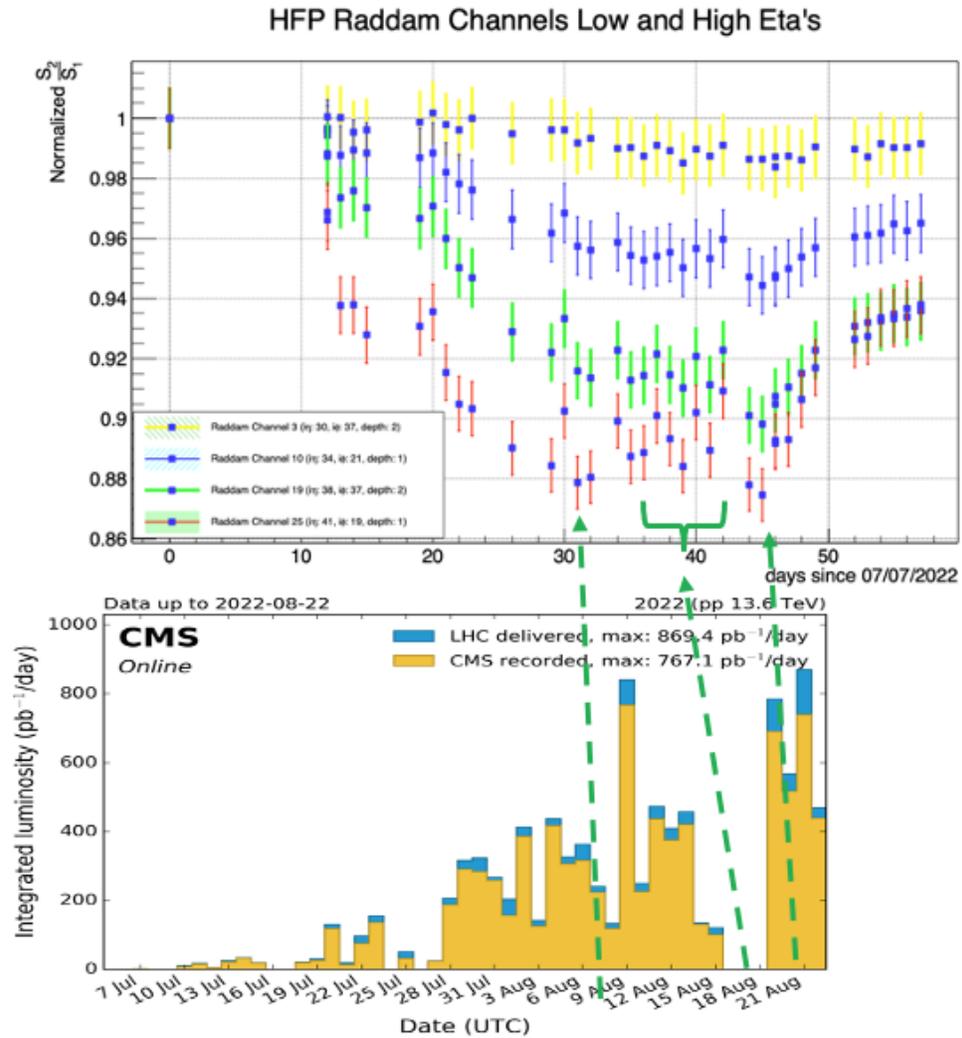
Figure 3.11: The radiation damage of the HFP fibers with the accumulated dose from proton-proton collisions during Run3 of LHC.
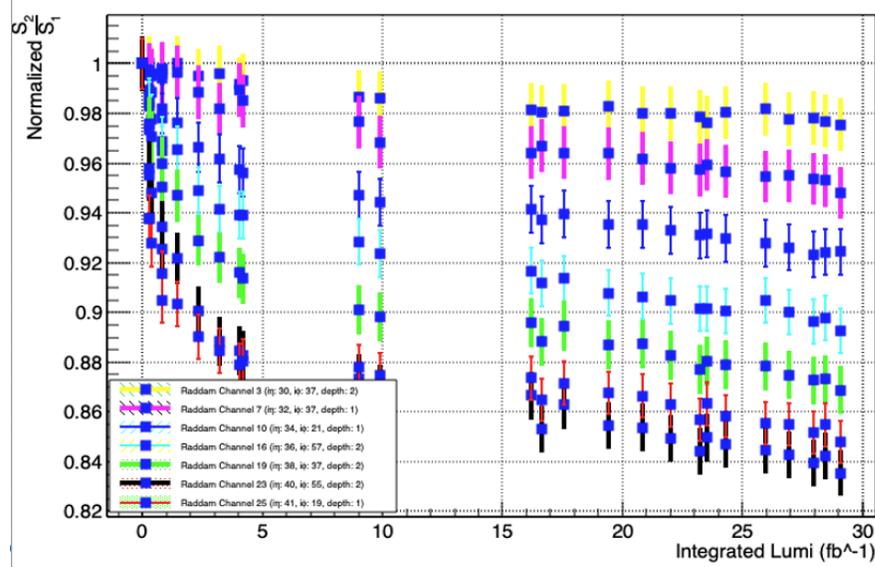
Figure 3.12: The signal decrease observed at HF fibers during the proton collisions of 2022.

Motivation for HGCAL

Scintillators are the type of active medium widely used in the calorimeters in all detectors around the world, especially in the LHC experiments (CMS, ATLAS, LHCb and ALICE Experiment). The CMS detector has a calorimeter system based on sampling, either with crystals (ECAL) or scintillators (HCAL). The initial structure of these crystals and scintillators, based on LHC parameters, is reaching the end of its lifetime and poses serious performance problems in terms of their resistance to radiation from collisions with the emergence of high beam intensity Phase-2 plans. As part of the HL-LHC upgrade program, the CMS collaboration has designed a High Granularity Calorimeter (HGCAL) to replace the current endcap calorimeters (Figure 3.13) (Azzi et al., 2017).

The High-Luminosity LHC (HL-LHC) will integrate 10 times more luminosity than the LHC, posing significant challenges for radiation tolerance and event stacking in detectors, especially for advanced calorimetry, and flagging the issue for future colliders. Due to this high luminosity, the pile-up events also will be increased by a factor of 5-10. At LHC every 25 nano second two bunch of protons each having billions of protons

moving in opposite directions are colliding. During those collisions not only one but several hundreds of protons are colliding although it is selected only one collision (40 MHz rate). The other collisions than the selected collision in 25 ns window are called pile-up events and the contribute to the LHC data as background or noise. In order to identify particle coming from the selected proton-proton collisions one has to eliminate of those pile-up events from the data. Since the original design of CMS based on the LHC parameters didn't foresee that much amount of pile-up, the present granularities of the ECAL and HCAL is not enough to separate the pile-up events from the selected ones. Being a high granularity calorimeter, this is one of the main motivation of HGCAL (Azzi et al., 2017). To deal with high number of pile-up events is necessary to have high granularity detector.

HGCAL features unprecedented transverse and longitudinal segmentation for both the electromagnetic (ECAL) and hadronic (HCAL) compartments. This will also facilitate particle flow calorimetry where fine structure can be measured within the particle shower and used to improve aggregation rejection and particle identification while still achieving good energy resolution (Figure 3.14).

Studies on radiation damage measurements of the CMS HCAL detector have shown that the scintillators in the CMS endcap hadron calorimeter have suffered more damage than expected. It shows that it is important to understand that the total dose of radiation received by the scintillators, as well as the rate of uptake, is responsible for this damage. The CMS experiment is thus conducting an intensive program of Phase-2 improvements for the endcap calorimeters (Hmayakyan et al., 2008). A new set of silicon active layers will be used for the endcaps of electromagnetic and hadronic calorimeter parts of the CMS High Granularity Calorimeter (HGCAL) and scintillators for the barrel part of hadron calorimeter.

The CMS Calorimeter Endcap will consist of an electromagnetic (CE-E) and a hadronic section (CE-H). The electromagnetic section will consist of 26 sensitive layers interspersed with Cu, CuW and Pb absorber plates (Pitters, 2019). It will have a total depth of 27.7 radiation lengths (X_0). The hadronic section will consist of 21 sensitive layers,

interspersed with steel as a passive material. Silicon will be used as the active sensor material in the detector areas exposed to high levels of radiation.
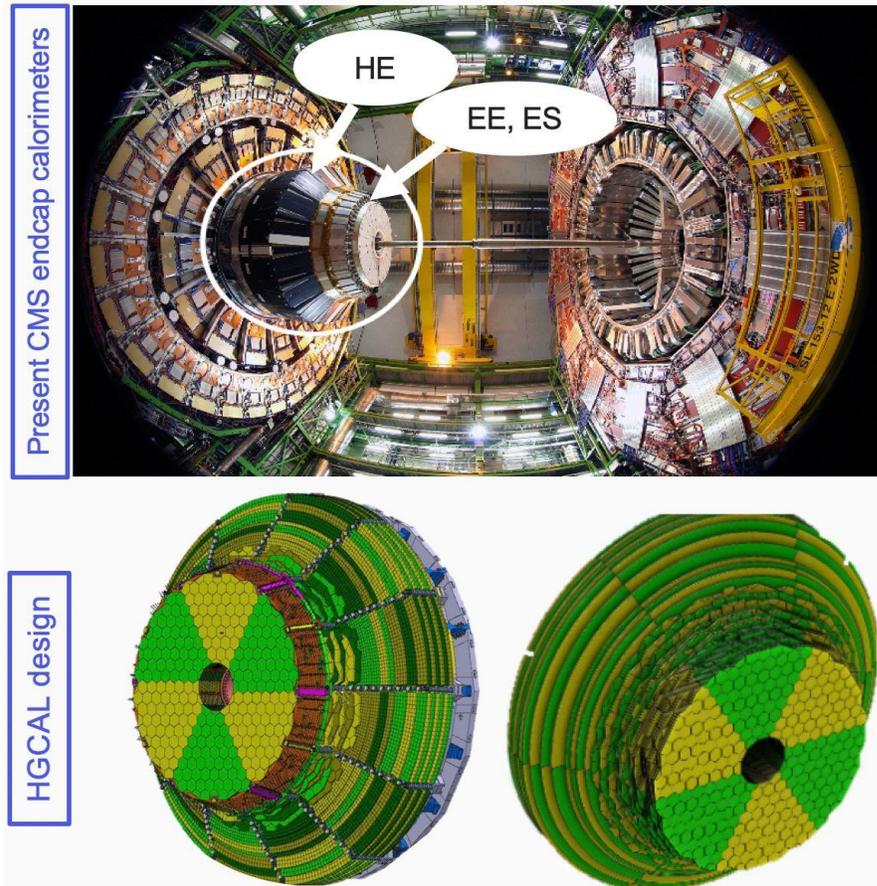
Figure 3.13: Endcap calorimeters of CMS (HE, EE and ES) will be replaced by HGCAL.
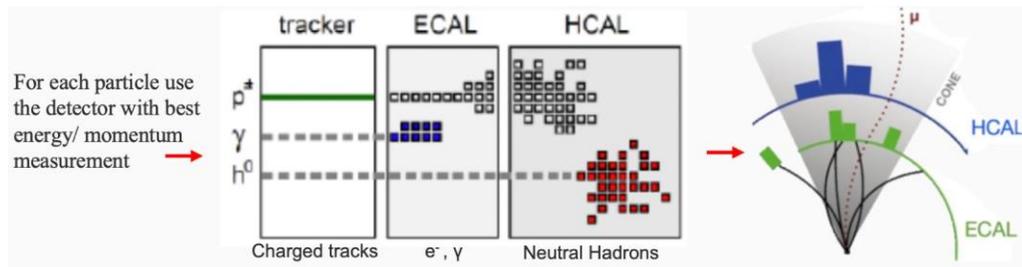
Figure 3.14: Demonstration of the particle flow in CMS detector. In order to follow the energy released by particles coming from the interaction point, the tracker and the calorimeters should be well aligned.

At the same time, silicon provides fast signals that allow time measurements of energy deposits with the precision necessary to effectively reject pile-up. For this reason, silicon sensors will be used throughout the electromagnetic compartment and in the high-radiation inner part of the hadronic compartment. In CE-H, in areas with relatively low radiation levels, scintillation will be used as the sensitive material.

Design of HGCAL

HGCAL will consist of 620 m^2 of silicon sensors and 370 m^2 of scintillators. The best way to divide a surface into regions with an area at least equal to the total perimeter is to use a silicon sensor with a hexagonal geometry. Therefore, a hexagonal geometry is chosen for the silicon sensors and an 8-inch sensor will be used to reduce the number of modules (Acar et al., 2023). The bulk of CE-E and CE-H will be based on hexagonal silicon (Si) sensors with a cell size of 0.5-1.2 cm^2 and the rest of HGCAL will be based on high segment scintillators with SiPM readout (Kronheim et al., 2024). Design cross-section of the HGCAL is shown in Figure 3.15. The inherent high-precision timing capabilities of the silicon sensors will add an extra dimension to event reconstruction, especially in terms of mass rejection.

HGCAL's wedge-shaped structures are called 'cassettes' and will use 26,000 silicon modules. The silicon module will be used to create sandwich structures containing four components. Figure 3.16 shows the low-density silicon module. The first component of the silicon module is the printed circuit board (PCB), called hexaboard, which contains the electronics and connectors. The PCB is connected to the motherboard for data transfer. Data is transmitted through the second part of the module, the silicon sensors (Akchurin et al., 2018). After the second layer there is a Kapton sheath used for electrical insulation between the components. The last layer is the base plate to provide mechanical support. It also acts as a heat sink to dissipate heat from the sensors or electronics. The cassette containing the silicon module is shown in Figure 3.17 (a) (Azzi et al., 2017).
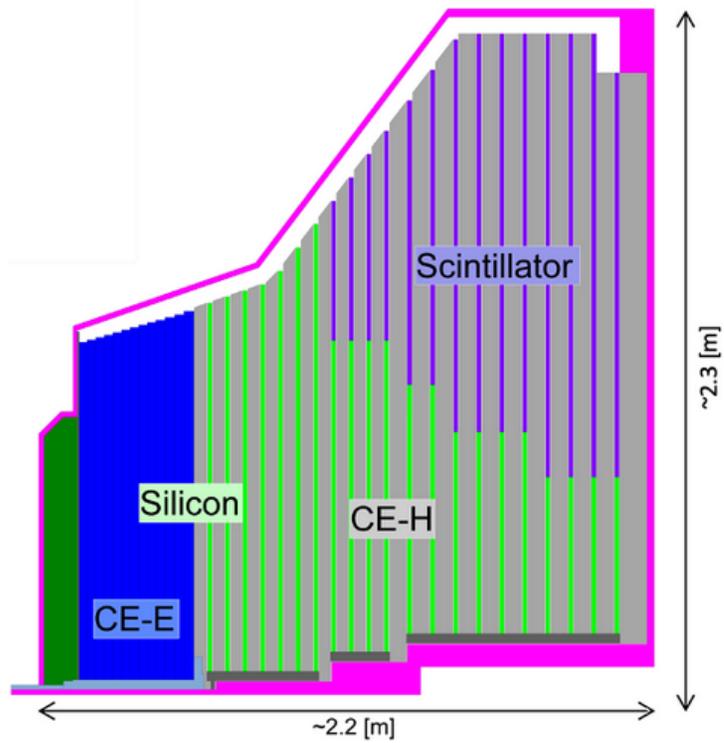
Figure 3.15: Cross section of the design of the new calorimeter, the High Granularity Calorimeter (HGCAL). The Electromagnetic (CE-E) compartment is indicated in blue, while the Hadronic compartment (CE-H) is shown in green (Barney, 2022).
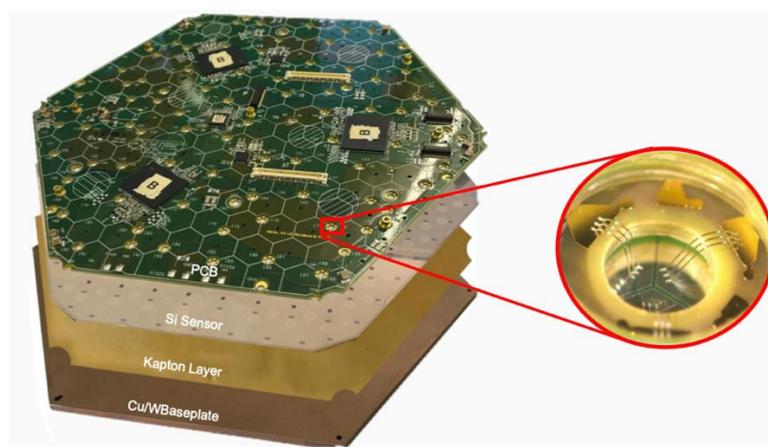
Figure 3.16: Silicon module of the HGCAL. Example of a silicon-based module, 8 inch and low-density (LD).

HGCAL will use three different thicknesses of silicon sensors. The center of the cassette is the high-density area where the high-density (HD) sensors will be used. These sensors have 432 channels and active thicknesses of 120 and 200 μm. HD has a pad size of 0.5 cm^2. However, the outer area has a lower density. Therefore, low-density (LD) sensors will be used. The active thickness of LD is 200 μm and 300 μm. Each of these sensors has 192 channels and a pad size of 1.2 cm^2 (Brondolin, 2020). The different zones in the Electromagnetic Section (CE-E) are shown in Figure 3.17 (b).

(a)   (b)
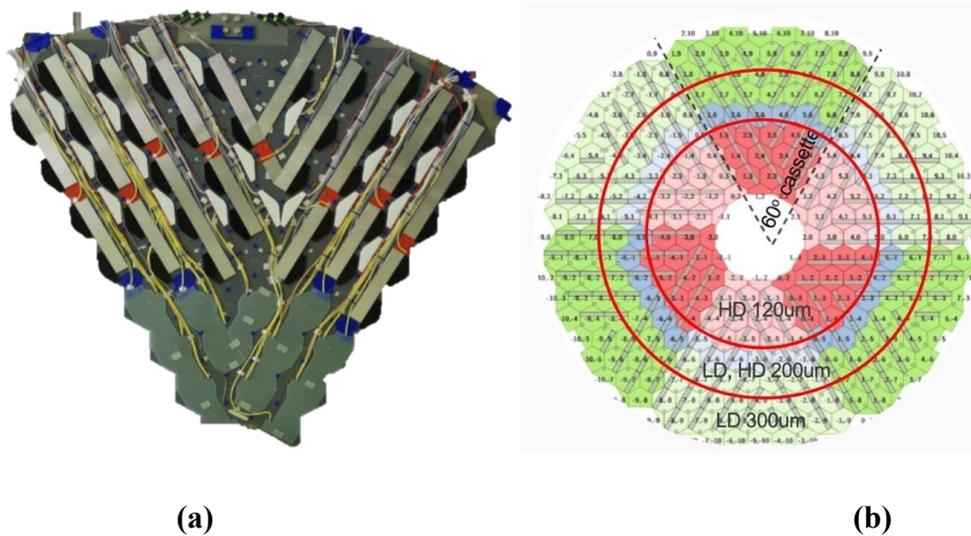
Figure 3.17: (a) HGCAL Silicon Cassettes (b) Different regions in CE-E.

The modules to be used in HGCAL will be operated at –30 degrees Celsius. This ensures reliable operation of the silicon modules after irradiation and keeps the energy equivalent of the electronic noise low enough. The PCB glued onto the sensor has hexaboard quality control requirements. Hexaboard contains passive components (connectors, resistors and capacitors) and ASICs. Signals from the sensor pads are provided by on-board signal digitization readout chips. Like silicon sensors, hexaboards have "low-density" (LD) and "high-density" (HD) types. The 8-inch boards include variants that differ in the number of holes and the number of ASICs (Strobbe, 2022). The LD hexaboard has three ASICs spaced 0.8 mm pitch, while the HD hexaboard has six ASICs spaced 0.6 mm pitch (Bouyjou et al., 2022). The 'stepped hole', achieved with two

holes, is present in large numbers in both versions and allows the aluminum wedge wire to be connected to the silicon sensor underneath. It also minimizes the overall height of the assembly. The sematic representation of the first and second hole forming the stepped hole is as shown in Figure 3.18.
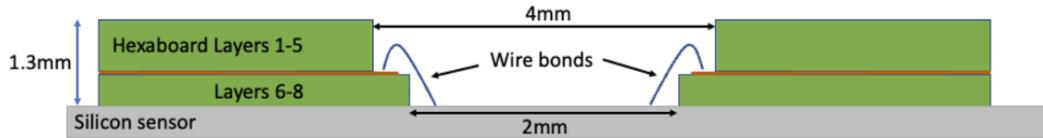
Figure 3.18: Diagram of a stepped hole in hexaboard. The first hole forming the stepped hole is 4 mm in diameter in layers 1 to 5. The second, in layers 6 to 8, is 2 mm in diameter.

In a hole containing six connection pads, three of them are for connecting between the sensor cell and the front-end chip (HGCROC) input channel. The other three connect to ground on the hexaboard. So, if a sensor cell is showing a really high leakage current, we can ground it so that the current does not affect the other cells. Figure 3.19 (a) is a photograph of a stepped hole showing the wire bonding pads. Figure 3.19 (b) shows the aluminum wire connections to the silicon sensor glued to the bottom of the hexaboard.

(a)   (b)
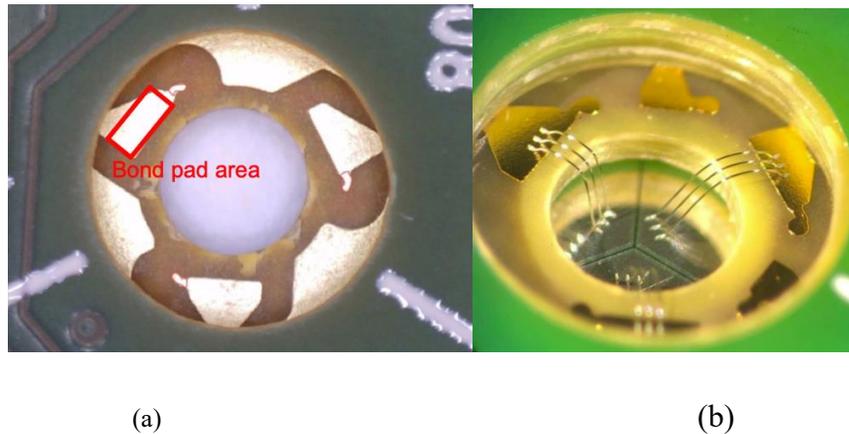
Figure 3.19: (a) Stepped hole showing the wire bonding pads. The bonding pads in the stepped holes are expected to be free of glue. (b) Image showing aluminum wire connections from PCB to silicon.

There are several critical acceptance criteria for hexaboards. The accepted mechanical description for hexaboards is as in Table 1.1. Firstly, they are visually inspected. The LD boards produced by two Indian companies (Hi-Q and Micropack) are inspected using various microscopes at CERN. For pre-series boards, all of them are visually inspected. For pre-production boards, the first 100 boards are visually inspected, then the rest are randomly selected at a level of 1-5%. A "traveler" document is used for visual inspection at CERN. Each board must have a batch number and an individual board number (ID). The PCBs are numbered with a special labeling. Table 1.2 shows example labels for hexaboards.

The following labeling scheme makes it easy to distinguish hexaboards:

$$320 - MM - TTT - VA\ NNNNN$$

1. MM is used to distinguish between high-density and low-density boards. Low-density (LD) is indicated by 'XL'. High-density (HD) board is indicated by 'XD'.
2. First digit for cut type, (T_1): Full (F/0), Top (T/1), Bottom (B/2), Left (L/3), Right (R/4), Five (5/5).
3. The middle character (T_2) represents the version of the board. Prototype versions of the PCB: 0, 1, 2 and 3 are indicated by generation IDs. Pre-production and production boards are identified by generation 4.
4. The last character (T_3) indicates the version (package type and chip version) of the read-out-hexaboard chips (HGCROC). It also indicates an indicator ("U" or '0') that the hexaboard is not currently assembled for use in the database.
5. V, the first of the last seven characters indicating the serial number of the hexaboard, represents the PCB manufacturer. There is a unique label for each vendor and is indicated in this digit.

The label for each vendor is listed as:

1. P/1: Represents the Plotech PCB vendor.

2. Q/2: Represents HiQ PCB vendor.

3. M/3: Represents Micropack PCB vendor.

4. A, the second of the last seven characters of the hexaboard serial number, identifies the assembly vendor of the PCB (use "U/0 " for unassembled boards).

Special labels are used for existing assembly vendors. These are:

1. H/1: Indicates the hybrid SA PCB assembly vendor.

2. P/2: Indicates Plotech PCB assembly vendor.

Table 1.1.

The Mechanical Description Table Contains the Acceptance Limits for Hexaboards

External size (full hexagons)	221.2 mm × 201.4 mm ± 0.1 mm
Thickness (can be discussed with CERN)	1.3 mm ± 0.2 mm
Number of layers	8

Table 1.2:

Table with Sample Labels and Descriptions for Hexaboards

Label	Description
320-XL-F4U-QU-00201	Full LD pre-production hexaboard with serial number 201 produced by HiQ
320-XL-F44-MH-00723	Full LD pre-production hexaboard with serial number 723 produced by Micropack and assembled by Hybrid SA with S04-packaged HGCROCV3b ASICs
320-XL-L42-QH-00018	LD Left pre-production hexaboard with serial number 18 produced by HiQ and assembled by Hybrid SA with S02-packaged HGCROCV3b ASICs
320-XH-T4C-PP-00078	HD Top pre-production hexaboard with serial number 78 produced by Plotech and assembled by Plotech with HGCROCV3c ASICs

Quality Control Steps for LD Hexaboard:

There are several steps to check if a hexaboard is in good shape, suitable for design parameters. Those steps can be summarized as below:

No glue seepage into the stepped holes:

Since the gold pads in the sixth layer will be used for wedge-wedge aluminum wire bonding, they must be free of any residue. Therefore, the hexaboard with gold bonding pads in the "stepped hole" is checked before it is assembled with passive components (connectors, resistors and capacitors) and ASICs. Figure 3.19 (a) also shows clean wire bonding pads.

Flatness of the boards:

The flatness of the hexaboard is critical as the silicon modules will operate at –30 degrees Celsius. The total thickness of each PCB is 1.3 mm ± 0.2 mm. A 'Feeler Gauge' is used to measure the flatness of the hexaboard (Figure 3.20), while a 'Vernier Caliper' is used to measure its thickness (Figure 3.21).
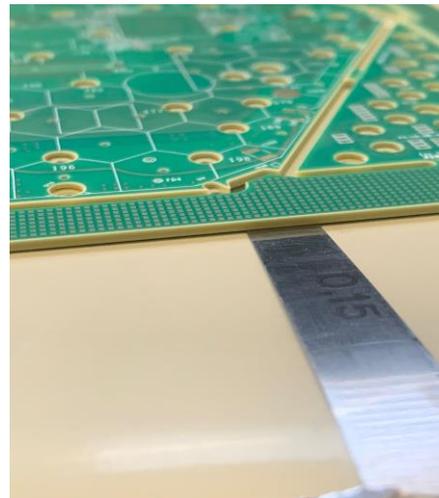
Figure 3.20: A practical demonstration of the board with the Feeler Gauge, which measures the flatness of the board.

Figure 3.21: A practical demonstration of measuring the thickness of a board with a Vernier Caliper.

Test Coupons check for No delamination after thermal Shock & Cycles:

It is imperative that no delamination of the hexaboard occurs under thermal stresses. For this reason, a test coupon is available for destructive testing without damaging the hexaboard. Test coupons are available with the new boards (version V1.3). There are three test coupons per board. Each test coupon must have the same ID printed on it as the main hexaboard. There is also a type of daisy-chained vias, where a voltmeter is used to measure the continuity to check if the via quality is good. At CERN, thermal shock tests were performed on test coupons and some complete boards. As shown in Figure 3.22, the boards were passed through the oven normally used for solder components. First, they went from 20 degrees (room temperature) to 240 degrees, then back to 20 degrees. This cycle was done ten times, although the industry recommends doing it five times. The cycled test coupons and boards were once again visually inspected. The results of the visual inspection showed no signs of delamination of the boards and no breakage of the daisy chain screws tested with a multimeter.
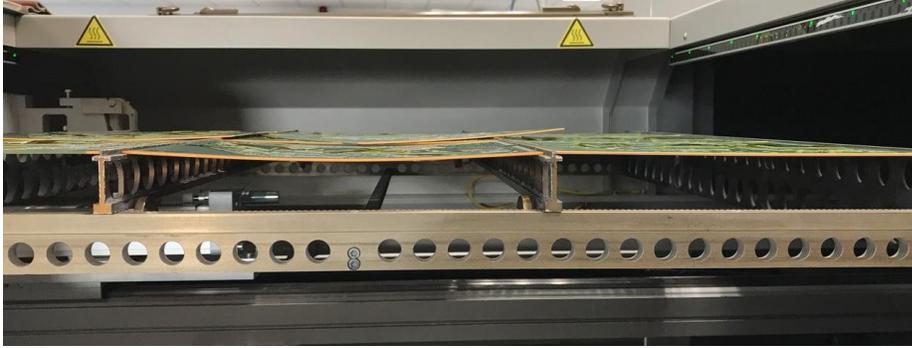
Figure 3.22: Hexaboard cycling with the oven normally used for solder components.

In 2024, 163 pre-production boards were visually inspected and analyzed. A graph showing their thickness and flatness according to the manufacturers was produced. 44 complete hexaboards manufactured by Micropack were analyzed. All of them were within the acceptance criteria but one board was found to be uneven and was rejected for this reason. Figure 3.23 (a) shows the thickness measurement results of the Micropack boards, (b) shows the distribution of irregularities. In addition, 119 complete hexaboards manufactured by Hi-Q were analyzed. All boards passed the acceptance criteria. Figure 3.24 (a) shows the thickness measurement results of Hi-Q boards, (b) shows the non-flatness distribution.

(a)

(b)
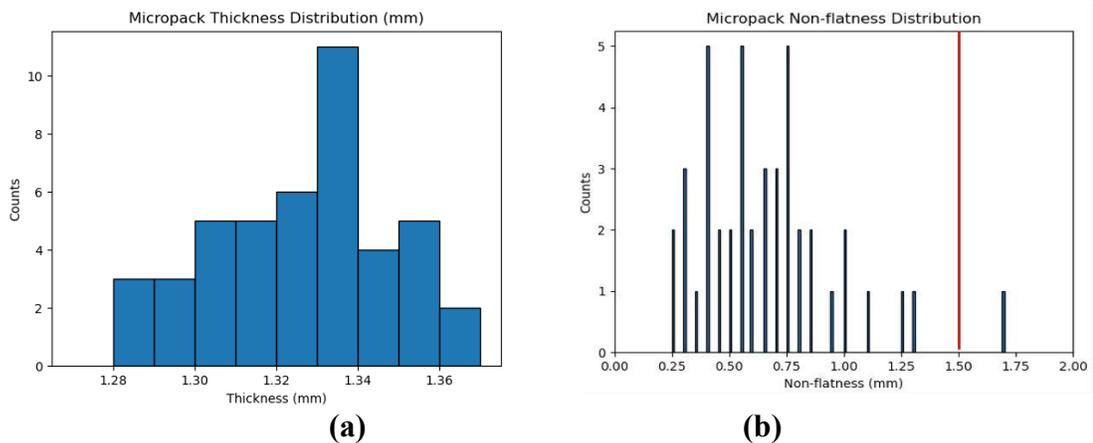
Figure 3.23: Thickness measurement results (a) and (b) non-flatness distribution of Micropack boards measured in millimeter.
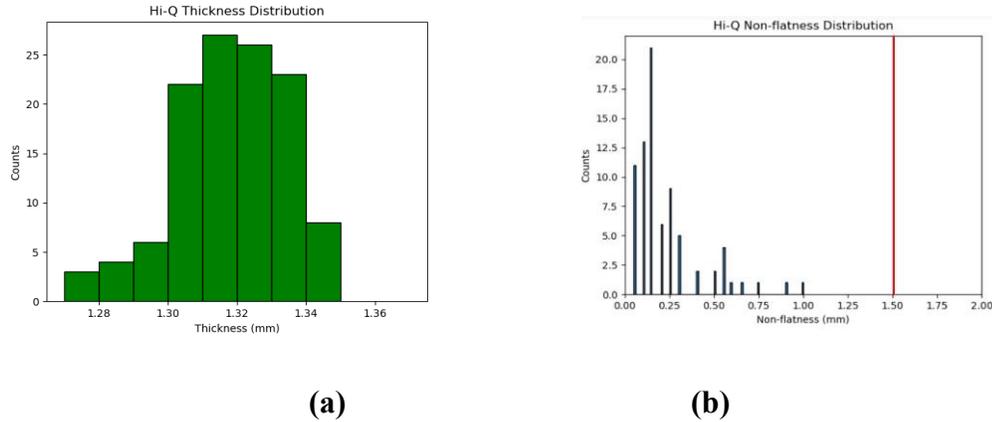
Figure 3.24: Thickness measurement results (a) and (b) non-flatness distribution of Hi-Q boards measured in millimeter.

HGCAL Si Sensor Testing Strategy

The CMS High Granularity Calorimeter follows a special quality assurance system (Hinger, 2021). This allows all sensors to be tested whether they meet predefined quality standards. Sensors are integrated into the CMS High Granularity Calorimeter according to this testing strategy. There are 4 steps of batch-based qualification for sensors as shown in Figure 3.25. According to this strategy, first all sensors are tested by the manufacturer, Hamamatsu Photonics K.K. (HPK) in Japan. Vendor Quality Control (VQC), provided by Hamamatsu, transmits sensors of which it is 100% sure to the distribution center at CERN, as well as all corresponding test structures.

Depending on the thickness of the sensors, there are two types of layout, low-density (LD) and high-density (HD), which define the number of cells. Hamamatsu produces them in thicknesses of 300 μm and 200 μm in the flotation zone process (FZ), while in the epitaxial process (epi) they are only 120 μm thick (Brondolin, 2020). This studied only low-density full and partial sensors.

All sensors and corresponding test structures are then transmitted from the distribution center at CERN to the relevant test centers for testing. These test centers are scientific institutions that can provide the necessary equipment and infrastructure. This

enables them to carry out quality control test procedures. Test structures undergo Process Quality Control (PQC), while sensors are subject to Sensor Quality Control (SQC).
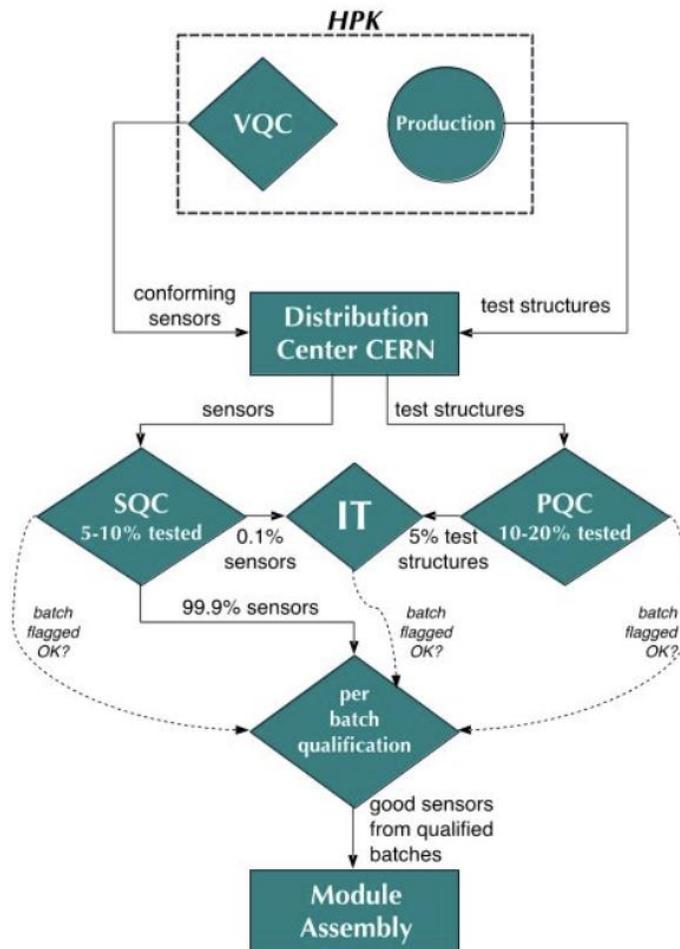
Figure 3.25: CMS High Granularity Calorimeter (HGCAL) silicon sensor testing strategy

The Institutes involved in the HGCAL Project at SQC are:

1. CERN

2. Florida State University (FSU)

3. Texas Tech University (TTU)

4. National Central University (NCU)

5. The Institute of High Energy Physics (IHEP)

6. The Institutes involved in the HGCAL Project at PQC are:

7. Florida State University (FSU)

8. The Institute of High Energy Physics (HEPHY)
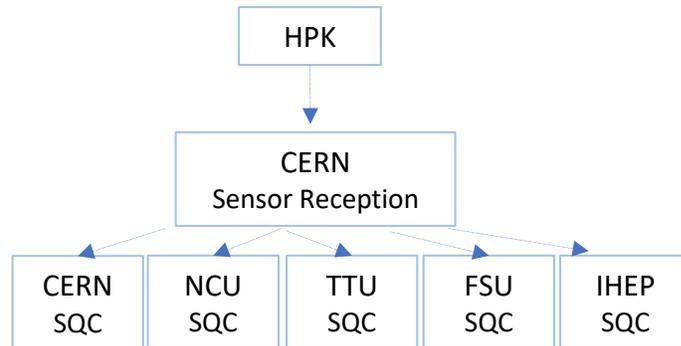
Figure 3.26: Sensor Quality Control (SQC) tracking diagram.

Sensor Quality Control

Sensor quality control for sensors is initiated at all SQC Institutes as shown in the Figure 3.26. Sensors are characterized through electrical and optical tests to provide information on the technical characteristics of the sensor. Full-wafer IV+CV measurements are available at all SQC institutes equipped with installations such as ARRAY system. Figure 3.27 shows an example setup at CERN. The ARRAY system enables fast electrical qualification of silicon sensors (Sicking et al., 2019). The SQC institutes test 10% of the pre-production sensors and 5% of the production sensors.

Process Quality Control

The hexagonal sensor is diced from the circular wafer as shown in the Figure 3.28. But remaining pieces are not wasted. These are called 'halfmoons'. Each halfmoon contains several test structures, such as single diodes, which have the same structure as a cell in the full sensor (Hinger, 2021).
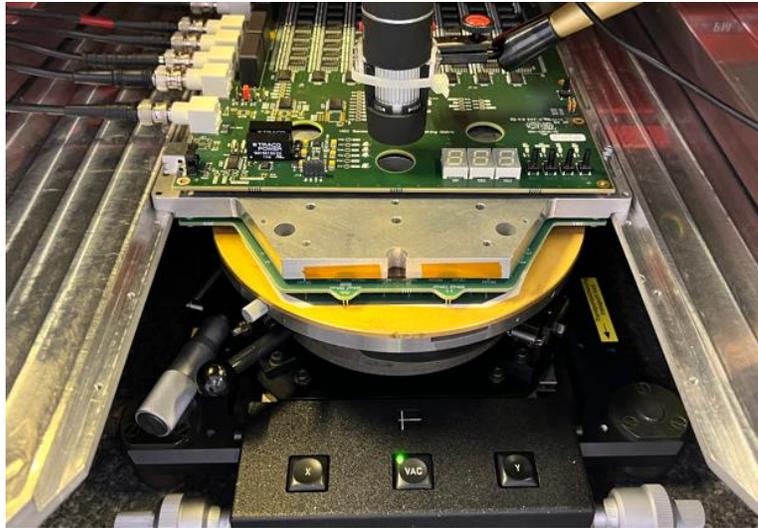
Figure 3.27: SQC probe station (PM8) at CERN
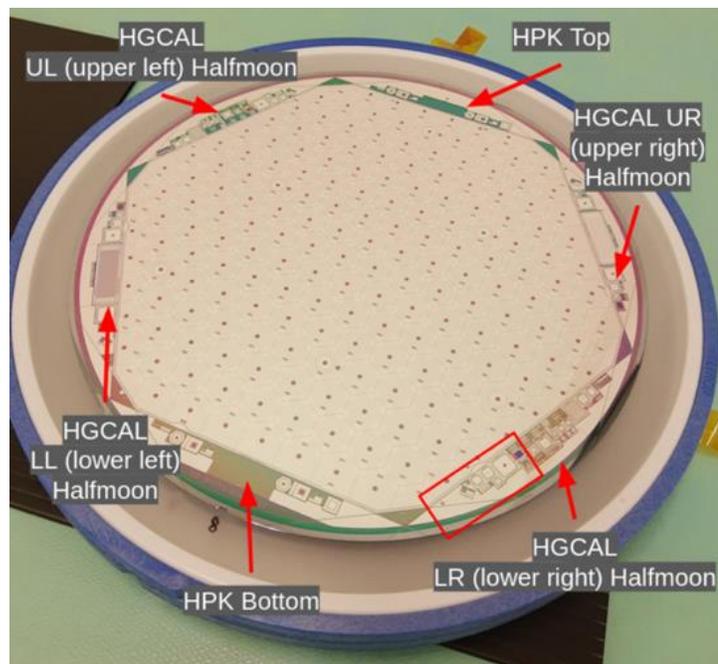
Figure 3.28: Full wafer silicon sensor.

Figure 3.29 shows the test structure diode used in the HGCAL. These test structures undergo Process Quality Control, i.e. PQC. This allows the quality and

consistency of the sensor manufacturing process to be monitored and measured easily due to their small size compared to full sensors. The PQC institutes test approximately 20% of the structures.
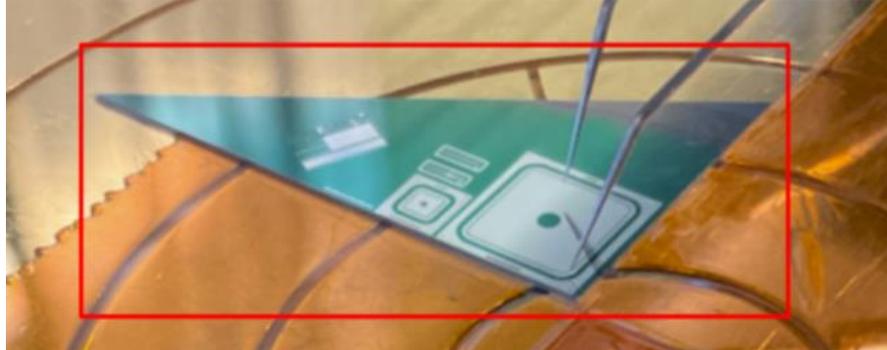
Figure 3.29: The test structure diode is shown, which is tested using two needles, one on the pad and the other on the guard ring.

After the SQC and PQC tests, 0.1% of the sensors and 5% of the test structures are collected for Irradiation Testing (IT). According to the HGCAL silicon sensor test strategy, if all these steps are completed well, firstly the sensors are sent to qualification per batch and then the good sensors from the qualified batches are sent to module assembly.

Data Collection Tools/Materials

In order to perform electrical characterization of silicon sensors we have an ARRAY sensor testing system. Using this system, we are measuring current-voltage (IV) and capacitance-voltage (CV) values of the pre-irradiation silicon sensors.

HGCAL will use approximately 26,000 sensors, corresponding to 6 million channels, to cover an area of approximately 620 m^2. For the quality control of silicon sensors, the sensors need to be electrically characterized quickly and automatically. For this reason, the ARRAY (switching mAtRix pRobe cArd sYstem) system for silicon

sensor testing has been developed at CERN (Sicking et al., 2019). The ARRAY system consists of an active switch card and a passive probe card.

The switch card consists of a 512 by 1 switching matrix. The probe card is a passive card that provides contact with the sensor. We bias the whole detector at the same time. But we read the signal from one cell at a time, so the switching card switches between cells. For this reason we need a switch card. So with this system the cells are tested separately for Current and Capacitance Voltage (IV+CV) measurements. The switch board is designed as a pluggable printed circuit board (PCB) and is placed directly on top of the probe board. The top (a) and bottom (b) view of the ARRAY (mAtRix probe board system with switch) system, which includes the switch and probe board systems, is shown in Figure 3.30 (Sicking et al., 2019).

(a)   **(b)**
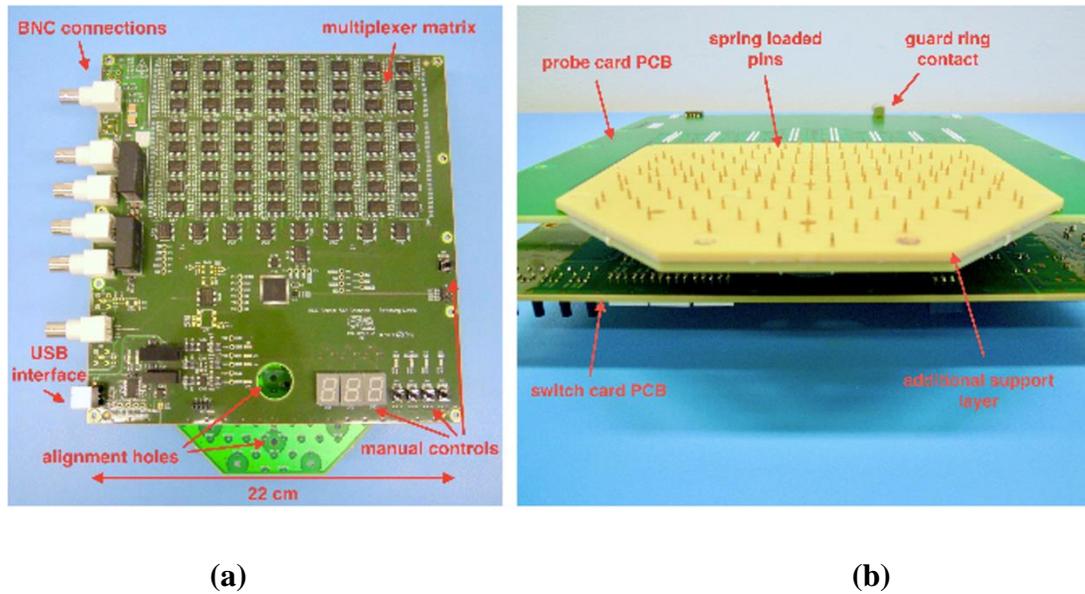
Figure 3.30: Of the two merged cards, the top is (a) the switch card and the bottom (b) the probe card.

The switch board, which consists of a series of multiplexers, controls the measurement. The probe board is a passive device consisting of a series of spring-loaded pins with a 1.4 mm range of movement, allowing it to simultaneously contact all pads on the sensor. The two boards are mechanically connected to a light-proof probe station

(PM8) inside a dark box, which prevents the formation of dark currents in the silicon sensors. The silicon sensors are held in place by vacuum on a chuck. Figure 3.31 shows all relevant components inside the probe station (PM8).
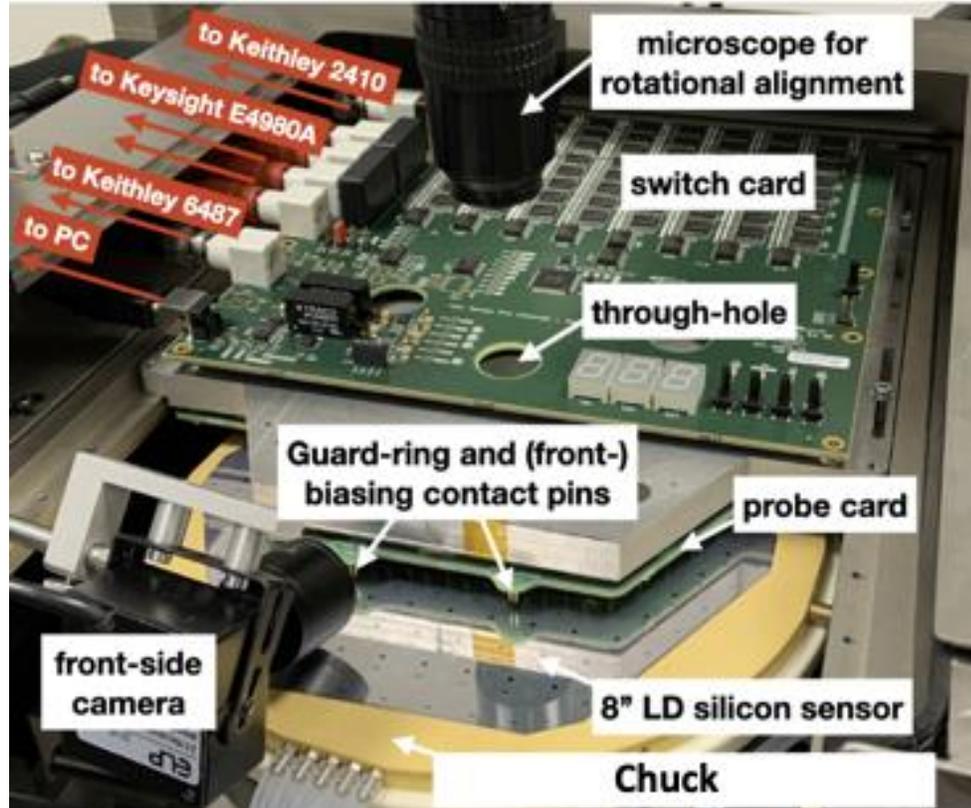
Figure 3.31: PM8 station at CERN.

In order to align the pins of the probe board to the pads on the sensor and thus ensure that all pins make contact, the USB microscope camera is used to view the holes in the boards and to assist in the X & Y alignment with respect to the sensor. A force of approximately 25 g per pin is applied to the probe station by mechanical integration. This ensures that the pins, which have a rounded tip with a radius of 250 μm, make good electrical contact with the aluminum pads on the sensor.

The probe card allows monitoring of the environment by integrating temperature and humidity sensors. Test capacitances have also been added to the probe board. This allows system calibration and cross-checking. All boards are based on the same concept.

Four probe cards are used for low-density and high-density sensors with different sensor geometries, i.e. full and partials. A simplified circuit diagram of the whole system is shown in Figure 3.32 (Sicking et al., 2019).
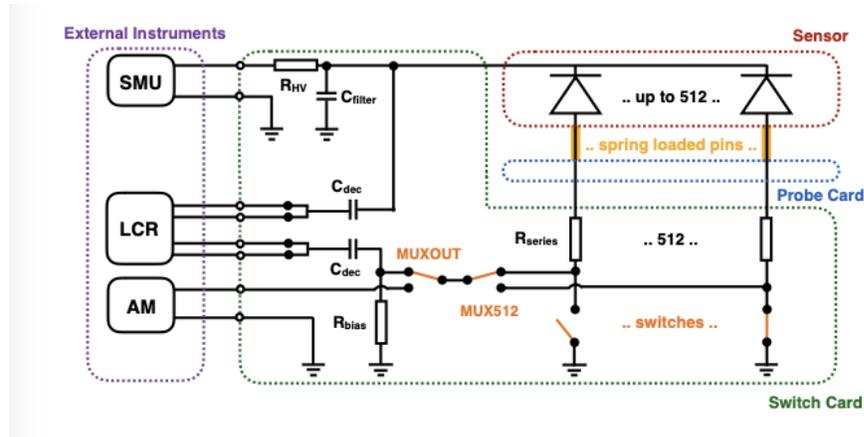
Figure 3.32: Simplified circuit diagram of the ARRAY system designed for 512 channels (Sicking et al., 2019).

(a)   (b)
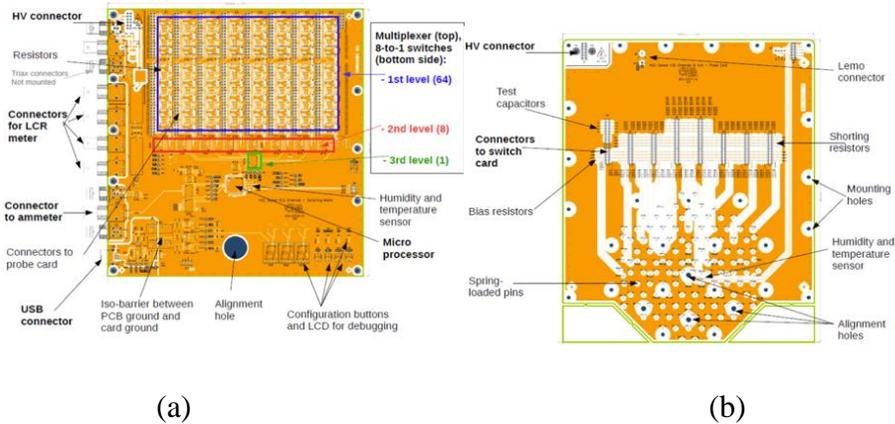
Figure 3.33: Switching matrix (a) and probe card (b) used testing silicon sensors.

By connecting a 10 kΩ resistors in series to the pins inside the switch card, high electrical currents that may occur during measurement are protected. The process of transmitting the signal from the pins on the probe card to the readout devices is provided by a 512-channel multiplexer (MUX512), while switching between the leakage current and capacitance measurement circuits is provided by the output multiplexer MUXOUT.

The switch board contains six coaxial BNC connections for connecting coaxial cables. This allows connection to external devices. There are 3 external devices, these are:

1. Keithley 2410 with power supply: Shown in Figure 3.32 with SMU (Source Measure Unit) provides the high voltage.
2. Keysight E4980A, used to measure the inductance (L), capacitance (C) and resistance (R): Shown in Figure 3.32 with LCR.
3. A picometer, Keithley 6487, used to measure extremely low levels of electric current: Shown as AM in Figure 3.32.

The other items shown in Figure 3.32 are auxiliary components that are particularly relevant for capacitance measurement. A resistor (R_{bias}) is used in the capacitance measurement so that the channel under test is not grounded. In the case of a voltage circuit, a high value resistor R_{bias} is added to ground. This can be set to eight different values between 100 kΩ and 100 MΩ. The resistor (R_{bias}) thus increases the impedance in the parallel circuit and allows the capacitance of a single pad to be measured instead of all the pads on the sensor.

A simplified circuit diagram of the ARRAY system shows two capacitors labelled C_{dec} with a capacitance of 1 microfarad (μF) (Sicking et al., 2019). These capacitors are used to separate or isolate the LCR meter from direct current (DC) voltage. In short, these two C_{dec} are decoupling capacitors, thus protecting the LCR meter from the bias voltage. The current flowing through the high voltage resistor (RHV) is defined as the total leakage current of the full silicon sensor, interpreted as dark current. The switch board is connected to the high voltage source/power supply (Keithley 2410) as shown in Figure 3.31. The high voltage can then be routed to the probe board via the RHV and C_{filter} filter network as shown in Figure 3.32 and applied to the backside of the sensor via the chuck.

Data Collection Procedures

To avoid sensor discharges, we prepare the PM8 probe station and sensor at the beginning of the measurements. There are three important steps: Optical inspection, Ion blower and Probe station preparation.

Optical Inspection:

Inspection is performed with the help of an artificial intelligence-supported microscope. The microscope is used to identify the sensor on the scratch pad IDs under the sensor (or next to it, depending on the sensor geometry) as shown in the Figure 3.34 (a). Then, using a bulb blower or clean room cloths, remove dust and dirt from the sensor. Particular attention should be paid to the ground ring and high voltage rings surrounding the sensor to minimize the possibility of sensor discharge. This is because ground (0V) and HV (up to 1000V) are close to each other. If there are any scratches on the sensor, they are entered into the elog, which we report regularly. Thus, if any non-contact or abnormal condition is detected on the pads with scratches after the measurement, a conclusion can be drawn by comparing with the previous elog. A photo of the sensor in the clean room at CERN during the pre-measurement optical inspection is shown in Figure 3.34 (b) (Sicking, 2023).

(a)   (b)
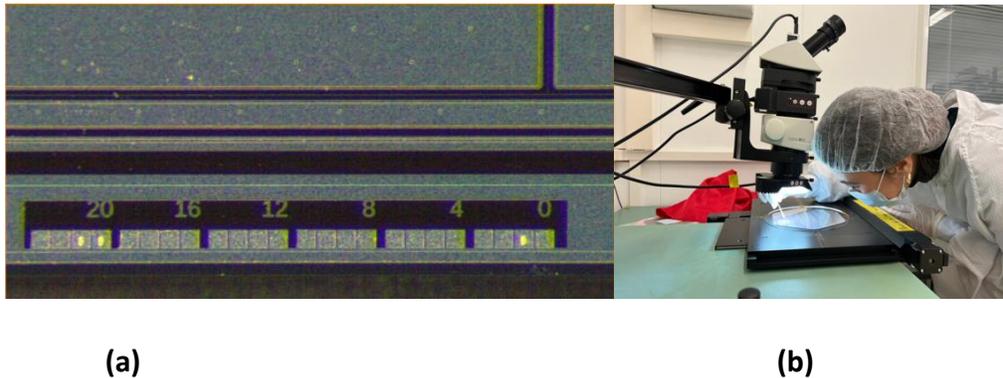
Figure 3.34: (a) Scratch pad for sensor ID. (b) Pre-measurement optical inspection of the sensor in the clean room at CERN (Sicking, 2023).

Ion Blower:

Ionized Air Blower is applied to the sensor to remove the surface charge on the silicon sensor. This eliminates potential charge on the sensor that could lead to high leakage currents and discharges during measurement. Before measurement, the sensor is placed under the Ionizing Air Blower for approximately 5 minutes as in Figure 3.35.

Preparing the probe station:

One person holds the sensor in front of the chuck while the second person uses the vacuum tweezers to place the sensor on the probe station, which we call PM8. And alignment is done by checking through a USB microscope through the central hole in the probe board. With the help of a label as shown in the Figure 3.36, the circular contact area of the sensor must follow the same label along a circular y-axis, which is a Mercedes cross-like intersection of three hexagons. This ensures alignment.
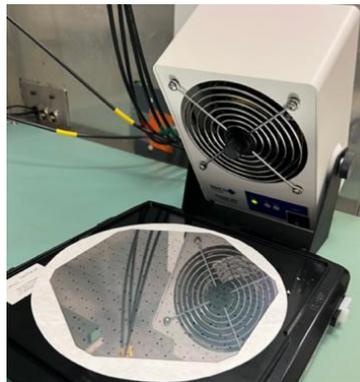
Figure 3.35: Photograph of the sensor placed below the Ionizing Air Blower (Sicking, 2023).
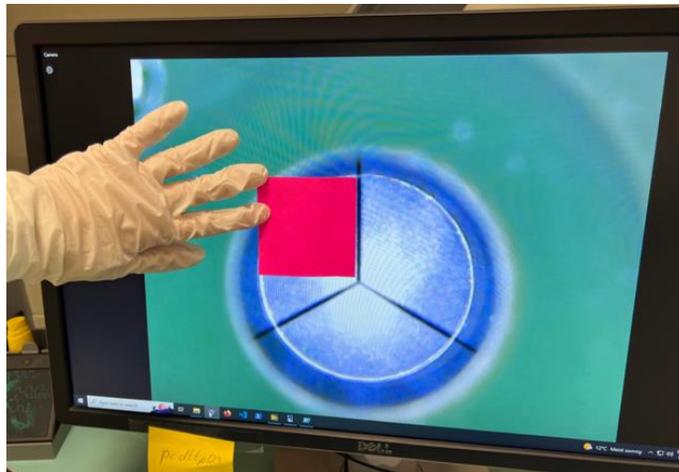
Figure 3.36: Image of a circle with the circular contact area of the sensor, a Mercedes cross-like intersection of three hexagons. The alignment of the sensor is aligned with the pink label used at the intersection point (Sicking, 2023).

IV/CV measurements are performed automatically by HexDAQ based on LabVIEW. Before the IVCV measurement, however, the "Test_Contact" measurement (= IV @ 1V forward bias) is performed to test whether all pins in contact with the probe card are in contact with the sensor. In this measurement all cells should show a forward bias current between 10nA and 100nA. After making sure that all pins are in contact, the IV+CV measurement is started.

The IVCV measurement takes less than 2 hours and "Measured every nth pad = every 10" can be selected to speed up the measurement. With this setting, during IV+CV scans, all cells are measured as IV and every 10th cell is measured as CV. With this fast scanning, two sensors can be measured in one shift and the results can be quickly evaluated. During this measurement, sensors are normally expected to have cells with cell currents in the order of a few nano amperes. However, the protection ring usually has higher currents than standard cells. These cell numbers are 198 for Low-Density sensors and 444 for High-Density sensors.

Data Acquisition (DAQ): LabView

The switch board is controlled via an on-board microprocessor and USB interface. IV/CV (leakage current voltage/capacitance voltage) measurements of silicon sensors are performed automatically by a LabVIEW-based data acquisition system (HexDAQ version 1.8.1). The LabVIEW program is interfaced with HexPlot. This allows the recorded data to be displayed in geometric shapes. IVCV measurement requires no user intervention. Voltage scans automatically terminate when total leakage current reaches a configurable compliance level. This compliance level is usually around 1mA (Quast, 2020). Similarly, individual pads with leakage currents exceeding 5 µA are no longer measured. Compliance limit prevent large voltage drops in the test circuit, minimizing the risk of damage to the ARRAY system. [Current limits: Compliance level: 1 mA, pad masking level: 5 µA]

The leakage current is measured as a function of the bias voltage (IV measurement), which varies in 100V steps (except for the first and last steps: first and last step 50 V) from –25 V to –850 V. Capacitance is also measured as a function of bias

voltage (CV measurement), similar to IV. However, the voltage list change according to the sensor thickness:

1. Between –5V and –400V for 300 µm sensors
2. Between –5V and –200V for 200 µm sensors
3. Between –5V and –100V for 120 µm sensors is measured as a function of changing bias voltage.

Data Analysis Plan

There is a code structure for IVCV analysis of sensors (Quast et al. 2024). These are:

1. A python code called 'CSV_entry_generator' which creates a database to analyze the Hamamatsu data.
2. The IVCV analysis code, which consists of several python code components and performs the analysis of both Hamamatsu and CMS data. In this code, I worked on some of the python code components responsible for the IV analysis. As a result of improvement and debugging:

It was discovered that the Hamamatsu data, which previously failed due to incorrect calculation of the bias voltage, should pass the correct analysis. Improvements were made to the IV rating output:

1. For one of the acceptance criteria, high current increase.
2. The ratio between the currents of the measured sensors at 600 V and 800 V is added. This gives us the information how much smaller or how much bigger the factor is than 2.5.
3. Added the total current values of the measured sensor at 600V and 800V.

After the IVCV analysis code, there is a python code called 'Grading csv generator' which generates a summary of the grading for both HPK and CMS data.

'HexaBatch', a python code that analyzes both CMS and HPK data and presents it in a few minutes. I've upgraded python for efficient analysis and visualization of large sensor data, such as about 1000 sensors produced by HPK in Japan. Especially during the production phase, Hamamatsu sends thousands sensors every month to sensor quality institutes. HPK, the manufacturer, tests all the sensors and transmits both the sensors and the data. Some of the sensors are then tested at the SQC institutes. In order to compare with CMS measurements, it is necessary to obtain all the results of the data sent by HPK. Therefore, a code is needed that is fast and contains all the information. The HexaBatch code allowed us to get the results faster. It plots the output data from the IVCV analysis code and presents the results in a nice format and generates an automatic PDF presentation as a summary of the delivery in a few minutes. The output is stored under the name 'IV_CV.pdf'. The IV_CV.pdf automatic presentation file is renamed according to delivery date.

CHAPTER IV

Findings and Discussion

Global Characterization of the full sensor

Randomly selected samples from each batch of 8" silicon sensors received by HPK (a single batch contains approximately 25 sensors) are electrically characterized. This is performed by measuring the leakage current (IV) and capacitance (CV) of the sensor.

In order to perform the electrical characterization of the silicon sensors, the current values of each channel are measured for different voltage values. After the IV measurements and the capacitance is calculated and CV values are deduced as well. The collected results are stored for processing and analysis which is done using a Python code. These acceptance criteria provide information about the specified requirements of the sensor. There are different acceptance criteria for non-irradiated sensors with IV+CV measurements. Sensor parameters and specifications for CMS HGCAL are given in Table 4.1 (Hinger, 2021).

IVCV Analysis

As described in Chapter 2, a depletion zone is created in p-n junction silicon sensors in order to reduce leakage current, which is background signal for the detector. This zone behaves like a capacitor. The electrical characterization of the silicon sensors therefore depends on the measurement of current and voltage (IV measurement) and the capacitor-voltage measurement (called CV measurement). When designing a silicon detector, certain criteria are set. IV and CV values are determined according to the size of the sensor wafer, the dimensions of the cells and the signal background ratio. Our task at CERN is to measure each cell of the silicon sensors and to find out whether or not those criteria are met.

Table 4.1.

Acceptance Limits and Sensor Qualification Requirements for Silicon Sensors to Be Used in CMS HGCAL

Parameter	CMS specification
Substrate resistivity, ρ	$> 3.0\ k\Omega\ cm$
Physical thickness, t_p	$300\ \mu m, 200\ \mu m, 300 \mu m$
Active thickness, t_a	$300\ \mu m, 200\ \mu m, 120 \mu m$
Thickness tolerance	$< \mp 10\ \mu m$
Full depletion voltage, V_{dp}	$300\ \mu m$ type: $<\ 370\ V$
	$200\ \mu m$ type: $<\ 160\ V$
	$120\ \mu m$ type: $<\ 70\ V$
Current at 600 V (normalized to 20°C), I_{600}	$\leq 100\ \mu A$ integrated over sensor and guard rings
Current at 800 V, I_{800}	$<\ 2.5\ \times I_{600}$
Breakdown voltage, V_{dp}	$>\ 800\ V$
Long-term stability	$|\langle \Delta I_{600}/I_{600}\rangle| < 30\%$ in 48 h at 600V and $< 30\%\ rH$
Single-cell current at 600 V, I_{pad}	$\leq 100\ nA/pad$
Inter-cell resistance, R_{int}	$> 100\ M\Omega$ at $V_{fd} + 50$ V and room temperature
Inter-cell capacitance, C_{int}	$< 1.5\ pF/cm$ at $V_{fd} + 50$ V and room temperature
Number of bad cells	≤ 8 per full-size sensor
Clustering of bad cells	≤ 2 adjacent bad cells

Leakage Current (IV) Acceptance Criteria

IV method involves measuring the current that flows through the sensor at specific bias-voltages. By that way one can determine the sensor's insulating properties and

identify any undesired leakage paths. Sensor is accepted if the leakage current measurements are below specific criteria. Otherwise, if the sensor fails, it cannot be accepted. There are three important acceptance criteria about the pass/fail of the sensor (Quast et al. 2024).

1. Total current for all cells (including guard ring) should be below 100 µA at 600 V.
2. Total current (sum of the currents of all channels) should be not more than 2.5 factor increase between 600 V and 800 V.
3. There cannot be more than 8 high current pads or 2 neighboring pads with high current.

We contributed to a change in the rating output of IV. A new line has been added regarding the total current increases. This makes it easy to find out from the IV grading output how much less than 2.5 or how much more than 2.5 the ratio between the currents at 600 and 800 V is. The IV grading result for an example sensor that fulfils all acceptance criteria is shown in the Figure 4.1.

Info:
  - Last measured voltage point: 850.0 V;
  - Expected depletion voltage for sensors of thickness 300 μm: 250 V; 250 x 1.5 = 375.0 V.
  - IV scan performed well above 1.5 times the expected depletion voltage.

Grading:
  - Sensor has been graded with checksCollectionID 1.
  - Global characteristics:
    - Current at 600V I600 (normalised to 20 deg Celsius): <= 100 μA integrated over the sensor and guard rings: Passed
    - I800 < 2.5 x I600: Passed
    - I600 = 0.176 uA I800 = 0.268 uA factor: 1.52
    - Number of bad pads 0 <= 8 for full-sized sensors: Passed
    - Allowed number of adjacent bad pads <= 2: Passed
  - Per-pad characteristics used to define bad pads if any of the following are met:
    - Current at 600V I600 (normalised to 20 deg Celsius) > 100 nA/pad: 0 pads, namely []
    - I600 > 10 nA and I800 > 2.5 x I600: 0 pads, namely []
    - I600 ≤ 10 nA and I800 > 25 nA: 0 pads, namely []

Sensor has PASSED the requirements.
WARNING: The following pads were masked at least once before or at 600V: [].

Figure 4.1: IV grading output of sensor number 105793 delivered by HPK to CERN in September 2023. This sensor has a thickness of 300 µm and was measured at CERN (Quast et al. 2024).

The results of the sensors analyzed with the python code are presented to us in a pdf format in several ways. Summary graphs, called hexplots, are then generated for each different bias voltage. Cells with high leakage current can be easily detected with the help of the visualised hexplot. There are many Python code components in the IV workflow (Quast et al. 2024). The equation 1.1 below is used for temperature scaling:

$$I_{ref} = I_T \cdot \left(\frac{T_{ref}}{T}\right)^2 \cdot exp\left(\frac{E_g}{2.k_b} \cdot \left(\frac{1}{T} - \frac{1}{T_{ref}}\right)\right) \qquad (4.1)$$

There is an acceptance grading criterion for all cells (including guard ring) where the total current must be below 100 µA at 600 V at 20 degrees. For this reason, in the python code that performs the analysis, I detected and corrected the problems by debugging for a more accurate analysis. As a result, the reference temperature (T_{ref}) was changed from –20 to +20 degrees and T_{ref} was set to 20 degrees. The hexplots of two sensors measured at 600 V bias voltage at CERN are shown in Figure 4.2.
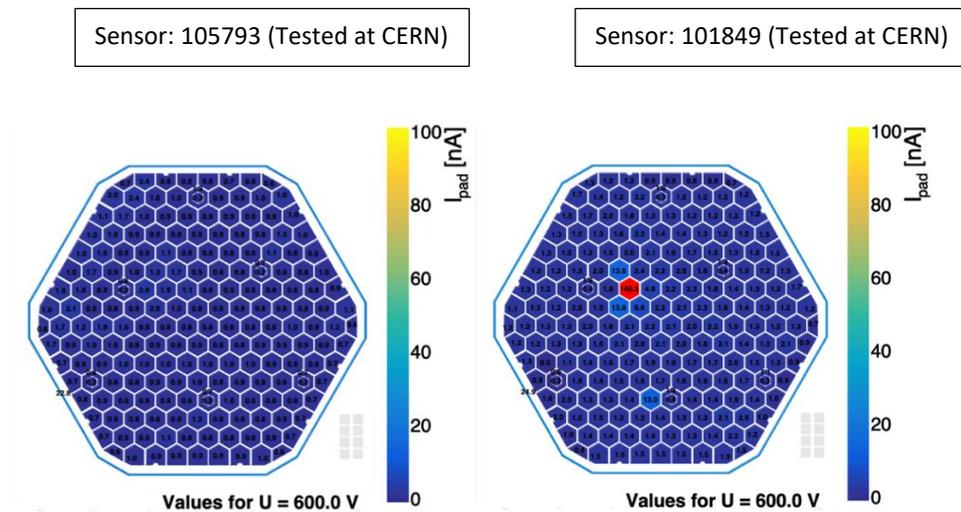
Figure 4.2: Example hexplots of the leakage current values recorded at 600 V bias voltage for two different sensors measured at CERN (Quast et al. 2024).

Per-pad characteristics are used to identify bad pads and which channel has the higher current. This info is included in the IV grading output. As shown in the hexplot on the right in Figure 4.2, sensor 101849 has one channel with high current. This channel has a current greater than 100 nA. Plots that help to observe how the leakage current varies with the bias voltage are also included in the pdf of the IV analysis results.

As shown in the left plot in Figure 4.3, channel 72 is above the threshold value at 600 V. The threshold value of 100 nA is indicated by the red dashed line. Since there are no 8 or more than 8 high current pads in this sensor, the sensor is passed. The plot on the right also shows that the increase in total current between 600 V and 800 V is below the 100 µA limit. With the modifications I have made to the python code that performs the IVCV analysis, the total current values at 600 and 800 V and the total current factor between them can be observed at the rating output of the measurement.
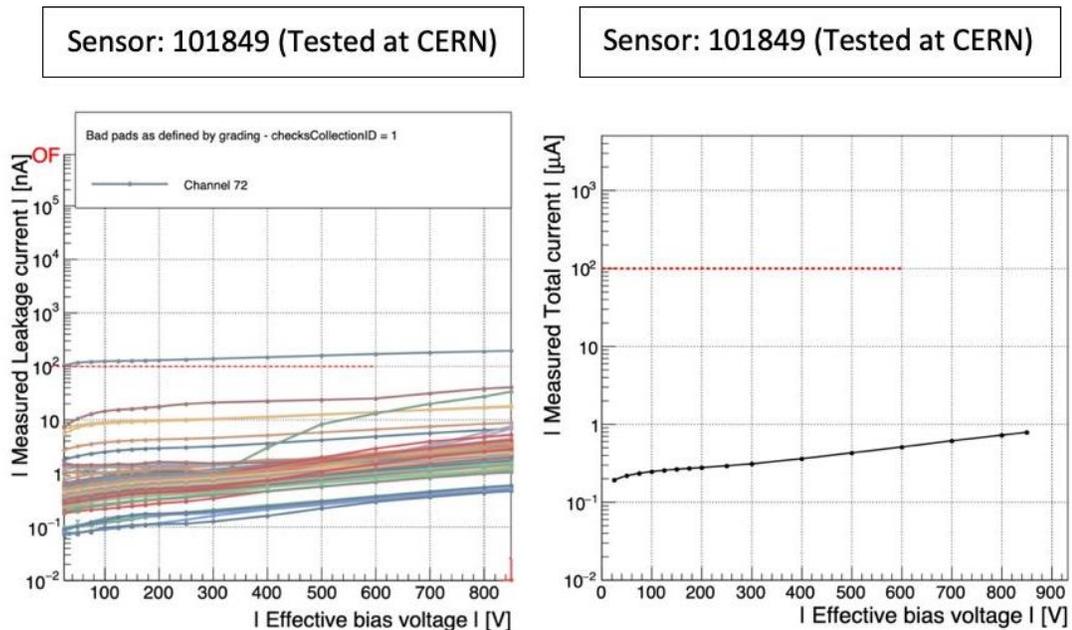
Figure 4.3: The IV curves for all channels of sensor 101849 (left) and the total current curve (right) for the same sensor (Quast et al. 2024).

Each sensor is measured and analyzed according to defined acceptance criteria and as previously described. However, there are differences between the measurements of the manufacturer Hamamatsu and CMS, which includes the SQC institutes. HPK carries out tests for all types of silicon sensor before the dicing frame. CMS institutes perform measurements and analyses after the dicing frame. This affects guard ring performance.

Hamamatsu has delivered 11,515 production sensors with 3 active thicknesses to SQC institutes from 2023 to March 2024. CERN received 2703 of them. Until April 2024, 184 sensors were tested at CERN. A few (around 7) of the tested sensors failed for the same reason: They failed because they did not fulfil one of the same acceptance criteria, which is the total current increase. The common reason for the failed sensors the total current increase was studied more closely.

This close study examines sensors that pass in the second measurement. The second measurement is performed if one of the channels affecting the total current rise is a guard ring. As shown in Figure 4.4 from the leakage and total current plots, the total current of the low-density sensor 109248 with a thickness of 300 μm is driven by the Guard Ring and the sensor failed. According to the IV results, the total current increased more than 2.5 times between 600 and 800V. On the other hand, we observed that the sensor has a low cell current.
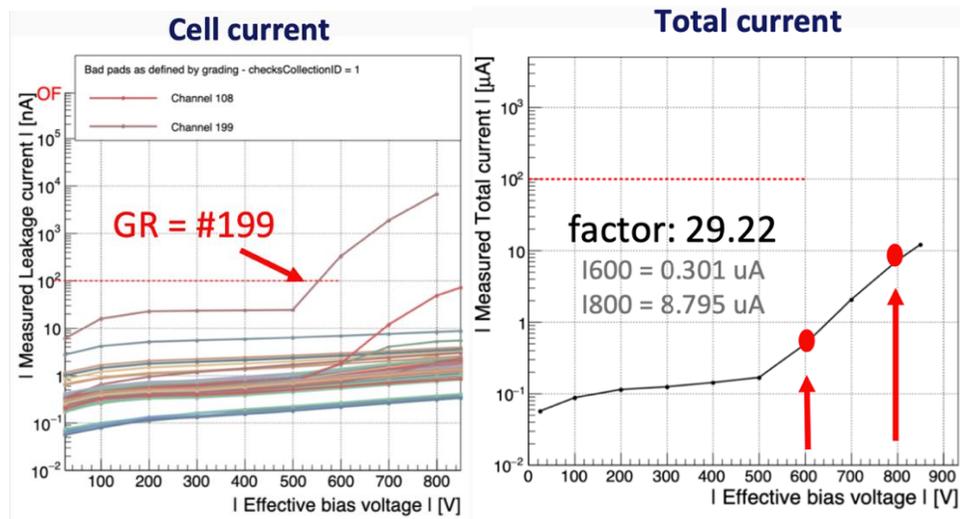
Figure 4.4: The cell and total current plots of **the first IV measurement** result of the low-density production 109248 sensor are shown. This sensor is **failed** (Quast et al. 2024).

The same sensor was measured a second time. The preferred method for the second measurement is to start the measurement analysis again from LabVIEW without removing it from the measurement station (PM8). This way, faster results are obtained and time loss is prevented. The sensor was successful in the second measurement. In the second measurement, channel 199 (guard ring) is below 100nA, as shown in the IV plots in Figure 4.5.
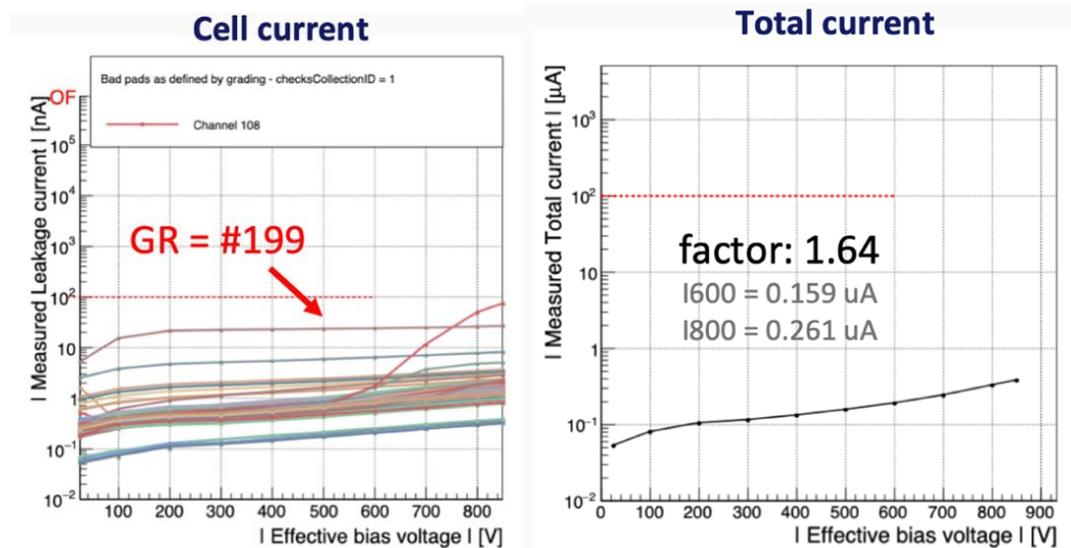
Figure 4.5: The cell and total current plots of **the second IV measurement** result of the low-density production sensor 109248 are shown. This sensor is **passed** (Quast et al. 2024).

But in the first measurement the same channel is above the threshold. The one cell (guard ring) has an effect on whether the sensor passes or not. We have observed this kind of results in many sensors at CERN, where the measurement of the total current is driven by the guard ring.

These results were shared with other SQC institutes and a common conclusion was reached. The sensors with the same observations were compared. Thus, a table containing the results of the first and second sensor measurements is created. Table 4.2 shows the results of the production sensors, including some of them (4), which were measured at

CERN and TTU. In the first measurement, the sensors are failed, while in the second measurement, the sensors are passed. The sensors are all low-density and have a thickness of 300 µm. In the second measurement the 300 µm LD sensors passed.

The Table 4.2 shows how much total current increase the sensors had between 600 and 800 V in the first and second measurement and the total current values at these voltages. The table also shows which cell exceeded the acceptance threshold of 100 µA. According to this information, it was observed that the total current values of all sensors except two sensors were below 10 µA at 800 V.

Table 4.2.

First and Second Measurement Results of 4 Production Sensors Measured at the SQC Institutes CERN and TTU

Sensor	Location CMS	I_tot_600V [µA] (at 20°C)	I_tot_800V [µA] (at 20°C)	Total current increase between 600V & 800V	Grading	Cell driving the current increase
105732 [1 st]	CERN	0.136	8.883	65.38	Failed	189,199=GR
105732 [2 nd]	CERN	0.121	0.281	2.31	Passed	-
102263 [1 st]	TTU	1.757	11.244	6.40	Failed	193,199=GR
102263 [2 nd]	TTU	0.481	0.987	2.06	Passed	-
102363 [1 st]	TTU	0.48	13.632	28.40	Failed	199=GR
102363 [2 nd]	TTU	0.254	0.466	1.83	Passed	-
109248 [1 st]	CERN	0.301	8.795	29.22	Failed	199=GR
109248 [2 nd]	CERN	0.159	0.261	1.64	Passed	-

This resulted in a plot containing the measurement results of all the sensors that failed due to the total current increase. The plot in Figure 4.6 shows how much more than a factor of 2.5 the sensors had between 600 V and 800 V and how much current the sensors

had at 800 V. The plot shows that at 800 V, total currents of less than 2 µA have low factors, while total currents of more than 5 µA (mostly intermediate) have high factors.

Taking all this into account, a general interpretation was made. Based on the analysis and observation results, it was recommended that if the failed sensors have a total current of less than 10 µA at 800V, no second re-measurement should be performed. This reduces the re-measurement rate by half.
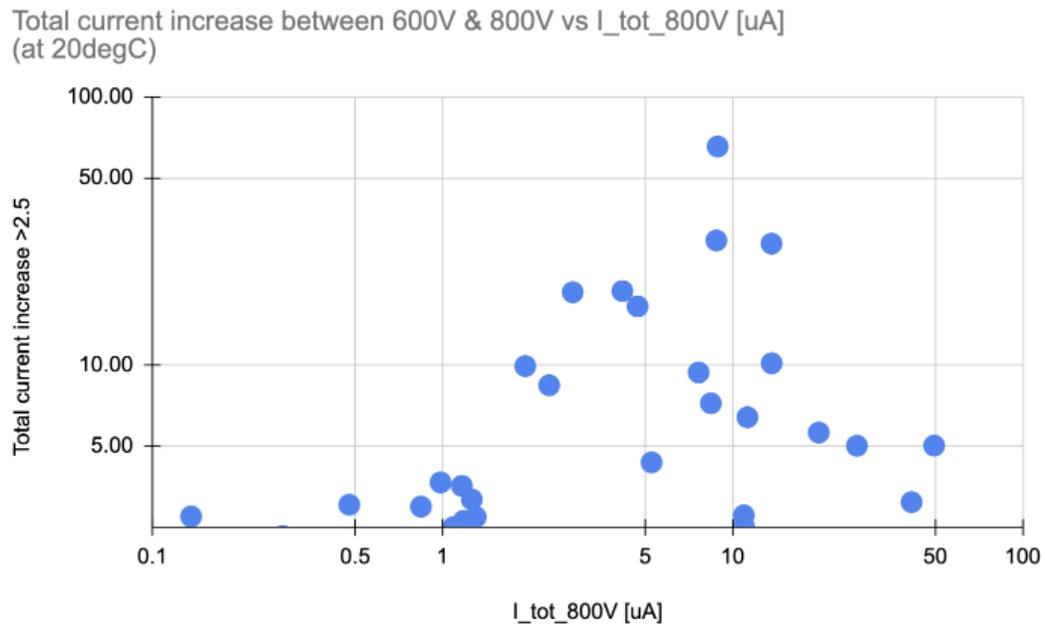
Figure 4.6: The total current of the sensor versus the total current of the sensor at 800 V.

One cell (guard ring) affects the measurement performance (Sicking et al., 2019). Hence, measurements are approached with precision. According to the technical specification for the procurement of silicon sensors for the CMS HGCAL upgrade project, the measurement condition is a relative humidity of less than 60%. The cleanroom laboratory at CERN sometimes has higher humidity levels. In case there may be a correlation between the discharges in the sensor and the relative humidity, the PM8 probe station is flushed with dry air at the beginning of the measurements. This reduces the humidity and prevents any possible discharges on the sensor. Humidity can be one of the reasons for the success of the second sensor measurement. If there is some residual

humidity on the sensor, the first measurement may be slightly heating the sensor, which may vaporize the humidity. However, given that the measurements at CERN are reliable, the measurements are approached with sensitivity as the one cell (guard ring) affects the measurement performance.

Capacitance (CV) Acceptance Criteria

Measuring the capacitance allows the charge storage capacity of the sensor to be understood. Therefore, CV measurements offer a valuable insight into how the sensor reacts across different voltage and frequency ranges. Capacitance measurements also have acceptance criteria like IV. When measuring for sensors with different thicknesses, in the LabVIEW program where the IVCV analysis takes place, the CV voltage list is changed according to the sensor thickness before the measurement.

Because there is a dependent limit for the depletion voltage. This limit is based on the thickness of the sensors, which are 120, 200 and 300 µm. The threshold voltage values for the depletion voltages per thickness are as follows.

1. For 300 µm sensor thickness, the threshold must be less than 370 V.
2. For 200 µm sensor thickness, the threshold should be less than 160 V.
3. For 120 µm sensor thickness, the threshold must be less than 70 V.

Also, among the acceptance criteria, the relative thickness variation must be less than 10 µm. According to these thresholds, the sensor either passes or fails. The results of the analysis after the measurement are included in a pdf format containing only the CV results as in IV. It is possible to present the results in several ways. With a graph showing the CV curves per cell for all pads, the capacitance values as a function of the applied bias voltage can be observed. For CV tests on 300 µm thick sensors, a bias voltage of up to 400 V is applied. This value is less for sensors with a thickness of 200, 120 µm. In Figure 4.7, sensor 108993 with a thickness of 300 µm shows these CV curves. The plot shows the capacitance values of the cells with different geometries. The capacitance value of full cells, which are standard cells (shown in red color in the plot), is around 44-45 pF.
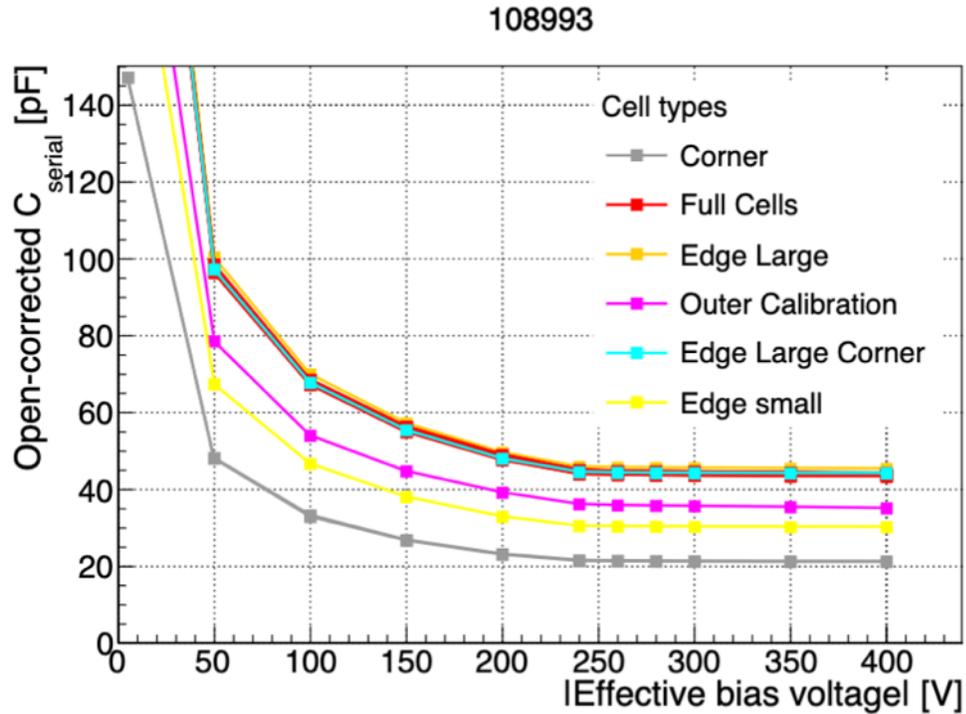
Figure 4.7: CV analysis plot of sensor 108993 measured at CERN. Effective bias voltage versus capacitance values for all channels with different geometries (Quast et al. 2024).

There are differences between CV measurements made at Hamamatsu CMS. HPK characterizes the capacitance of the sensor with a test diode on a half-moon. In other words, the manufacturer measures only one diode with the same structure as a cell in the full sensor. Figure 4.8 shows the location of the HPK monitoring diode on the wafer. CMS institutes perform capacitance measurement per pad after dicing.

CV measurements take longer than IVs. For this reason, it is sometimes possible to perform a CV measurement by including only a few selected cells (e.g. every 10th pad) to speed up the measurement.

(a)   (b)
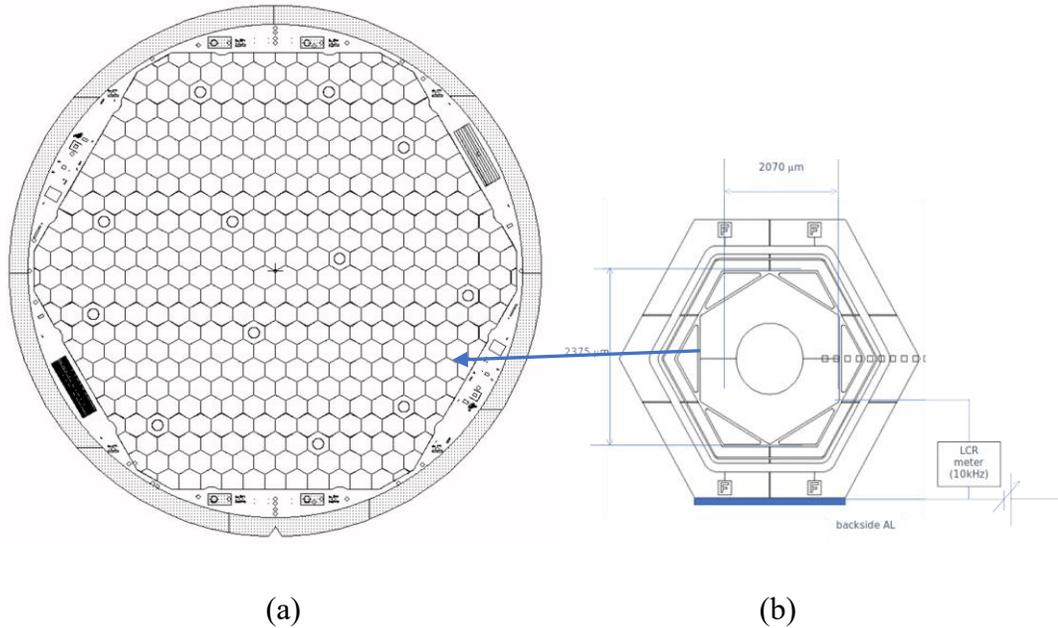
Figure 4.8: (a) Capacitance of monitoring diode. (b) Location of HPK monitoring diode on wafer.

Auto-presentation code

Multiple Geometry Wafers (MGW) IVCV Analysis Results

Partial sensors are required to provide sufficient coverage around the regions instrumented with silicon sensors. The cut types and geometries of sensors with different densities are shown in Figure 4.9. Multiple Geometry Wafers (MGW) have been produced to tile the inner and outer edges of the sensitive layers of HGCal cassettes (Azzi et al., 2017). Partial high-density sensors (HD MGW) are used on the inside of the HGCal cassettes where radiation exposure is high (high η), while partial low-density sensors (LD MGW) are used on the outside where radiation exposure is lower (low η). The channel map of the LD and HD multi-geometry wafers is shown in Figure 4.10.
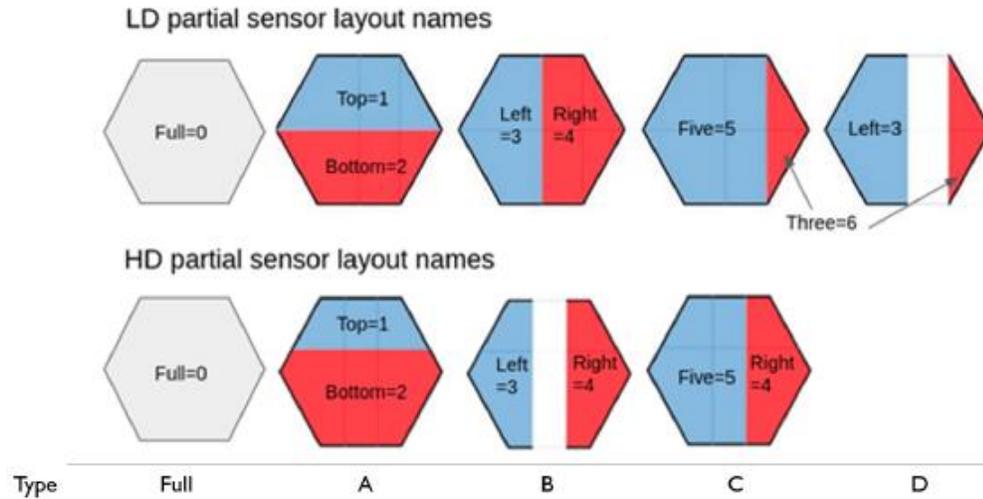
Figure 4.9: The cut types and geometries of high- and low-density sensors.
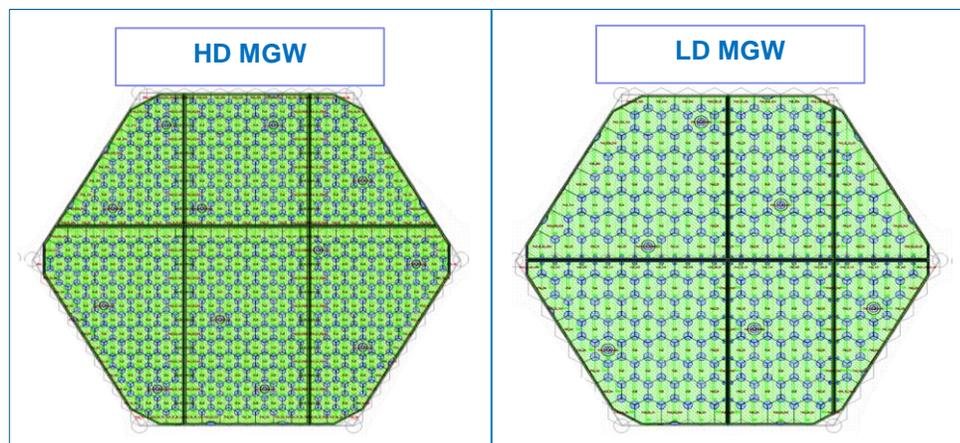
Figure 4.10: Channel map of a high-density multi-geometry wafer (HD-MGW) (Left). Channel map of a low-density multi-geometry wafer (LD-MGW) (Right).

For an accurate analysis, it is important to correctly determine the density, geometry and type of sensor. In Hamamatsu, the sensors are measured as full wafers, whereas in CMS they are measured after dicing. Therefore, HPK data is not separated by cut types, but CMS data is separated by cut types. Python code has been developed to analyze the partial sensors measured at Hamamatsu and CERN. A data frame is created

according to the type of cuts the sensors have. This way it is possible to analyze different types of cuts (e.g. right or left partial) of sensors in the same batch in a single code. A comparison of the IVCV analysis results of low-density multi-geometry wafers measured at HPK with CERN measurements is shown in Figure 4.11. Partial sensors, measured and analyzed at CERN, are pre-series and have a thickness of 300 µm. They have three different types of cuts, type b left and right and type c five.

The code that we contributed to the development of generates separate plots for leakage and capacitance measurements for the sensors being measured. Plots are produced according to IVCV acceptance criteria. The output of four different plots according to the IV acceptance criteria of the sensors is shown in Figure 4.11 (a). From the legend and the box plots it is easy to identify which cut type the sensor belongs to.

The first plot, the cell current plot, shows whether all cell currents of the sensors at 600 V are below the threshold. The mean values are also printed in the legend. First the median of each sensor is calculated and then the average of all sensors is taken. This gives the mean values. From the example result it is observed that there are no hot cells exceeding the 100 nA threshold for both HPK and CERN results.

The second plot is the protection ring current plot. The Y axis is the bias voltage applied to the sensor. All sensors are below 100nA at 600V and it means that the sensors meet the acceptance criteria.

The third plot is the total current for all sensors. The total current for all sensors is below the threshold of 100 µA.

The fourth plot represents the grading results. This plot shows the total number of sensors that passed or failed at CERN and HPK. The data is sorted in code according to the IV acceptance criteria as pass or fail and presented in a nice format.

IV plot is the results of 15 pre-series low-density partial sensors measured at CERN and all (19) multi-geometry wafers measured at HPK. All sensors have passed.

The code also provides the results of the analysis of all sensors according to the CV acceptance criteria. Figure 4.11 (b) presents the depletion voltage values of the pre-series

partial sensors. For sensors with 300 µm thickness, the depletion voltage of 370 V is shown by the red dashed line. The depletion voltage is below the threshold for all multi-geometry wafers measured at both CERN and HPK. The CV plot represents that the estimated depletion voltage for the partial sensors measured at CERN is around 280 V.
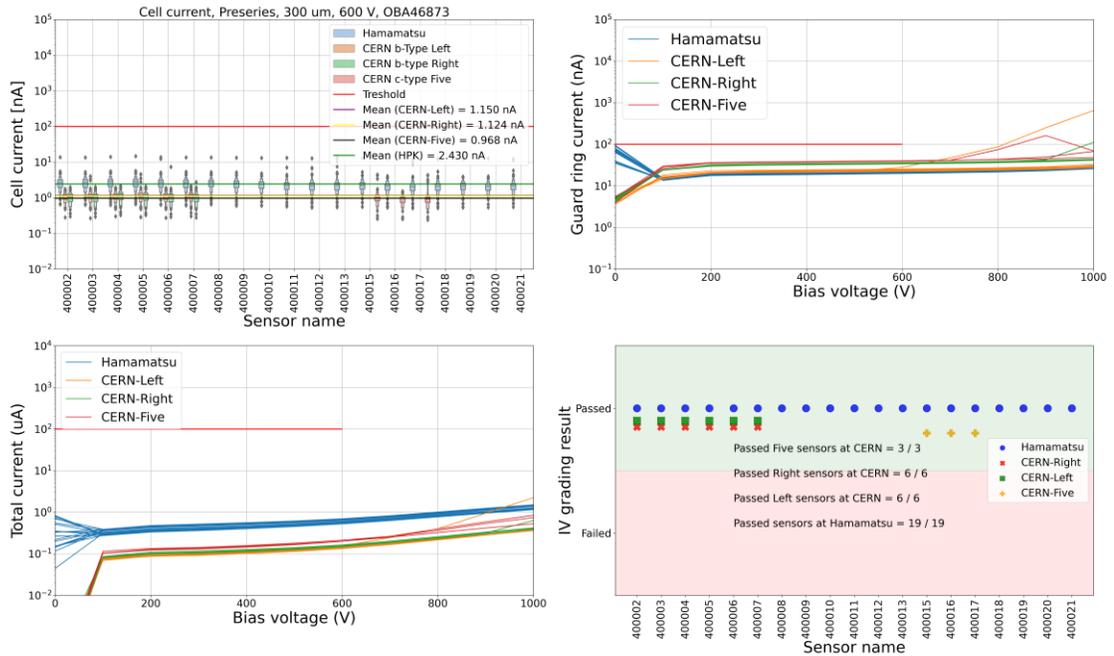
Figure 4.11: (a) Comparison of HPK and CERN IV measurement results of pre-series LD MGW.
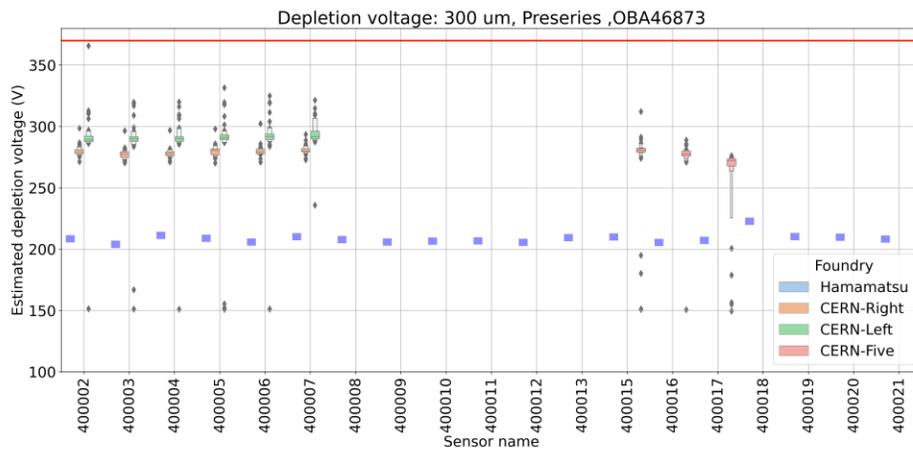
Figure 4.11: (b) Comparison of HPK and CERN CV measurement results of pre-series LD MGW.

Full Sensor IVCV Analysis Results with HexaBatch

With the HexaBatch code, which presents the IVCV analysis results in a nice format, you can access a lot of information about the delivery each month. The code calculates the number of batches and sensors for delivery as well as the number of failed sensors. This way, the first page contains information about the campaign, such as delivery date, number of batches, sensors, etc. The density of these sensors, the number of channels they are in, and whether they are irradiated or not can also be found on the first page of the auto-presentation code HexaBatch generates. For example; Figure 4.12 shows the first page with the HPK results of the code with the delivery information for September 2023 for the production phase. It reports the results of 1106 sensor deliveries in September, totaling 48 batches. It can also be determined from this page that all sensors with HPK test station were successful and there were no failures. The active thickness is 300 µm and they are low-density production sensors with 199 channels.
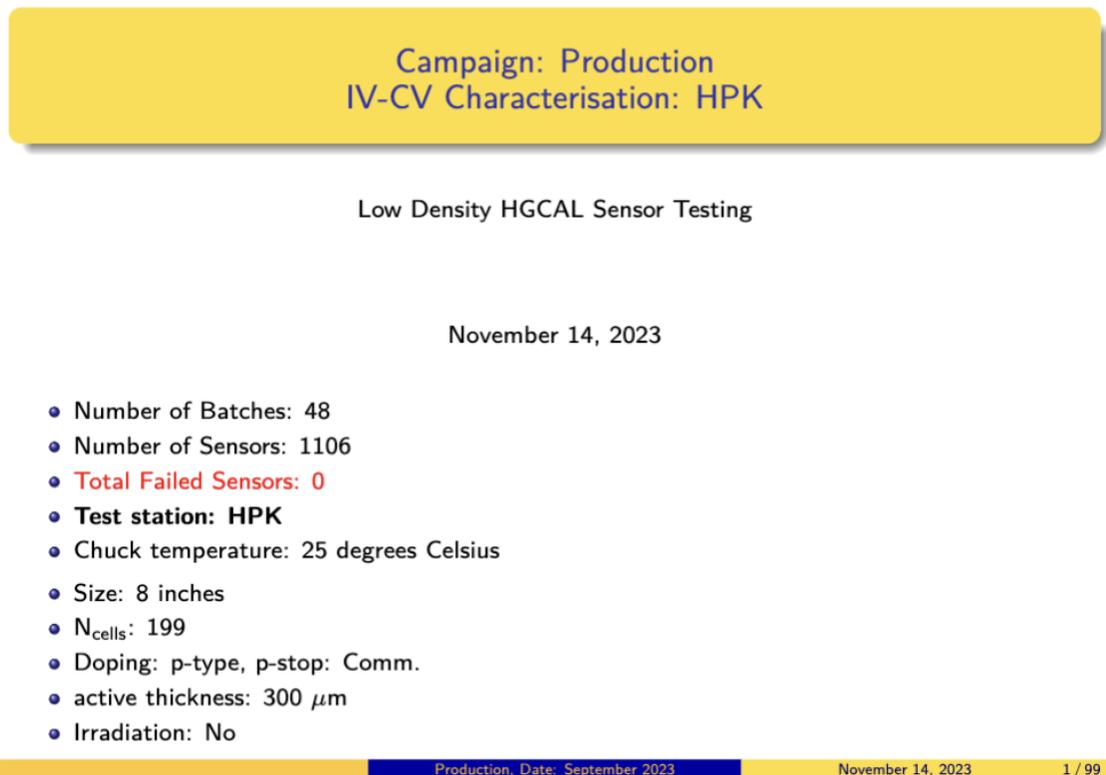
Figure 4.12: This is the first page representing the summary of the delivery made by HPK in September 2023, produced by the HexaBatch code.

Figure 4.13, the second page of the automatic presentation code generated by HexaBatch, shows a table with the number of sensors and batch numbers for the delivery in September. This table contains the number of sensors in the batch and the number of successful and unsuccessful sensors in each batch. The blue colors in the table, which mean warning, indicate that the batch has less than 20 sensors in total. Under normal conditions each batch should contain about 20-25 sensors. For example, in the table shown in Figure 4.13, 5 batches have less than 20 sensors (e.g. OBA47639 contains 9 sensors).

Table of the Campaign Production

OBA number	Number of sensors	Passed	Failed	OBA number	Number of sensors	Passed	Failed
OBA47634	17	17	0	OBA49343	24	24	0
OBA47639	9	9	0	OBA49386	24	24	0
OBA48990	22	22	0	OBA49388	25	25	0
OBA48993	23	23	0	OBA49389	24	24	0
OBA48994	20	20	0	OBA49424	24	24	0
OBA48996	20	20	0	OBA49425	25	25	0
OBA49002	23	23	0	OBA49426	24	24	0
OBA49046	24	24	0	OBA49427	25	25	0
OBA49047	19	19	0	OBA49428	25	25	0
OBA49088	17	17	0	OBA49429	25	25	0
OBA49089	24	24	0	OBA49431	24	24	0
OBA49322	23	23	0	OBA49759	13	13	0
OBA49323	24	24	0	OBA49760	25	25	0
OBA49324	24	24	0	OBA49763	25	25	0
OBA49325	24	24	0	OBA49764	24	24	0
OBA49326	22	22	0	OBA49765	25	25	0
OBA49327	25	25	0	OBA49768	25	25	0
OBA49328	24	24	0	OBA49769	23	23	0
OBA49329	22	22	0	OBA49770	23	23	0
OBA49338	25	25	0	OBA49771	25	25	0
OBA49339	25	25	0	OBA49773	25	25	0
OBA49340	25	25	0	OBA49932	25	25	0
OBA49341	25	25	0	OBA49937	24	24	0
OBA49342	25	25	0	OBA50033	24	24	0

Production, Date: September 2023   November 14, 2023   2 / 99

Figure 4.13: The summary table produced by the HexaBatch code for HPK's delivery in September 2023. The table contains the number of sensors and batch numbers in September. Blue color indicates less than 20 sensors in the batch.

The code also generates a plot showing the distribution of the number of sensors for each batch on delivery. Figure 4.14 shows this plot. From the graph it is possible to quickly check how many batches contain a lower or higher number of sensors.

After all this summary delivery information, the plots containing the IV and CV results of the sensors are started. The delivery results file prints all IV/CV plots for each OBA (in order of increasing number) on consecutive pages. For the guard ring current plot in the IV plots, if there is a sensor above the acceptance limit, the code automatically changes the color and prints the sensor name. This way the sensor is identified from the legend. Likewise, in the total current graph, the color for the failed sensor changes to red and the sensor name is printed on the legend. Sensors sometimes have hot cells that exceed the acceptance criterion of 100 nA. If there are sensors with outliers in the first IV plot 'Cell current graph', the HexaBatch code identifies sensor numbers for the hot cells. The sensor information with the hot cells is located at the bottom of the graph. Figure 4.15 shows the results of analyzing the IV plot for one batch.

The HexaBatch code also provides hexplot, leakage and total current plots for failed sensors, as well as the grading criteria. This information comes from the rating output produced by the IVCV analysis script and is included on the last page of the delivery summary result file. This shows the reasons for the failure of the sensors. The HexaBatch script generates an output file containing all the information that allows a detailed analysis of the IVCV characteristics of the sensors. The code also compares the HPK results with the sensors measured at CMS. Since not all sensors are tested at CMS, the data is stored by sensor number, not by batch number. Therefore, the code separates the sensor measured at CMS according to each OBA and compares them all. The code provides a result file comparing the IVCV behavior of the sensors at two different measurement stations (HPK and SQC institutes).

A summary of the results of the comparison of the results of the production sensor measured at CMS with the HPK data is shown in Figure 4.16. At CERN, one of the SQC institutes, 63 production sensors with a thickness of 300 µm were tested and two of them failed.
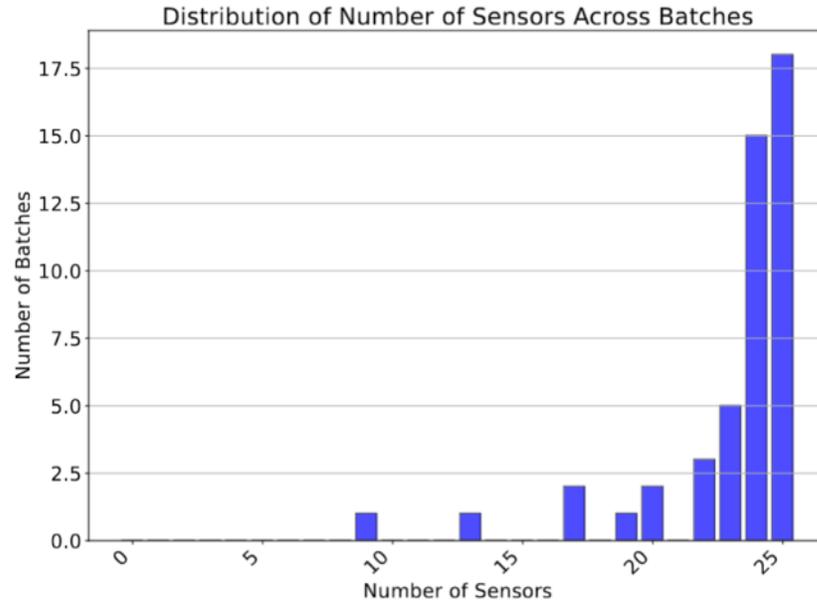
Figure 4.14: The distribution of the number of sensors for each batch for the delivery in September 2023. The pdf file containing the summary of the automated delivery produced by the HexaBatch code is on the third page.

Comparison of leakage current (a) and capacitance (b) measurement results of CMS and HPK data is shown in Figure 4.17. It can be seen from the guard ring and total current plots that the CMS data is measured when the bias voltage is applied up to 850 V, while the HPK data is up to 1000 V. Test procedures have been standardized across all SQC institutes. This facilitates testing for high throughput in future production phases. As a result, the voltage list has been reduced to the essentials. However, at times voltages of up to 1000 V were measured, especially for pre-production sensors. This is because by increasing the bias voltage we can increase the electric field in the silicon to reduce radiation damage and loss of charge collection efficiency. Unfortunately, leakage current (the noise) increases with bias voltage, so a compromise must be made by increasing the voltage, but not too much. The expectation is that the HL-LHC will eventually need up to 800 V for 200 µm and 300 µm sensors and about 600 V for 120 µm sensors.
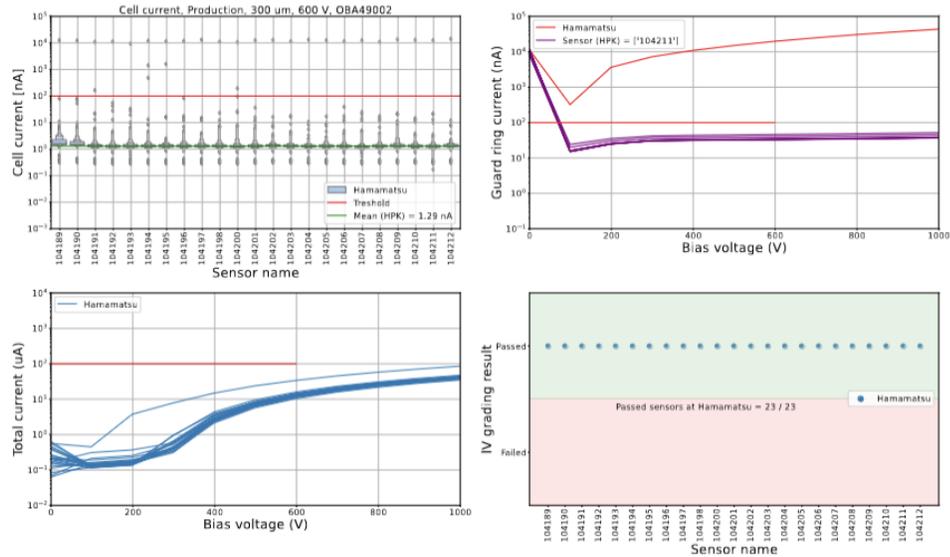
Figure 4.15: IV Results of production sensors in OBA49002 delivered in September 2023 and measured at HPK. Presentation in a nice format by HexaBatch code.

Figure 4.16: Comparison of HPK and CMS results of production sensors produced with HexaBatch code for the month of December 2023.
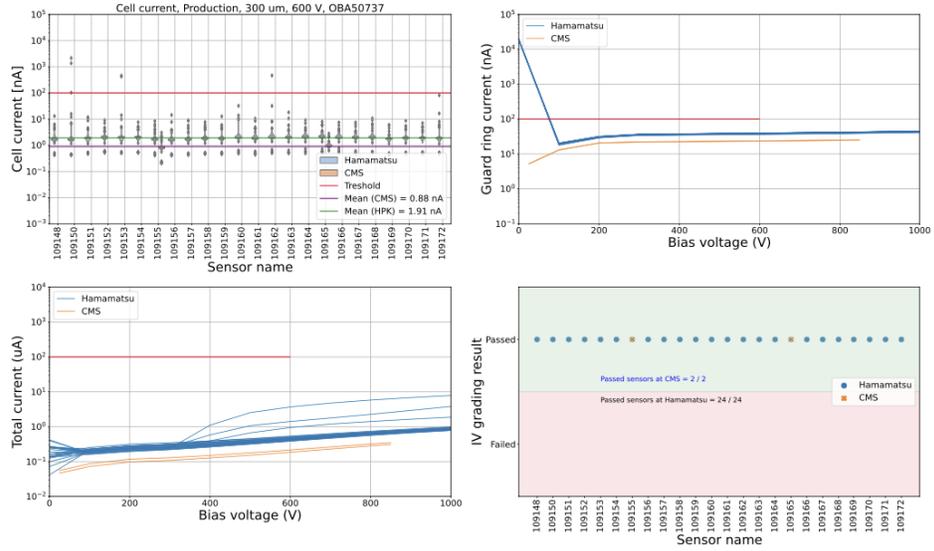
Figure 4.17: (a) Comparison of IV results of CMS and HPK data produced with HexaBatch.
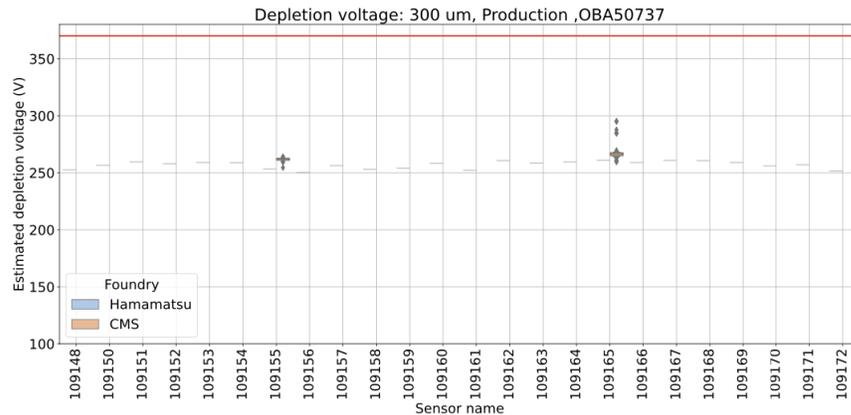
Figure 4.17: (b) Comparison of CV results of CMS and HPK data produced with HexaBatch.

The hexplot, cell and total current plots for the failed sensor measured at CERN are shown in Figure 4.18 (a). High current is observed on the guard ring after 700V. It can be seen from the plots that the sensor fails due to the increase in total current driven by the guard ring. Then Figure 4.18 (b), which includes all acceptance criteria, shows the ratio of the total current between 800 V and 600 V and the total current at 800 V. The factor of the sensor fails because it has a value much higher than 2.5. It is also observed that the sensor has a current of more than 10 µA at 800 V.
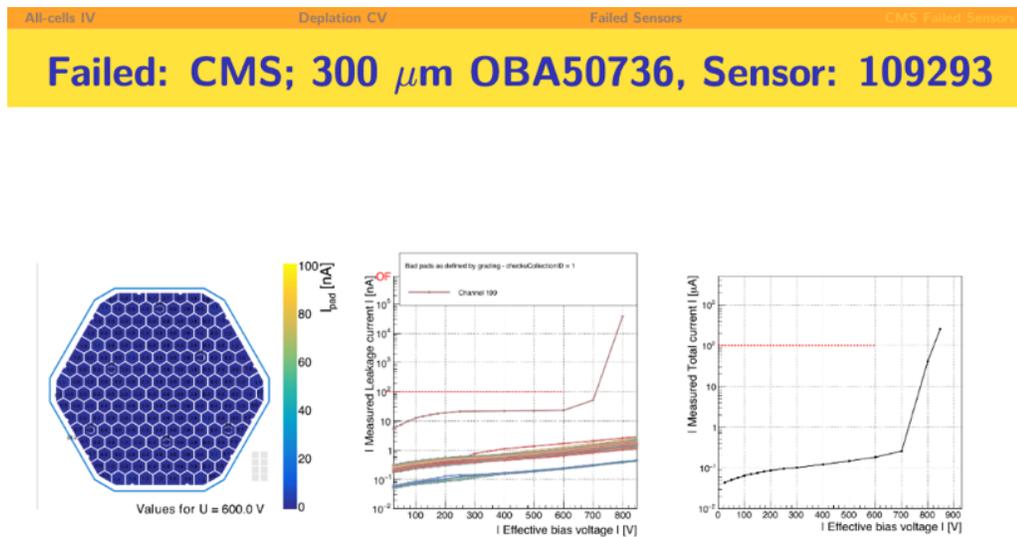
Figure 4.18: (a) HexaBatch code output of hexplot, cell and total current plots of sensor 109293 measured at CERN. The total current is driven by the guard ring current (cell 199).

Developed HexaBatch code for efficient analysis and visualization of large sensor data such as 1000 sensors produced by Hamamatsu. Provides measurement summaries for each delivery month.

All-cells IV   Deplation CV   Failed Sensors   CMS Failed Sensors

IV Grading of the sensor

Info:

- Last measured voltage point: 850.0 V;
- Expected depletion voltage for sensors of thickness 300 μm: 250 V; 250 $\times$ 1.5 = 375.0 V.
- IV scan performed well above 1.5 times the expected depletion voltage.

Grading:

- Sensor has been graded with checksCollectionID 1.
- Global characteristics:
  - Current at 600V I600 (normalised to 20 deg Celsius): $<=$ 100 μA integrated over the sensor and guard rings: Passed
  - I800 < 2.5 x I600: Failed
  - I600 = 0.151 uA I800 = 132.921 uA factor: 879.15
  - Number of bad pads 1 $<=$ 8 for full-sized sensors: Passed
  - Allowed number of adjacent bad pads $<=$ 2: Passed
- Per-pad characteristics used to define bad pads if any of the following are met:
  - Current at 600V I600 (normalised to 20 deg Celsius) > 100 nA/pad: **0** pads, namely **[]**
  - I600 > 10 nA and I800 > 2.5 x I600: **1** pads, namely **[199]**
  - I600 $\leq$ 10 nA and I800 > 25 nA: **0** pads, namely **[]**

Sensor has FAILED the requirements.
WARNING: The following pads were masked at least once before or at 600V: [].

Figure 4.18: (b) Output of the HexaBatch code showing the IV grading result of sensor 109293 measured at CERN. The total current of the sensor is greater than 10 µA at 800 V. Since the factor is greater than 2.5, the sensor is failed.

CHAPTER V

Conclusion and Recommendations

Conclusion

CERN will be adapted to the High-Luminosity LHC (HL-LHC), scheduled to start in 2028. The HL-LHC accelerator, which will produce five to ten times more collisions than the LHC (with different pile-up scenarios depending on the amount of incoming radiation), is expected to be capable of sorting out an average of about 150 particle pile-up events that occur in each collision.

Since 2008, very high levels of radiation damage have been observed in the CMS calorimetry system as a result of proton-proton collisions at the LHC.

Since the number of proton-proton collisions produced at the LHC will be ten times higher than originally planned for the CMS experiment, some of the existing detectors will not perform well enough in the HL-LHC phase and will have to be upgraded. This is because, although increasing the luminosity improves the potential for new physics research, in practice the large increase in the collision rate will lead to more complex collisions and more radiation. Therefore, the end-cap calorimeters (ECAL-EC and HCAL-EC) of the CMS detector will be replaced by high-granularity calorimetry (HGCAL).

This thesis mainly deals with the leakage current (IV) and capacitance (CV) measurement techniques and analysis results of the silicon sensors to be used for the CMS End Cap Calorimeter Upgrade. HGCAL, a sampling calorimeter, will use silicon sensors as the active material in high radiation regions. The silicon sensors, manufactured by Hamamatsu in Japan, have a hexagonal geometry cut from 8-inch wafers. They are manufactured on 8" wafers instead of 6" to optimize the number of modules. Hexagonal geometry was chosen because it is the best way to divide a surface into regions of equal area with a minimum total perimeter.

HGCAL will use silicon sensors of three different thicknesses. These are 120, 200 and 300 μm. The inside of the HGCAL cassette is where the radiation is more intense. For this

reason, high-density (HD) sensors with 432 channels will be used. HD sensors have an active thickness of 120 and 200 μm.

Since the outer part of the cassette is exposed to lower radiation, low-density (LD) sensors will be used in this area. LD sensors have 192 channels. The active thickness is 200 μm and 300 μm. During the thesis, electrical characterization of both full and partial silicon non-irradiated sensors were studied. These sensors were measured in two stages. The first one was performed by the manufacturer (HPK). HPK measured the sensor before it was removed from the cutting frame and transmitted the measurement data to CERN. The second measurement took place at CERN, one of the sensor quality control institutes. However, the CERN measurements were taken after removal from the shear frame. A python code called 'HexaBatch' was developed to batch analyze the measurement data sent by Hamamatsu and compare it with the CERN measurement results. Thus, sensor quality control institutes such as CERN can obtain measurement results in a short time (about 5 minutes). After each IVCV measurement, the sensor was classified as "pass" or "fail". For the sensors measured on the cutting frame at HPK, the rating results were successful. However, in the CERN measurements after the sensors were removed from the cube frame, about 7 sensors did not pass the rating due to the total current increase in the IV properties. According to the technical specifications for the procurement of silicon sensors for the CMS HGCAL upgrade project, the ratio between the sensor currents at 600 V and 800 V should not exceed 2.5.

Although the total current in these sensors is usually driven by the protection ring current, they were often observed to have low cell currents. For this reason, the failed sensors were re-measured and were found to be successful in the second measurement. The reason for the difference between the first and second measurement results is not known exactly, but it can be interpreted as humidity. On the other hand, it is well known that a cell (protection ring) affects the measurement performance. For sensors that failed for the same reason, a table was created and the results of the analyses were evaluated. In order to reduce the re-measurement rate by half, it has been suggested that if the total current of the sensor is less than 10 μA at 800V, the sensor is considered successful without the need for a second measurement. This is not yet included in the IV acceptance

criteria but is under evaluation. The same observations and results have been observed at other SQC CMS institutes.

In the next phase of the CMS End Cap Calorimetry Upgrade, the best sensors in mass production will be selected and sent to module assembly. The 620 m2 area of the CMS High Granularity Calorimeter for End Caps (HGCAL) will consist of silicon sensors. With this thesis work, the characterizations of the sensors in pre-production and production phase have been understood and developed. Full optical inspection of the front side and visual inspection of the back side of all sensors tested in the production phase. In addition, visual front and backside inspection of the silicon sensor is performed for significant scratches/chipped corners up to 11 per batch of approximately 25 sensors. Hexaboards to be used in HGCAL are complex hexagonal 8-layer PCBs equipped with up to six readout chips (HGCROC ASIC) that read signals from silicon diode pads with low noise and wide dynamic range. Two types of Hexaboard are available, low and high density. In order to maximize the active area coverage of the circular reference area of the CMS end caps, partial modules will be used. For this reason, partial boards are also available for hexaboard design (more than 10 types).

In this study, the quality control of the PCB (hexaboard) including electronics and connectors in pre-series, pre-production and production phase is discussed and developed. The first component of the silicon module, the hexaboard, is connected to the main board for data transfer and the data comes from the second component of the silicon module, the silicon sensors. The signals from the sensor pads are provided by on-board signal digitization readout chips.

A large number (tens of tens) of LD and HD hexaboards are produced and tested for sensor verification before mass production. This provides more statistical data for a better understanding of these designs before mass production. This allows physical damage to sensors and boards to be detected before module assembly.

Recommendations for Further Research

The HGCAL detector will be installed in the CMS experiment in 2026-28. Until then, all sensors need to be electrically characterized, irradiated with test radiation, tested

for radiation damage and installed on hexaboards. More hexaboards need to be electrically tested and more statistical data obtained. This will provide more statistical data for a better understanding of the designs.

Finally, the construction of the HGCAL detector needs to be completed at the P5 site where the CMS detector is located.

References

Abashian, A., et al. (Tech. Rep.). (2002). The Belle Detector. *Nucl. Instrum. Meth. A*, *479*, 117–232.

Abbaneo, D. (2004). Layout and Performance of the CMS Silicon Strip Tracker. *Nucl. Instrum. Meth. A*, *518*, 331–335.

Abbaneo, D. (2011, Dec). Upgrade of The CMS Tracker with Tracking Trigger. *Journal of Instrumentation*, *6*(12), C12065.

Acar, B. et al. (2023, Aug). Neutron Irradiation and Electrical Characterisation of the First 8" Silicon Pad Sensor Prototypes for the CMS Calorimeter Endcap Upgrade. *Journal of Instrumentation,* 18(08), P08024. Retrieved from http://dx.doi.org/10.1088/1748-0221/18/08/P08024 doi: 10.1088/1748-0221/18/08/p08024

Ahmed, S. (2007). *Physics Engineering of Radiation Detection*. Elsevier.

Aicheler, M., Burrows, P., Draper, M., Garvey, T., Lebrun, P., Peach, K. et al. (2012). *A Multi-TeV Linear Collider Based on CLIC Technology: CLIC Conceptual Design Report*. CERN.

Akchurin, N. et al. (2018, Oct). First beam tests of prototype silicon modules for the CMS High Granularity Endcap Calorimeter. *Journal of Instrumentation*, 13(10), P10023. Retrieved from https://dx.doi.org/10.1088/1748-0221/13/10/P10023 doi: 10.1088/1748-0221/13/10/P10023

Altarelli, G. (2013, Dec). The HIGGS: So Simple Yet so Unnatural. *Physica Scripta*, *2013*(T158), 014011.

Amendolia, S. R., Batignani, G., Bedeschi, F., Bertolucci, E., Bosisio, L., Bradaschia, C., Vincelli, M. L. (1980). A Multi Electrode Silicon Detector for High Energy Physics Experiments. *Nucl. Instrum. Methods Phys. Res.*, *176* (3), 457-60.

Antoniou, A. (2022). *Models, Data, and Unobservable Phenomena in Physics* (Doctoral dissertation, University of Bristol). Retrieved from https://research-information.bris.ac.uk/en/studentTheses/ models-data-and-unobservable-phenomena-in-physics (Presented 30 Jun 2022)

Azzi, P., Barney, D. et al. *The Phase-2 Upgrade of the CMS Endcap Calorimeter* (Tech. Rep.). (2017). Geneva: CERN. Retrieved from https://cds.cern.ch/record/2293646 doi: 10.17181/CERN.IV8M.1JY2

Bergauer, T., Dragicevic, M., Konig, A., Hacker, J., & Bartl, U. (2016). First Thin AC-coupled Silicon Strip Sensors on 8-inch Wafers. *Nucl. Instrum. Meth. A*, *830*, 473–479.

Bicken, B., Holm, U., Marckmann, T., Wick, K., & Rohde, M. (1991). Recovery and Permanent Radiation Damage of Plastic Scintillators at Different Dose Rates. *IEEE Trans. Nucl. Sci.*, *38*, 188–193.

Bilenky, S. M. & Hošek, J. (1982). Glashow-Weinberg-Salam Theory of Electroweak Interactions and The Neutral Currents. *Physics Reports*, *90* (2), 73-157.

Bouyjou, F., Bombardi, G., Callier, S., Dinaucourt, P., Dulucq, F., Berni, M. E., Vergine, T. (2022, Nov). HGCROC2: The Front-End Readout ASICS for the CMS High Granularity Calorimeter. *Journal of Physics: Conference Series*, *2374*(1), 012070.

Brondolin, E., Dannheim, D., Kulis, S., Maier, A. A., Pitters, F., Quast, T., & Sicking, E. (2019). ARRAY: An Open Source, Modular and Probe-Card Based System with Integrated Switching Matrix for Characterisation of Large Area Silicon Pad Sensors. *Nuclear Instruments and Methods in Physics Research Section A: Accelerators, Spectrometers, Detectors and Associated Equipment, 940,* 168-173.

Brondolin, E. (2020) *The Phase-2 Upgrade of the CMS Endcap Calorimeter Silicon Sensors for the HGCAL Upgrade Challenges, Sensor Design and Electrical Characterization. Silicon Sensors for the CMS HGCAL Upgrade: Challenges, Sensor Design, Electrical Characterization* (Tech. Rep. No. 05).

Bross, A., & Pla-Dalmau, A. (1992). Radiation Damage of Plastic Scintillators. *IEEE Transactions on Nuclear Science*, *39*(5), 1199-1204.

Bruning, O. S., Collier, P., Lebrun, P., Myers, S., Ostojic, R., Poole, J., & Proudlock, P. (2004). *LHC Design Report*.

Cankocak, K., Bakırcı, M., Cerci, S., Gulmez, E., Merlo, J., Onel, Y., Sonmez, N. (2008). Radiation-Hardness Measurements of High OH-Content Quartz Fibres Irradiated with 24 GeV Protons up to 1.25 Grad. *Nuclear Instruments and Methods in Physics Research Section A: Accelerators, Spectrometers, Detectors and Associated Equipment*, *585* (1), 20-27.

Casse, G., Affolder, A., Allport, P. P., & Wormald, M. (2008). Measurements of Charge Collection Efficiency with Microstrip Detectors made on Various Substrates after Irradiations with Neutrons and Protons with Different Energies. PoS, VERTEX2008, 036. doi: 10.22323/1.068.0036

Casse, G., Allport, P., Biagi, S., Bowcock, T., Greenall, A., & Turner, P. (2003). Charge Collection and Charge Sharing in Heavily Irradiated n-side Read-Out Silicon Microstrip Detectors. *Nuclear Instruments and Methods in Physics Research*

Section A: Accelerators, Spectrometers, Detectors and Associated Equipment, *511*(1), 112-117.

CERN. (2022). *The HL-LHC Project.* Retrieved 2024-05-09, from https://hilumilhc.web.cern.ch/content/hl-lhc-project

CERN Official Website. (Accessed November 21, 2023). Retrieved from https://home.cern/

CMS Official Website. (Accessed January 11, 2024). Retrieved from https://cms.cern/news/cms-detector-design

CMS Collaboration. *Expected Performance of the Physics Objects with the Upgraded CMS Detector at the HL-LHC* (Tech. Rep.). (2018).

Cooke, C. A. (2022). *Upgrade of the CMS Barrel Electromagnetic Calorimeter for the High Luminosity LHC* (Tech. Rep. No. 3).

Barney, D. (2021). *Sketchup images highlighting the Sub-Detectors*. Retrieved from https://cms-docdb.cern.ch/cgi-bin/PublicDocDB/ShowDocument?docid=11982

Barney, D. (2022). *Overview slide of CE with main parameters.* Retrieved from https://cms-docdb.cern.ch/cgi-bin/PublicDocDB//ShowDocument?docid=13251

Dainese, A., Mangano, M., Meyer, A. B., Nisati, A., Salam, G., & Vesterinen, M. A. (2019). *Report on the Physics at the HL-LHC, and Perspectives for the HE-LHC* (Tech. Rep.).

Denegri, D., Guyot, C., Hoecker, A., Roos, L. (2021). *The Adventure of the Large Hadron Collider: From the Big Bang to the HIGGS Boson*. World Scientific Publishing Company Pte Limited.

De Barbaro, P. et al. *The Phase-2 Upgrade of the CMS Barrel Calorimeters* (Tech. Rep.). (2017).

Evans, L. & Bryant, P. (2008, Aug). LHC Machine. *Journal of Instrumentation*, *3* (08), S08001.

Frank, I., & Tamm, I. (1937). Coherent Visible Radiation from Fast Electrons Passing Through Matter. *C. R. Acad. Sci. USSR*, *14*(109-114).

Gorodetzky, P., Lazic, D., Anzivino, G., Chiavassa, E., Contin, A., Dellacasa, G., Vercellin, E., et al. (1995). Quartz Fiber Calorimetry. *Nuclear Instruments and Methods in Physics Research Section A: Accelerators, Spectrometers, Detectors and Associated Equipment*, *361*(1), 161-179. Retrieved from https://www.sciencedirect.com/science/article/pii/0168900295002952

Grupen, C., & Shwartz, B. (2008). *Particle Detectors*. Cambridge: Cambridge University Press.

Gusarov, A., & Hoeffgen, S. (2013, 06). Radiation Effects on Fiber gratings. *Nuclear Science, IEEE Transactions on*, *60*, 2037-2053.

Hartmann, F. (2017). *Evolution of Silicon Sensor Technology in Particle Physics* (Vol. 275). Springer.

Hayrapetyan, A., et al. (2023, 9). Development of the CMS Detector for the CERN LHC RUN3.

Higgs, P. W. (1964, Oct). Broken Symmetries and the Masses of Gauge Bosons. *Phys. Rev. Lett.*, *13*, 508–509.

Hinger, V. (2021). *Silicon Sensor Process Quality Control for the CMS Phase-2 Upgrade* (Doctoral dissertation, Vienna University of Technology).

HL-LHC Website. (Accessed January 11, 2024). Retrieved from https://hilumilhc.web.cern.ch/

Hmayakyan, G. et al., (2008, Aug). *The CMS experiment at the CERN LHC,* 3 (08), S08004. Retrieved from https://dx.doi.org/10.1088/1748-0221/3/08/S08004

Jenni, P. & Virdee, T. S. (2020). The Discovery of the HIGGS Boson at the LHC. In H. Schopper (Ed.), *Particle Physics Reference Library: Volume 1: Theory and Experiments* (pp. 263–309). Cham: Springer International Publishing

Khan, F. A. (2023). *Design and Performance Optimisation of the Hexaboards for CMS HGCAL On-Cassette Readout Electronics* (Tech. Rep. No. 03).

Knoll, G. (1999). *Radiation Detection and Measurement*. New York: John Wiley Sons Inc.

Krige, G. J. (1996). *History of CERN*. Amsterdam: North-Holland.

Kronheim, B., Belloni, A., Edberg, T., Eno, S., Howe, C., Palmer, C., Sriram, S. (2024, Feb). Reduction of Light Output of Plastic Scintillator Tiles During Irradiation at Cold Temperatures and in Low-Oxygen Environments. *Nuclear Instruments and Methods in Physics Research Section A: Accelerators, Spectrometers, Detectors and Associated Equipment*, *1059*, 168922.

Lobanov, A. (2020, July). Precision Timing Calorimetry with the CMS HGCAL. *Journal of Instrumentation*, *15*(07), C07003–C07003.

Ochando, C. (2017). HGCAL: A High-Granularity Calorimeter for the End- Caps of CMS at HL-LHC. *J. Phys.: Conf. Ser.*, *928*(1), 012025.

Paulitsch, P. (2020). The Silicon Sensors for the High Granularity Calorimeter of CMS. *Nuclear Instruments and Methods in Physics Research Section A: Accelerators, Spectrometers, Detectors and Associated Equipment*, *978*, 164428.

Pásztor, G. et al., (2021). *The Phase-2 Upgrade of the CMS Beam Radiation Instrumentation and Luminosity Detectors* (Tech. Rep.).

Penzo, A. et al. (2009, Apr). The CMS-HF Quartz Fiber Calorimeters. *Journal of Physics: Conference Series*, *160*(1), 012014.

Peskin, M. E. & Daniel V. S. (2019). *An Introduction to Quantum Field Theory*. Elsevier-CRC.

Pitters, F. M. (2019). Silicon Detector Technologies for Future Particle Collider Experiments (Doctoral dissertation, Vienna, Tech. U.) Retrieved from https://cds.cern.ch/record/2714709 (Presented 2020)

Quast, T. (2020). *Qualification, Performance Validation and Fast Generative Modelling of Beam Test Calorimeter Prototypes for the CMS Calorimeter Endcap Upgrade* (Doctoral dissertation, RWTH Aachen U.) Retrieved from https://cds.cern.ch/record/2746196 (presented on 28 May 2020)

Quast, T. et al. (2024). *HGC Sensor IVCV Analysis.* Retrieved from https://gitlab.cern.ch/CLICdp/HGCAL/lcdhgcalanalysisworkflows

Schmidt, B. (2016, Apr). The High-Luminosity Upgrade of the LHC: Physics and Technology Challenges for the Accelerator and the Experiments. *Journal of Physics: Conference Series*, *706*(2), 022002.

Sicking, E. (2023). *HGCAL Sensor Testing Instructions 2023.* Retrieved from https://twiki.cern.ch/twiki/bin/view/CMS/HGCALSensorTestingInstructions2023

Strobbe, N. (2022). Readout Electronics for the CMS Phase 2 Endcap Calorimeter: System Overview and Prototyping Experience. *JINST*, *17*(04), C04023.

V. Khachatryan et al. (2016, Oct). Dose Rate Effects in the Radiation Damage of the Plastic Scintillators of the CMS Hadron Endcap Calorimeter. *Journal of Instrumentation*, *11*(10), T10004.

Wick, K., Paul, D., Schroder, P., Stieber, V., & Bicken, B. (1991). Recovery and Dose Rate Dependence of Radiation Damage in Scintillators, Wavelength Shifters and

Light Guides. *Nuclear Instruments and Methods in Physics Research Section B: Beam Interactions with Materials and Atoms*, *61*(4), 472-486.

Workman, R. L. et al. (2022). Review of Particle Physics. *PTEP*, *2022*, 083C01.

Zorn, C., Johnson, K., Kross, B., Majewski, S., & Wojcik, R. (1993). Preliminary Results from a Low Dose Rate Irradiation of Selected Plastic Scintillating Fibers. *Nuclear Physics B - Proceedings Supplements*, *32*, 369-376.

Appendices

Appendix A

Ethical Approval Letter

YAKIN DOĞU ÜNİVERSİTESİ

ETHICAL APPROVAL DOCUMENT

Date: 28/05/2024

To the Institute of Graduate Studies

The research titled **"Upgrade of CMS Endcap Calorimeters and Silicon Sensor Characterization"** has been evaluated. Since the researcher will not collect primary data from humans, animals, plants or earth, this project does not need through the ethics committee.

Title: Prof. Dr.

Name Surname: Kerem CANKOÇAK

Signature:

Role in the Research Project: Supervisor

Appendix B

Turnitin Similarity Report

Appendix C

Curriculum Vitae (CV)

Gizem Gül Dinçer was born on October 31, 1997, in Istanbul. She completed her secondary and high school education in Istanbul. In 2021, she graduated from the Department of Astronomy and Space Sciences. In 2022, she started her master's degree at Istanbul Technical University and was sent to CERN with the support of Near East University. In the spring semester of 2023, she started her Master's degree in Physics Engineering at Near East University. She is currently working as a researcher at CERN.